

**Exploring bonding interactions of biochemical relevance in  
silicon, platinum(II) and iron(III) positively charged species**

**Doctoral thesis of**

**Dr. Alberto De Petris**

Presented to the Department of Department of

Drug Chemistry and Technologies

Sapienza Università di Roma

for the Degree of

**Ph.D. in Pharmaceutical Sciences**

**Sapienza Università di Roma**

**January 2014**



*Truth is what stands the test of experience.*

— Albert Einstein



**Abstract.** Elements playing a biological role that are present in nature or in synthetic drugs, such as silicon, platinum(II) and iron(III) usually appear coordinated to ligands in more or less composite molecular architectures. This notion is particularly true when a metal ion is placed in the active center of an enzyme or otherwise integrated into simple biomolecules and proteins. Whereas multifaceted factors affect a charged (metal) centre in a biological environment, the gas-phase provides an interesting medium for elucidating intrinsic interactions between metal ions and biological targets. The idea underlying this doctoral thesis is to highlight how state of the art techniques combining mass spectrometry, IR spectroscopy and computational chemistry can be applied to the study of ionic complexes in an isolated state. In a first section the reactivity behavior of gaseous complexes from the  $(\text{CH}_3)_3\text{Si}^+$  addition to acetylene has been fully explored by FT-ICR mass spectrometry and ab initio calculations. In this way the  $\text{C}_5\text{H}_{11}\text{Si}^+$  potential energy surface has been elucidated and the computational results nicely account for the experimental evidence showing an isomerization process from a primarily formed complex (a  $\beta$ -silyl-substituted vinyl cation acquiring an asymmetric cyclic geometry) to  $\text{CH}_2=\text{C}(\text{CH}_3)\text{-Si}(\text{CH}_3)_2^+$  silyl cation. The computational methods tested in dealing with the  $\text{C}_5\text{H}_{11}\text{Si}^+$  ion problem have been further applied to more challenging systems. In a second and third section a comprehensive investigation of the structural features of the key intermediates which are formed from cisplatin by replacement of chloro ligands by water or methionine is described. Here the experimental approach has involved vibrational spectroscopy carried out with a recently designed and assembled apparatus. The NH/OH stretching region has been found highly structurally diagnostic in the aqua complexes where hydrogen bonding interactions are crucial in determining relative conformer stability. The infrared characterization of the monofunctional adducts of platinum(II) drugs

with methionine has led to identify distinct modes of interaction with cisplatin and transplatin derived species. In fact, the preferred ligand atom (S or N) seems to be depending on the specific isomer (*cis*- or *trans*-) that is reacting with the metal. Cisplatin and transplatin derived species have been sampled both experimentally and computationally, taking into account relativistic effects in the heavy metal. In a fourth task the binding properties ofazole ligands toward ferric heme have been examined. Starting from simple ligands such as pyridine, 1-methylimidazole and 1H-1,2,4-triazole, the focus was then directed to imidazole- and triazole-based antifungal drugs. These drugs are known to act as inhibitors of CYP51enzyme, through binding to the heme prosthetic group. Relative binding energies were determined experimentally by energy variable collision induced dissociation experiments performed on the selected ionic complexes and evaluated theoretically by Car-Parrinello molecular dynamics calculations. To this end, theoretical investigations were carried out during a training period spent at the “Parc Cientific de Barcelona”, under the supervision of Research Professor Carme Rovira. Imidazole-based drugs consistently display higher dissociation energies when compared to triazole-based drugs.

## Index

<b>Introduction to Bioinorganic Chemistry</b> .....	13
I Bioinorganic Chemistry: An Introduction to the Field.....	13
II Spectroscopic Methods.....	16
III Mass Spectrometric Methods (Electrospray Tandem Mass Spectrometry).....	18
IV Theoretical Chemistry.....	19
V Instrumental Details.....	29
VI IRMPD Spectroscopy: ESI FT-ICR coupled with FEL and OPO/OPA Lasers.....	29
VII ESI-MS/MS Mass Spectrometry: Triple Quadrupole Linear Ion Trap Mass Spectrometer.....	31
VIII References.....	33
CHAPTER 1	
<b>Isomeric C<sub>5</sub>H<sub>11</sub>Si<sup>+</sup> ions from the trimethylsilylation of acetylene: an experimental and theoretical study</b> .....	35
1.1 Introduction .....	36
1.2 Experimental Details .....	39
1.2.1 Materials .....	39
1.2.2 FT-ICR Mass Spectrometry.....	39
1.2.3 Computational Details .....	40
1.3 Results and Discussion .....	41
1.3.1 Sample Ion(s) and Model Ions.....	41
1.3.2 Ion-Molecule Reactions of C <sub>5</sub> H <sub>11</sub> Si <sup>+</sup> Ions .....	42
1.3.3 C <sub>5</sub> H <sub>11</sub> Si <sup>+</sup> Isomers and Rearrangement Pathways: a Quantum Chemical Assay .....	47
1.4 Conclusions .....	56
1.5 References .....	58

## CHAPTER 2

### **Vibrational signature of the naked aqua complexes from platinum(II)**

<b>anticancer drugs: an experimental and theoretical study</b> .....	63
2.1 Introduction .....	64
2.2 Results and Discussion .....	64
2.3 Experimental Method .....	74
2.4 References .....	76

## CHAPTER 3

### **Cisplatin and transplatin complexes with L-methionine:**

<b>an assay by IRMPD spectroscopy with methionine</b> .....	79
3.1 Introduction .....	80
3.2 Experimental Details .....	81
3.3 Results and Discussion .....	82
3.3.1 Conformational Analysis .....	82
3.3.2 Vibrational Analysis .....	84
3.4 Conclusions .....	94
3.5 References .....	95

## CHAPTER 4

### **Binding interactions in heme-azole complexes: combined application of energy-resolved threshold collision-induced dissociation and**

<b>Car-Parrinello molecular dynamics calculation</b> .....	97
4.1 Introduction.....	98
4.2 Experimental Section.....	103
4.2.1 Materials.....	103
4.2.2 CID Experiments.....	104
4.2.3 Computational Details.....	105
4.3 Results and Discussion.....	107
4.3.1 Kinetic Energy of the Precursor Ion.....	107
4.3.2 Phenomenological Threshold Energies Determination.....	109
4.3.3 Bond Dissociation Energy Calculations.....	114



4.4	Conclusions.....	118
4.5	Training Experience in CPMD Calculations at Parc Cientific de Barcelona .....	119
4.6	References.....	120



## List of Publications.

- 1) Siehl, H. U.; Brixner, S.; Coletti, S.; Re, N.; Chiavarino, B.; Crestoni, M. E., De Petris, A.; Fornarini, S. Isomeric  $C_5H_{11}Si^+$  ions from the trimethylsilylation of acetylene: An experimental and theoretical study *Int. J. Mass Spectrom.* **2013**, 334, 58-66.
- 2) De Petris, A.; Ciavardini, A.; Coletti, C.; Re, N.; Chiavarino, B.; Crestoni, M. E.; Fornarini, S. Vibrational Signatures of the Naked Aqua Complexes from Platinum(II) Anticancer Drugs *J. Phys. Chem. Letters* **2013**, 4, 3631-3635.
- 3) In vitro inhibition of herpes simplex virus type 1 replication by *Mentha suaveolens* essential oil and its main component piperitenone oxide. Manuscript accepted for publication (Phytomedicine, Elsevier).
- 4) Binding Interactions in Heme-Azole Complexes: Combined Application of Energy-Resolved Threshold Collision-Induced Dissociation and Car-Parrinello Molecular Dynamics Calculation. *Manuscript in preparation*.



# INTRODUCTION TO BIOINORGANIC CHEMISTRY

## I. Bioinorganic Chemistry: An Introduction to the field

Among the three different element-based species (Si, Pt(II) and Fe(III)-heme), heme cations and Pt-containing drugs pertain to the field of bioinorganic chemistry. Bioinorganic chemistry constitutes the interface of the more classical areas of inorganic chemistry and biology. It has two major components: the study of naturally occurring inorganic elements in biology and the introduction of metals into biological systems as probes and drugs. Peripheral but essential aspects of the discipline include investigations of inorganic elements in nutrition, of the toxicity of inorganic species, including the ways in which such toxicities are overcome both by the natural systems and by human intervention, and of metal-ion transport and storage in biology. Even these added topics do not exhaust all aspects of the field, however<sup>1</sup>.

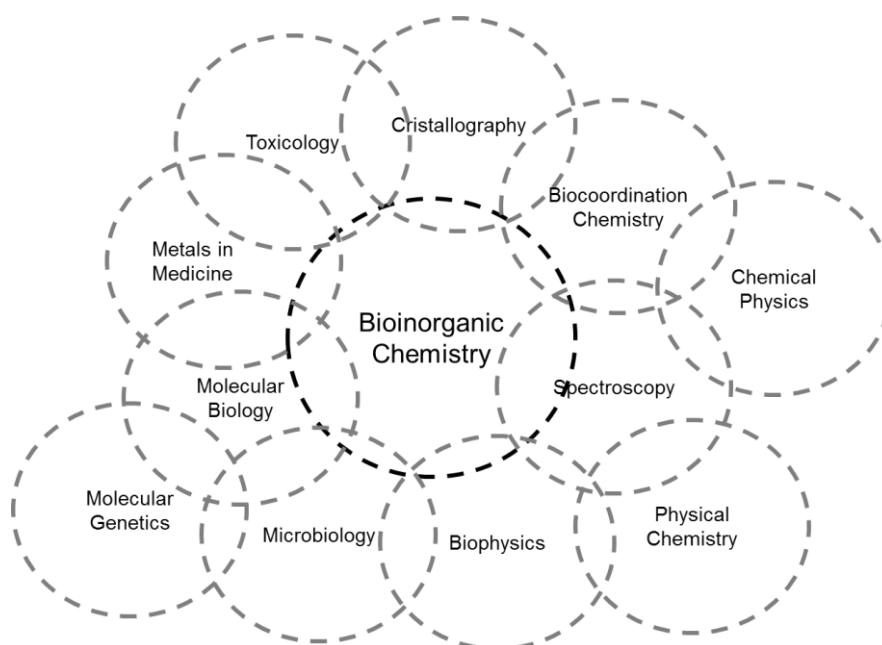


**Figure 1.** View of adjacent and overlapping fields from the bioinorganic view<sup>2</sup>.

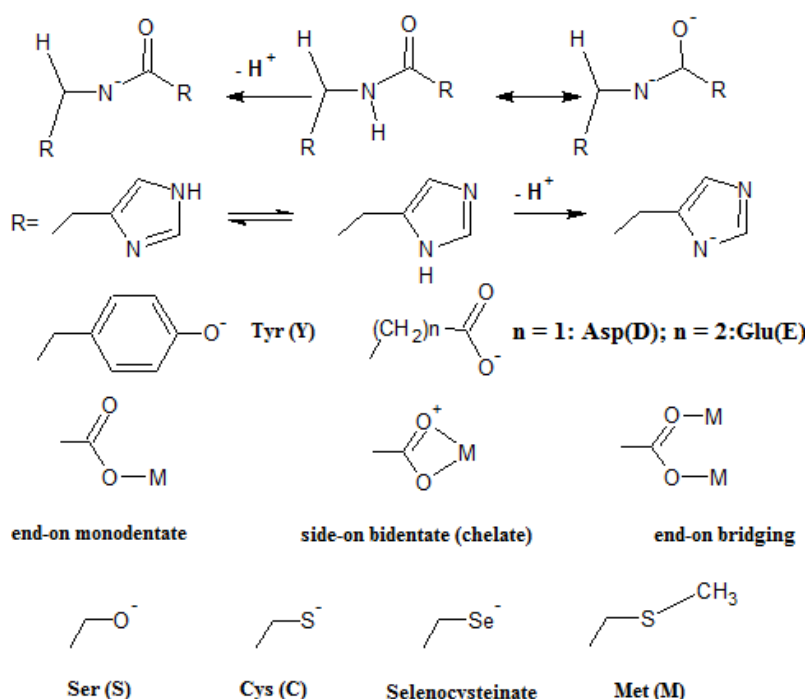
At this point it is necessary to define what is actually meant by the terms “inorganic” and “organic” in the context of medicinal chemistry as a scientific discipline. The term “organic” include the chemistry of carbon compounds; while, on the other hand, “inorganic” is generally perceived as referring to the chemistry of metal compounds, whereas other non-carbon non-metal elements are not specifically excluded. Because metals of many kinds are found in living matter (e.g. sodium, potassium and calcium) and because all metals are subjects of inorganic chemistry, there must then always have been an inorganic component of biochemistry. Thus, according to this reasoning, “bioinorganic chemistry” certainly is not a new subject; rather they may only be new subject<sup>2</sup>.

Living organisms store and transport transition metals both to provide appropriate concentrations of them for use in metalloproteins or cofactors and to protect themselves against toxic effects of metal excesses. The normal concentration range for each metal in biological systems is narrow, with both deficiencies and excesses causing pathological changes. In multicellular organisms, composed of a variety of specialized cell types, the storage of transition metals and the synthesis of the transporter molecules are not carried out by all types of cells, but rather by specific cells that specialize in this tasks. The form of the metals is always ionic, but the oxidation state can vary, depending on biological needs<sup>1</sup>. Inorganic “substances” in living systems can be metal ions (such as  $K^+$ ,  $Fe^{3+}$  and  $Fe^{2+}$ ), but also composite ions (e.g. molybdate), coordination compounds (e.g. metal-based drugs like cisplatin and carbonyltechnetium), or inorganic molecules such as  $CO$ ,  $NO_2$ ,  $O_3$ . Inorganic reactions have possibly played an important role in the formation and development of organic molecules of life in the prebiotic area (terrestrial and/or extraterrestrial), and from the very beginning of life on Earth.

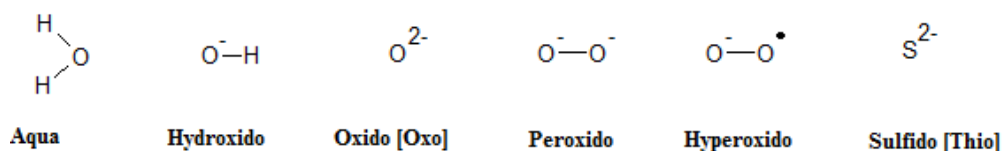
H																		
Li														B	C	N	O	F
Na	Mg														Si	P	S	Cl
K	Ca			V		Mn	Fe	Co	Ni	Cu	Zn				As	Se	Br	
					Mo	Te									Sn	Sb		I
	Ba	Gd			W					Pt	Au					Bi		

**Figure 2.** Periodic Table of the bio-elements: elements building up bio-mass, additional essential elements, essential for some groups of organisms, medically important elements.

Transition metal ions normally are not present in a free form, but rather coordinated (complexed) to ligands. In particular, this applies to metal ions in the active centres of enzymes or otherwise integrated into peptides and proteins. The chelating atoms are usually O, N, S,P or C. Examples for the respective ligands are listed below (N-functional: peptide moiety, porphinogenes, histidine; O-functional: tyrosinate, serinate, glutamate and aspartate; S-functional: cysteinate and methionine):



Additional inorganic ligands:



Proteins with which transition metals and zinc are most commonly associated catalyze the intramolecular or intermolecular rearrangements of electrons. Although the redox properties of the metals are important in many of the reactions, in others the metal appears

to contribute to the structure of the active state (Zinc in the Cu-Zn dismutases and Iron in the photosynthetic reaction centers).

## II. Spectroscopic Methods

Several modern methods have currently been applied to the study of metal ions in biology, and to highlight the importance of inorganic chemistry in biology. They include IR (Infra Red), Raman and NMR (Nuclear Magnetic Resonance) spectroscopy, mass spectrometry, X-ray crystallography, molecular biology, enzymology, and theoretical chemistry. Even as little as perhaps fifty years ago the idea that metal ions had any role in biology appealed only to a small minority of believers, but an overwhelming body of evidence has accumulated in the foreground to categorically demonstrate the diversity of roles that inorganic metals play in biology.

In the realm of high energy radiation, it is important to mention the relatively recent development of X-ray absorption spectroscopy, which became feasible when sufficiently powerful beam lines became more generally available at the reactor site<sup>2</sup>. Various features of these spectra have attracted attention: X-ray absorption near edge structures and more recently also pre-edge structures (XANES), and the extended near edge absorption fine structures (EXAFS), from which distances to neighboring nuclei can be determined or estimated, or certain types of nuclei can be excluded, depending on the quality of the spectra. EXAFS, for instance, has played a decisive role in the discovery and determination of the 3Fe clusters of Fe-S proteins<sup>3</sup>, and particular attention has been paid recently to the pre-edge features in XANES<sup>4</sup>, as it can furnish quantitative information on the degree of covalency of metal-ligand bonds<sup>5</sup>. This has been successfully accomplished for Fe-S proteins and has given new insights into the electronic structures of Fe-S proteins.

After these considerations, it is also important to consider the use of spectroscopy at other frequencies, starting from the lower energy end. NMR has undergone a very impressive development after the introduction of two- and higher-dimensional techniques, in combination with elaborate pulsing techniques and Fourier transform analysis, particularly also by the use of isotopes of a nuclear spin different from that of the naturally occurring atoms, such as  $^2\text{H}$ ,  $^{15}\text{N}$ ,  $^{13}\text{C}$ ,  $^{17}\text{O}$ , and  $^{57}\text{Fe}$ . For use with metal proteins the exploration of “paramagnetic NMR”, that is NMR on paramagnetic substances, has



obtained a great success<sup>6</sup> and has now become a routine procedure and the method of choice for answering specific questions. For instance, when the sequence of a protein is known and preferably also the three-dimensional structure around the metal site, the unpaired spin density on specific atoms can be determined. It has been possible to observe the migration of spin density between sites<sup>7</sup>.

Infrared spectroscopy is one of the powerful basic method for biological structure characterization. The tool greatly benefited from the advent of Fourier Transform IR spectroscopy that increased enormously the experimental resolution. Positioning an absorption cell in an infrared light beam permits to obtain an entire spectrum also from a gaseous sample. Fourier Transform and laser sources improve the resolution and the sensitivity of the spectra, respectively. When the species to be sampled is gaseous charged species, however, major problems arise in applying IR spectroscopy, that is one of the basic means for molecular structure characterization. Only recently the direct spectroscopic assay of a gaseous ion has been developed as a tool to ascertain an ion structure due to the development of infrared multiple photon dissociation (IRMPD) spectroscopy. The technique is now gaining widespread popularity, especially as a tool to distinguish among candidate structures. A brief outline of the underlying principle is the following. A general problem of direct absorption measurements is their inherently limited sensitivity. For this reason IR direct absorption spectroscopy is mostly confined to stable species having a sufficient vapor pressure and the number densities for routine measurements are on the order of  $10^{10}$  molecules/cm<sup>3</sup> or higher. Coulombic repulsion in a cloud of ions having the same charge usually limits the obtainable number densities to about  $10^6$  ions/cm<sup>3</sup>. The introduction of a mass selection device, that is required to isolate the ions of interest, usually reduces the ion density to an extent that the direct measurement of the absorption is essentially impossible. Therefore, a so-called action spectroscopy is rather performed. It is based on the point that the absorption of infrared radiation can induce dissociation of a molecule or a complex and this can be detected by recording the intensity of the resulting fragments using mass spectrometry. IR induced fragmentation is only observed on resonance with an IR active vibrational mode of the ion. As the energy of one IR photon is insufficient to cause dissociation of molecules and strongly bound complexes the experimental strategy of IRMPD has been developed to effect photodissociation. Many photons are absorbed resonantly and their energy is stored in the bath of vibrational modes,

leading to dissociation. IRMPD of gaseous ions requires a high intensity laser source if strong covalent bonds are to be broken in order to achieve photofragmentation in the 50-2500  $\text{cm}^{-1}$  mid-IR region. The emergence of free electron lasers (FELs) and recent breakthroughs in bench top lasers based on nonlinear optics have now made it possible to record IR spectra of gas-phase ions. These sources provide the high fluence required for the multiple absorption process inducing fragmentation of the bare molecular ion and at the same time are efficiently tunable sources.

### III. Mass Spectrometric Methods (Electrospray Tandem Mass Spectrometry)<sup>14-17</sup>

The analysis of metal-complexes with biomolecular ligands at the trace level poses a number of challenges to the analyst<sup>18</sup>. Despite the fundamental role that electrospray<sup>19</sup> and MALDI<sup>20</sup> have played in the systematic acquisition of information relevant to proteins and their functions<sup>21,22</sup>, mass spectrometry alone seems to be unable to provide answers to many question that are relevant to charged metal-complexes with biomolecules, in spite of the advantage of the long lifetime experienced by the species in the gas-phase even if only transient in solution. The Electrospray Ionization Mass Spectrometry (ESI-MS) has found widespread use in the determination of non-covalent interactions and functional proteomic analyses. Complexes of biological molecules, such as amino acids, peptides, proteins, and carbohydrates with transition metals are readily transferred into the gas-phase by ESI, and their gas-phase and solution properties can be correlated<sup>23</sup>. The technique is highly specific and sensitive. A serious inconvenience with the use of electrospray to probe the metal-ligand interactions and to determine metal-ligand stochiometry is its poor tolerance to non-volatile salt buffers and other solubilizing agents (detergents), which are often necessary to maintain the analyte's stability and integrity. Depending on how the electrosprayed ion is further handled, different type of information on the identity of the molecule of interest can be obtained. In the simplest case (molecular ion or single MS mode), one or more protons can be attached to the analyte's molecule to form a single- (generally for species up to 1000 Da) or multi-charged ion. In this way, the molecular mass of the analyte species can be determined.

In tandem mass spectrometry, the protonated molecular ions  $(M + nH^+)^{n+}$  can be fragmented by increasing the ionization energy (orifice voltage) at the source in the

process referred to as source collision-induced dissociation (SCID). Finally, the molecular ion, isolated at the level of the first mass filter can be fragmented by collision with molecules of a neutral gas in a process referred to as collision-induced dissociation<sup>24</sup>. The resulting fragments, analyzed with a second mass analyzer (tandem MS mode), allow informations on the structure of the molecule to be obtained.

#### IV. Theoretical Chemistry

**QM Calculation.** Computational chemistry is increasingly growing as a versatile tool in understanding chemical phenomena. By using more sophisticated QM theory, the chemist can better model a chemical system to be studied. The goal of this thesis is to clearly demonstrate that QM calculations can help in predicting and explaining the complexities of the chemical phenomena explored/evidenced by mass spectrometry and IRMPD spectroscopy.

In the first section of this chapter QM methodologies will be defined, along with a general explanation of how the electronic structure of atoms and molecules is modeled. The second part is dedicated to ab initio calculations applied to the field of bioinorganic chemistry, and how this powerful tool help the electronic description of organometallic complexes.

To begin, the energy of a system is described by:

Eq. (1.1)

$$\hat{H}\Psi(x, t) = E\Psi(x, t)$$

where the Hamiltonian operator ( $\hat{H}$ ) is operating on the eigenfunction ( $\Psi$ ), which represents the system as a wave function, and the outcome, the eigenvalue, represents the total energy ( $E$ ) of  $\Psi$ . The Hamiltonian has the form of

Eq. (1.2)

$$\hat{H} = -\sum_i \frac{\hbar^2}{2m_e} \nabla_i^2 - \sum_k \frac{\hbar^2}{2m_k} \nabla_k^2 - \sum_i \sum_k \frac{e^2 Z_k}{r_{ik}} + \sum_{i < j} \frac{e^2}{r_{ij}} - \sum_{k < l} \frac{e^2 Z_k Z_l}{r_{kl}}$$

where  $i$  and  $j$  number electrons,  $k$  and  $l$  number of nuclei,  $\hbar$  is Planck's constant divided by  $2\pi$ ,  $m_e$  is the mass of an electron,  $m_k$  is the mass of nucleus  $k$ ,  $\nabla^2$  is the

Laplacian operator,  $e$  is the charge of an electron,  $Z$  is the atomic number, and  $r_{ab}$  is the distance between particles  $a$  and  $b$ . The first two terms of the operator represent the kinetic energy of the electrons and nuclei, respectively. The following three terms represent the potential energy of electron-nuclear attraction, inter-electronic repulsion, and inter-nuclear repulsions, respectively. Equation (1.1) has many acceptable wave functions for a given molecule, where each  $\Psi$  is associated with a different expectation value. The energy of a wave function describing a chemical system can be solved by:

Eq. (1.3)

$$\frac{\int \Psi_i^* \hat{H} \Psi_i}{\int \Psi_i^* \Psi_i} = E$$

This equation proves useful as a prescription for determining the molecular energy; however, it is still difficult to find  $\Psi$ . Instead, we can approximate  $\Psi$  with  $\Phi$ , where commonly  $\Phi$  is a linear combination of atomic orbitals. We assume that every molecule has a ground state with  $E_0$  and  $\Psi_0$ , and that for every  $\Phi$  approximation, there is an associated  $E$  that is equal to or greater than  $E_0$  (the variational principle). The energy of  $\Phi$  is evaluated

Eq. (1.4)

$$\frac{\int \Phi^* \hat{H} \Phi}{\int \Phi^* \Phi} = E \geq E_0$$

As the value of  $E$  approaches the value of  $E_0$ , the approximation of  $\Phi$  approaches the lowest energy wave function  $\Psi$ .

**Density Functional Theory.** Other QM methods require calculating the probability density of the electrons of the system. The wave function is dependent on the spatial coordinates of each electron and all possible interactions with each electron. Instead, DFT postulates that the energy of a molecule can be determined from the electron density ( $\rho$ ). Electrons interact with one another and an ‘external potential,’ which refers to nuclei at a particular geometry.  $\rho$  corresponds to a unique ‘external potential,’ which means there is a one-to-one mapping of  $\rho$  to  $E$ . This is known as the Hohenberg-Kohn Existence Theorem. The number of electrons ( $N$ ) and molecular space are arguments for density, which is used as the argument for determining the energy. The energy functional is given as:

Eq. (1.5)

$$E[\rho(r)] = T_{ni}[\rho(r)] + V_{ne}[\rho(r)] + V_{ee}[\rho(r)] + E_{xc}[\rho(r)]$$

where  $T_{ni}$  is the kinetic energy of non-interacting electrons,  $V_{ne}$  is the nuclear-electron interaction,  $V_{ee}$  is the classical electron-electron repulsion and  $E_{xc}$  is the exchange correlation energy of electrons. There are many different expressions for the exchange-correlation energy, which gives rise to the many different flavors of DFT. Earlier versions of this term were calculated exclusively from  $\rho$  at each position (Local Density Approximation, LDA). Evolving from LDA are inclusions of both the density at the local position and the gradient of  $\rho$ , which is known as the gradient correction (Generalized Gradient Approximation, GGA). Further from this, an additional correction for including the dependence of kinetic-energy density can be included (meta-GGA). Lastly a hybridization of both a DFT functional and Hartree-Fock (HF) exchange can be used to calculate the exchange portion of the exchange-correlation energy.

**Basis Sets.** The basis set is a set of mathematical functions, or basis functions, designed to model atomic orbitals (AO). Molecular orbitals (MO) are expressed as linear combinations of the basis functions. From the basis set the wave function that describes the chemical system is constructed. The full wave function is expressed as a Slater determinant formed by the individual occupied MOs. One possibility for a basis functions are Slater-type orbitals (STOs), which have a number of qualities that make them chemically accurate. The mathematical form of a normalized STO is

Eq. (1.6)

$$\varphi(r, \theta, \phi; \zeta, n, l, m) = \frac{(2\zeta)^{n+\frac{1}{2}}}{[(2n)l]^{\frac{1}{2}}} r^{n-1} e^{-\zeta r} Y_l^m(\theta, \phi)$$

where  $\zeta$  is an exponent that depends on the atomic number,  $n$  is the principle quantum number for the valence orbital, and  $Y_l^{ml}$  is the spherical harmonic function with angular momentum and magnetic quantum numbers  $l$  and  $ml$ , respectively. STOs have hydrogenic angular components and correct exponential decay with increasing  $r$  (where  $r$  is the distance from the nucleus), which mirrors the exact orbitals of the hydrogen atom. In order to obtain an analytical solution for an STO, the radial decay can be changed from  $e^{-r}$  to

$e^{-\alpha r^2}$ , making the AO-like function have the form of a Gaussian function. The general functional form of a normalized Gaussian-type orbital (GTO) is

Eq. (1.7)

$$\phi(x, y, z; \alpha, i, j, k) = \left[ \frac{(8\alpha)^{i+j+k} i! j! k!}{(2i)!(2j)!(2k)!} \right]^{\frac{1}{2}} x^i y^j z^k e^{-\alpha(x^2+y^2+z^2)}$$

where  $\alpha$  is an exponent controlling the width of the GTO and  $i$ ,  $j$ , and  $k$  are non-negative integers that describe orbital symmetry in Cartesian coordinates. When the sum of the indices  $i$ ,  $j$ , and  $k$  is zero, one, or two, then the GTO is expressing an s-type, p-type, or d-type orbital, respectively. When the sum of  $i$ ,  $j$ , and  $k$  is one, symmetry is displayed on the corresponding axis, yielding three possible functions which correspond to the  $p_x$ ,  $p_y$ , and  $p_z$  orbitals. When the sum of the indices is two there are 6 possible functions, which express six d-type functions ( $x^2$ ,  $y^2$ ,  $z^2$ ,  $xy$ ,  $xz$ , and  $yz$ ). The advantage of using GTOs is that the one- and two-electron integrals, which arise in electronic structure calculations, are faster to compute and have analytical solutions available. The disadvantages of using a GTO is that the decay of a GTO is too rapid and a cusp is not formed when  $r = 0$ . To overcome these disadvantages, linear combinations of GTOs are used to approximate STOs, which is referred to as a ‘contracted’ basis function. One way to increase computational flexibility is to increase the number of basis functions utilized. Computational efficiency can be increased without loss of accuracy by distinguishing between valence and core AOs by using more and less basis functions, respectively, to represent those AOs. This can be done because valence AOs have more chemical interaction due to chemical bonding than core AOs. The core AOs are typically represented by a single basis function while the valence AOs are represented by multiple basis functions. This is called using a ‘split-valence’ or ‘valence-multiple- $\zeta$ ’ basis set. Predicting accurate molecular geometries becomes difficult when there is insufficient mathematical flexibility in the basis set. To further increase this flexibility, polarization functions are added to basis sets. Polarization adds extra valence functions corresponding to one quantum number higher of angular momentum. This would add d-type functions to second row elements and p-type functions to hydrogen. Electrons in anions or the excited states of molecules are generally more loosely bound than those in cations or neutral compounds. Many errors arise when there is a lack of flexibility to describe these electrons, thus the basis set must accommodate for this phenomena. Adding diffuse functions augments heavy

atoms with an extra s-type orbital and one set of p-type orbitals, while hydrogen atoms are augmented with an extra s-type orbital. The diffuse functions have smaller  $\alpha$  exponents so that the basis functions decay more slowly at longer distances from the nuclei (see equation 1.8). Heavy elements become more computationally expensive to model, in particular due to containing so many electrons. Many of the electrons are not involved in chemical bonding because they lie within the atomic core. To make calculations more efficient the core electrons are replaced with a pseudopotential (ECP) and only the valence (large ECP) or the valence and second outermost electron shells (small ECP) are modeled with basis functions. This effective core potential (ECP) represents the behavior of an atomic core, which includes Coulomb repulsion and adherence to the Pauli principle.

**Geometry Optimizations and the Self Consistent Field.** Obtaining the energy of an arbitrary structure can be interesting, however it may not have much chemical meaning. The lowest energy structure is generally the most probable. In order to discover the “lowest” energy structure a series of geometry optimizations must take place. Initially a guess wave function  $\phi$  is constructed for a molecule as a linear combination of basis functions  $\psi$  (LCAO, or linear combination of atomic orbitals, theory):

Eq. (1.8)

$$\phi = \sum_{i=1}^N \alpha_i \varphi_i$$

where  $\alpha_i$  is a coefficient and N is the number of basis functions  $\psi$ . By arranging equations (1.4) and (1.8) the energy is determined by

Eq. (1.9)

$$E = \frac{\int (\sum_i \alpha_i \varphi_i) \hat{H} (\sum_j \alpha_j \varphi_j)}{\int (\sum_i \alpha_i \varphi_i) (\sum_j \alpha_j \varphi_j)}$$

$$= \frac{\sum_{ij} \alpha_i \alpha_j H_{ij}}{\sum_{ij} \alpha_i \alpha_j S_{ij}}$$

where  $H_{ij}$  is the ‘resonance integral’ and  $S_{ij}$  is the ‘overlap integral’, and both terms are called ‘matrix elements.’ The overlap integral has a clear physical meaning that being the extent to which two basis functions overlap in space. The variational principle instructs that the lower  $E$  represents a better quality (i.e., closer to the ‘real wave function’) wave function. In order for our function (the energy) to be at a minimum, then the derivative with respect to each of the free variables ( $\alpha_i$ ) must be zero. This gives rise to  $N$  equations of the form in equation (1.10) that must be satisfied.

**Eq. (1.10)**

$$\sum_{i=1}^N \alpha_i (H_{ki} - ES_{ki}) = 0$$

A set of  $N$  equations with  $N$  unknowns has a solution if the determinant formed from the coefficients of the unknowns equals zero. Notationally, equation (1.10) becomes

**Eq. (1.11)**

$$\begin{vmatrix} H_{11} - ES_{11} & \cdots & H_{1N} - ES_{1N} \\ \vdots & \ddots & \vdots \\ H_{N1} - ES_{N1} & \cdots & H_{NN} - ES_{NN} \end{vmatrix} = 0$$

which is called a secular equation. From this there will be  $N$  energies  $E_j$  which satisfy this equation. Each value of  $E_j$  will give rise to a different set of coefficients,  $\alpha_{ij}$ , which can be found using equation (1.10) using  $E_j$ . These coefficients will define an optimal wave function within the basis set. Hartree-Fock (HF) theory builds upon Hartree theory by accounting for electron spin and the Pauli exclusion principle. Previously the Hamiltonian operator, equation (1.2), was employed; for HF theory the one-electron Fock operator is used:

**Eq. (1.12)**

$$f_i = -\frac{1}{2} \nabla_i^2 - \sum_k \frac{Z_k}{r_{ik}} + V_i^{HF} \{j\}$$

where the final term is the HF potential, which accounts for Coulomb repulsion between electrons and exchange interactions between electrons of the same spin. This changes the secular equation, equation (1.11), to include the new Fock matrix element  $F_{\mu\nu}$  instead of the resonance integral from Hartree theory (the overlap integral  $S$  is unchanged).  $F_{\mu\nu}$  takes on the form:



Eq. (1.13)

$$F_{\mu\nu} = \left\langle \mu \left| -\frac{1}{2} \nabla^2 \right| \nu \right\rangle - \sum_k^{\text{nuclei}} Z_k \left\langle \mu \left| \frac{1}{r_k} \right| \nu \right\rangle + \sum_{\lambda\sigma} P_{\lambda\sigma} \left[ \langle \mu\nu | \lambda\sigma \rangle - \frac{1}{2} \langle \mu\lambda | \nu\sigma \rangle \right]$$

The first two terms are one-electron integrals that represent the kinetic energy of an electron and electron-nuclear attraction, respectively. The last terms are two-electron integrals that represent coulomb repulsion and exchange interactions between electrons. Like in Hartree theory, HF follows a procedure where an initial wave function is guessed. From the initial wave function the density matrix is computed, and the HF secular equation is constructed and a new set of orbital coefficients is solved. If the new density matrix is sufficiently similar to the old matrix, the SCF process is concluded with the energy and wave function for the molecular geometry having been determined. Then the current molecular geometry is checked to see if it satisfies the optimization criteria. If the geometry does not satisfy the optimization criteria, then a new geometry is produced according to an optimization algorithm. This new geometry is then subjected to the same process again until the optimization criteria are satisfied. A summary of these steps is tabulated in table 1. It is common for optimization criteria to include thresholds for the root mean square and maximum deviation of atomic positions between geometry steps and the average and maximum first derivative of energy versus atomic positions.

Step	Action
1	Determine basis set; guess initial wave function; calculate initial density matrix
2	Determine matrix elements
3	Create HF equation and solve for N of E <sub>j</sub>
4	Determine new density matrix; if the old and new are not similar then start again from step 2
5	Check if molecular geometry satisfies opt criteria; if not then new geometry is chosen according to optimization algorithm and start again from step 2
6	Output optimized geometry data

**Table1.** Summary of the HF SCF process.

This process is analogous in DFT, with the exception that it use the Kohn-Sham one-electron operator:

**Eq. (1.14)**

$$h_i^{KS} = -\frac{1}{2} \nabla_i^2 - \sum_k^{nuclei} \frac{Z_k}{|r_i - r_k|} + \int \frac{\rho(r')}{|r_i - r'|} dr' + V_{xc}$$

where  $\rho$  is electron density and  $V_{xc}$  is a functional-derivative, equation (1.15), which accounts for the exchange-correlation potential.

**Eq. (1.15)**

$$V_{xc} = \frac{\delta E_{xc}}{\delta \rho}$$

Just like with HF theory, there is a secular equation to be solved, however  $F_{\mu\nu}$  is replaced with  $K_{\mu\nu}$ :

**Eq. (1.16)**

$$K_{\mu\nu} = \left\langle \phi_{\mu} \left| -\frac{1}{2} \nabla^2 - \sum_k^{\text{nuclei}} \frac{Z_k}{|r-r_k|} + \int \frac{\rho(r')}{|r-r'|} dr' + V_{xc} \right| \phi_{\nu} \right\rangle$$

These are used in an analogous SCF process for DFT, just as in HF calculations.

**Thermodynamic Data.** In the previous section a guide for the SCF and geometry optimization processes was discussed. However, there are more steps that must be completed in order to obtain the proper thermodynamic data. The absolute Gibbs energy ( $G$ ) of a compound is the sum of the electronic energy ( $E_{\text{elec}}$ ), the sum of the thermal contributions to the enthalpy ( $H_{\text{thermal}}$ ), zero point energy (ZPE,  $E_{\text{ZPE}}$ ) and the thermal contributions to the entropy ( $S$ ).

Eq. (1.17)

$$G = (E_{\text{elec}} + H_{\text{thermal}} + E_{\text{ZPE}}) - TS$$

The electronic energy is sensitive to the size of the basis set. To obtain a more accurate electronic energy, the final geometry from an optimization is taken and a singlepoint calculation is carried out using a slightly larger basis set (e.g., a geometry is optimized with a double-zeta basis set, and the electronic energy is recalculated with a triple-zeta basis set). The zero point energy is the sum of the energies from the lowest vibrational level for each vibration ( $\omega$ ), which is derived from the harmonic oscillator approximation

Eq. (1.18)

$$E_{\text{ZPE}} = \sum_i^{\text{modes}} \frac{1}{2} h\omega_i$$

The thermal contribution to the enthalpy is the sum of the individual enthalpies for translation ( $H_{\text{trans}}$ ), rotation ( $H_{\text{rot}}$ ), vibration ( $H_{\text{vib}}$ ) and electronics ( $H_{\text{elec}}$ ). This is analogous for the thermal contribution to the entropy.

**Theoretical calculations applied to bioinorganic chemistry.** The last section of the paragraph is dedicated to a brief description of coordination metal ions in biomolecules and how it need to be done at all levels of the system description. It has been a natural consequence of the recent progress in quantum chemical methodology that the theoretical chemistry may complement and, at the same time, rival their experimental counterparts<sup>25,26</sup>. The major advantage of using quantum chemistry in studies of

biomolecules is complementarity of information that can be obtained from the calculations. The energy profile changes in electron density and molecular structures, including the transition state structures along a reaction pathway, are important system descriptors which are difficult to obtain by other techniques. Thus, it is nowadays possible to conveniently model systems containing up to 500 atoms using standard techniques, such as the popular Density Functional Theory (DFT) method. This size of the system is not accessible for the high-level wavefunction methods; however, recent advances have considerably extended our possibilities in their usage for bioinorganic systems of a realistic size (approaching 100 atoms).

First principles molecular dynamics simulations (Car-Parrinello simulations) open up new avenues for studying transition metal centers and enable several questions to be addressed that cannot be resolved with either standard quantum chemical or traditional force-field methods. The quantum chemical methods used in bioinorganic chemistry are dominantly of the Density Functional Theory (DFT) type, given their appreciable performance ratio. The question of the correct electron count is an important one for bioinorganic chemists because the concept of the  $d^N$  electron configuration has proven to be a powerful guide to the properties and reactivities of transition metal complexes. Theoretical investigation are used as an integral part of the data analysis or as an *a posteriori* justification of the conclusion that were reached. Its quality and reliability are assessed by comparing the calculated data with their experimental counterparts.

## V. Instrumental Details

### V.I. IRMPD Spectroscopy: ESI FT-ICR coupled with FEL and OPO/OPA Lasers

The experiments in this thesis were carried out with two different equipments, each one based on the coupling of a mass spectrometer with a IR laser source. The first set-up consists of a commercial APEX-Qe Bruker hybrid Fourier transform ion cyclotron resonance tandem mass spectrometer equipped with a 7.0 T actively shielded superconducting magnet and a quadrupole-hexapole interface for mass-filtering and ion accumulation, under control by the commercial software APEX 1.0.

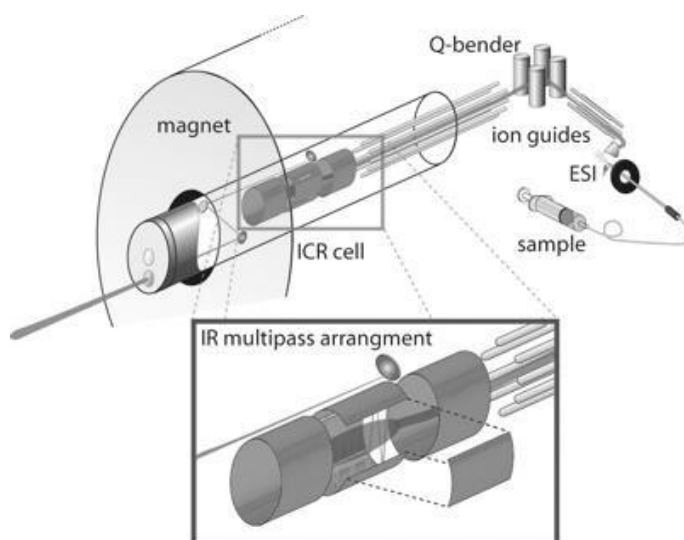


**Figure 2.** Schematic of the instruments and a detailed view of the ICR cell with the IR laser beam entering.

After electrospray ionization delivering the species of interest, ions are guided through a capillary and an ion funnel into a first hexapole ion trap, where they are collected for typically about 20 ms. One or multiple bunches of ions are then pulse-extracted into a 20 cm long rf quadrupole ion guide, where mass selection can be performed by resonant RF ejection of other species present. Ions are then collected in a 5 cm long hexapole cell, where they are collisionally cooled using a flow of high-purity Argon. A typical collection time in the hexapole collision cell is 500-1000 ms, although in other experiments species are collected for periods as short as 1 ms. Ions are then pulse-extracted toward the ICR cell, where they are irradiated by IR light for a fixed time period. For each wavelength, the

mass spectrum is the Fourier transform of a time-domain transient averaged three times. The 63 mm long infinity ICR cell is placed inside the 155 mm diameter bore of a 7 T superconducting magnet (Magnex). Before entering the ICR cell, the ions are decelerated by two ring electrodes of which the one closest to the trapping electrodes is segmented into two half-electrodes, allowing for a more efficient trapping by transferring longitudinal beam energy into transversal beam energy, or for a correction of transversal beam energies. A 3.45 mm diameter aperture in the cathode allows for IR laser beam to enter the cell. The IR light then transverses the ICR cell along the axis of the bore of the magnet in a singlepass configuration. The IR laser beam is loosely focused using a 2 m focal mirror and has a nearly constant diameter throughout the cell region. IR spectroscopy in 650-2200  $\text{cm}^{-1}$  wavenumber range was performed using the CLIO FEL, which produces pulsed, tunable IR light covering the 600-2200  $\text{cm}^{-1}$  wavenumber range (4-100  $\mu\text{m}$ ). Typical energies reached within one macropulse can be 40-60 mJ.

A LaserVision OPO/OPA coupled to a Paul ion trap tandem mass spectrometer (Esquire 6000+, Bruker Inc.) was employed to explore the 2900–3700  $\text{cm}^{-1}$  spectral region of the different species under study. This parametric converter was pumped by a Continuum Surlite II non-seeded Nd:YAG laser operating at 10 Hz repetition rate. The typical pulse width of this pump laser is 4–6 ns, with output pulse energy of 600 mJ at 1064 nm. The OPO/OPA laser is tunable within 2800–4000  $\text{cm}^{-1}$ , and tunability is achieved by angle fine-adjusting of OPO and OPA crystals simultaneously. The angle tuning is controlled precisely using software-controlled stepping motors. The typical output energy from the OPO/OPA laser was 20 mJ/pulse in the investigated spectral range with 3–4  $\text{cm}^{-1}$  bandwidth. IR beam focusing is performed to achieve better overlap with the trapped ion cloud. In the trap, ions were accumulated for 3–50 ms prior to IR irradiation. Multistage mass spectrometry was performed using the standard Bruker Esquire Control (v5.2) software. The typical irradiation time used in the present experiments was 0.5–2 s. The irradiation time was controlled using an electromechanical shutter synchronized precisely with the mass spectrometer.

If the IR beam is in resonance with a strongly IR-active vibrational mode, light can be absorbed by the ions and the sequential absorption of several IR photon can lead to fragmentation of the mass-selected ions. By recording the number of detected ions, the parent mass channel and that in the fragment channels while varying the wavelength of the

IR light, an IRMPD spectrum is obtained. The IRMPD spectra are obtained by plotting the photofragmentation yield  $R$  ( $R = -\ln[I_{\text{parent}}/(I_{\text{parent}} + \sum I_{\text{fragment}})]$ , where  $I_{\text{parent}}$  and  $I_{\text{fragment}}$  are the integrated intensities of the mass peaks of the precursor and of the fragment ions, respectively) as a function of the frequency of the IR radiation<sup>27</sup>.

## V.II. ESI-MS/MS Mass Spectrometry: Triple Quadrupole Linear Ion Trap Mass Spectrometer

ESI-MS/MS experiments were performed with a Triple Quadrupole Linear Ion Trap (LIT) mass spectrometer (APPLIED Biosystems Linear Ion Trap API 2000) equipped with an ESI ion source. A layout of the instruments is shown in **Figure 2**.

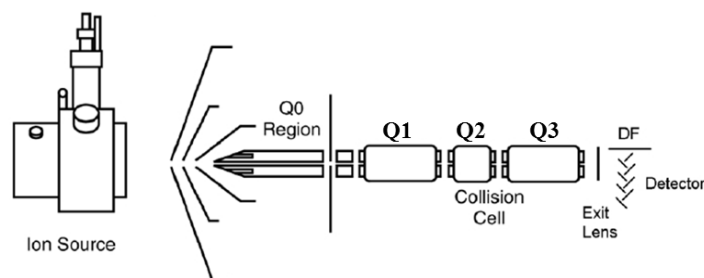


**Figure 2.** Scheme of the Triple Quadrupole Linear Ion Trap mass spectrometer.

Ion are extracted from the solution by an ESI source and transferred in Q0 where they are accumulated and guided toward Q1 by the potential applied to the skimmer. The space between the curtain plate and the orifice plate is constantly filled with dry  $N_2$  in order to avoid most of the solvent from entering the Q0 region, which is maintained at  $8 \times 10^{-3}$  torr by a turbomolecular pump. Ions are then guided in Q1, q2 and Q3 region by the IQ1-IQ3 radiofrequency lens. Q1, q2 and Q3 (LIT) are modulated by a radiofrequency and a direct current DC. A supplementary AC current is applied to Q3 for MS/MS/MS experiments. q2 is filled with dry  $N_2$  (collision gas, CAD gas) at  $2-4 \times 10^{-5}$  torr and connected to Q3 by an orifice through which a minimal amount of CAD gas is able to reach the Q3 region and then to be used for successive CID experiments. A DC current is applied in Q3 to allow the isolation of an ionic species by stabilizing its trajectory inside the trap while destabilizing all the others; the AC current is used for a resonant excitation of the isolated ion. Thus ions coming from q2 can be manipulated in Q3 by means of several techniques:

- Ion trapping: Ions are confined in Q3 applying the rf and the DC current;
- Ion isolation: the rf is spanned in order to destabilize all the ions trajectories but the one of the ion to be isolated;
- Ion excitation: a supplementary resonant AC voltage is applied thus increasing the translational energy of the isolated ion;
- Ion ejection: before ions detection, the rf is linearly increased and a supplementary AC voltage is applied, thus destabilizing the ionic trajectories and expelling the ions from the trap;
- Ion detection: ions are accelerated towards two dynodes over and below the trap;

For our purpose, mass spectra were recorded in three different modalities: Enhanced Product Ion Scan. In this scan mode, the precursor ion to be fragmented is the first selected in Q1, filtering out all other ions. The precursor ion is fragmented by collisionally-activated dissociation (CAD) in the q2 collision cell. The fragment ions generated are captured in the ion trap; then scanned out at a fast scan speed.



### V.III. References

- (1) Lippard, S. J.; Berg, J. M. *Principles of Bioinorganic Chemistry*; University Science Books, 1994.
- (2) Beinert, H. Bioinorganic Chemistry: a New Field or Discipline? Words, Meanings, and Reality *J. Biol. Chem.* **2002**, *277*, 37967-37972.
- (3) Beinert, H.; Emptage, M. H.; Dreyer, J. L.; Scott, R. A.; Hahn, J. E.; Hodgson, K. O.; Thomson, A. J. Iron-Sulfur Stoichiometry and Structure of Iron-Sulfur Clusters in Three-Iron Proteins: Evidence for [3Fe-4S] Clusters *PNAS* **1983**, *80*, 393-396.
- (4) Glaser, T.; Rose, K.; Shadle, S. E.; Hedman, B.; Hodgson, K. O.; Solomon, E. I. S K-edge X-ray Absorption Studies of Tetranuclear Iron-Sulfur Clusters:  $\mu$ -Sulfide Bonding and Its Contribution to Electron Delocalization *J. Am. Chem. Soc.* **2001**, *123*, 442-454.
- (5) Anxolabehere-Mallart, E.; Glaser, T.; Frank, P.; Aliverti, A.; Zanetti, G.; Hedman, B.; Hodgson, K. O.; Solomon, E. I. Sulfur K-edge X-ray Absorption Spectroscopy of 2Fe-2S Ferredoxin: Covalency of the Oxidized and Reduced 2Fe Forms and Comparison to Model Complexes *J. Am. Chem. Soc.* **2001**, *123*, 5444-5452.
- (6) Bertini, I.; Luchinat, C.; Parigi, G. *Solution NMR of paramagnetic molecules : applications to metalloproteins and models*; Elsevier Science Ltd.: Amsterdam ; New York, 2001.
- (7) Banci, L.; Bertini, I.; Ciurli, S.; Ferretti, S.; Luchinat, C.; Piccioli, M. The Electronic Structure of  $[\text{Fe}_4\text{S}_4]^{3+}$  Clusters in Proteins. An Investigation of the Oxidized High-Potential Iron-Sulfur Protein II from *Ectothiorhodospira Vacuolata* *Biochemistry* **1993**, *32*, 9387-9397.
- (8) Polfer, N. C.; Oomens, J. Vibrational Spectroscopy of Bare and Solvated Ionic Complexes of Biological Relevance *Mass. Spectrom. Rev.* **2009**, *28*, 468-494.
- (9) Petrie, S. Getting a Theoretical Handle on Fullerene Ions: Quantum Chemical Calculations on the Reactions of  $\text{C}_6\text{O}^+$ ,  $\text{C}_6\text{O}_2^+$  and  $\text{C}_6\text{O}_3^+$  with Ammonia *Int. J. Mass. Spectrom.* **2006**, *255-256*, 213-224.
- (10) Meijer, G.; de Vries, M. S.; Hunziker, H. E.; Wendt, H. R. Laser Desorption Jet-Cooling Spectroscopy of para-Amino Benzoic Acid Monomer, Dimer, and Clusters *J. Chem. Phys.* **1990**, *92*, 7625-7635.
- (11) Polfer, N. C.; Oomens, J.; Dunbar, R. C. IRMPD Spectroscopy of Metal-Ion/Tryptophan Complexes *Phys. Chem. Chem. Phys.* **2006**, *8*, 2744-2751.
- (12) Surya, P. I.; Roth, L. M.; Ranatunga, D. R. A.; Freiser, B. S. Infrared Multiphoton Dissociation of Transition Metal Containing Ions:  $\text{MC}_n\text{H}_2^{n+}$  (M = Fe, Co, Ni; n = 2-5) *J. Am. Chem. Soc.* **1996**, *118*, 1118-1125.
- (13) Oomens, J.; Polfer, N.; Moore, D. T.; van der Meer, L.; Marshall, A. G.; Eyler, J. R.; Meijer, G.; von Helden, G. Charge-State Resolved Mid-Infrared Spectroscopy of a Gas-Phase Protein *Phys. Chem. Chem. Phys.* **2005**, *7*, 1345-1348.
- (14) Angelelli, F.; Chiavarino, B.; Crestoni, M. E.; Fornarini, S. Binding of gaseous Fe(III)-heme Cation to Model Biological Molecules: Direct Association and Ligand Transfer Reactions *J. Am. Soc. Mass. Spectrom.* **2005**, *16*, 589-598.
- (15) Crestoni, M. E.; Fornarini, S. Heme-Peptide/Protein Ions and Phosphorous Ligands: Search for Site-Specific Addition Reactions *J. Biol. Inorg. Chem.* **2007**, *12*, 22-35.
- (16) Chiavarino, B.; Crestoni, M. E.; Fornarini, S.; Rovira, C. Protonated Heme *Chemistry* **2007**, *13*, 776-785.
- (17) Crestoni, M. E.; Fornarini, S. Compound I of Naked Heme (iron protoporphyrin IX) *Inorg. Chem.* **2007**, *46*, 9018-9020.
- (18) Lobinski, R. Characterizing Speciation of Trace Elements in the Chemistry of Life *J. Anal. Chem.* **2001**, *369*, 113-114.
- (19) Fenn, J. B.; Mann, M.; Meng, C. K.; Wong, S. F.; Whitehouse, C. M. Electrospray Ionization for Mass-Spectrometry of Large Biomolecules *Science* **1989**, *246*, 64-71.
- (20) Karas, M.; Hillenkamp, F. Laser Desorption Ionization of Proteins with Molecular Masses Exceeding 10000 Daltons *Anal. Chem.* **1988**, *60*, 2299-2301.
- (21) Peng, J. M.; Gygi, S. P. Proteomics: the Move to Mixtures *J. Mass. Spectrom.* **2001**, *36*, 1083-1091.

- (22) Hancock, W. S.; Wu, S. L.; Shieh, P. The Challenges of Developing a Sound Proteomics Strategy *Proteomics* **2002**, 2, 352-359.
- (23) Vaisar, T.; Gatlin, C. L.; Turecek, F. Metal-ligand Redox Reactions in Gas-Phase Quaternary Peptide-Metal Complexes by Electrospray Ionization Mass Spectrometry *Int. J. Mass. Spectrom.* **1997**, 162, 77-87.
- (24) Armentrout, P. B.; Ervin, K. M.; Rodgers, M. T. Statistical Rate Theory and Kinetic Energy-Resolved Ion Chemistry: Theory and Applications *J. Phys. Chem. A* **2008**, 112, 10071-10085.
- (25) Senn, H. M.; Thiel, W. QM/MM Methods for Biomolecular Systems *Ang. Chem.* **2009**, 48, 1198-1229.
- (26) Warshel, A.; Sharma, P. K.; Kato, M.; Xiang, Y.; Liu, H.; Olsson, M. H. Electrostatic Basis for Enzyme Catalysis *Chem. Rev.* **2006**, 106, 3210-3235.
- (27) Lemaire, J.; Boissel, P.; Heninger, M.; Mauclaire, G.; Bellec, G.; Mestdagh, H.; Simon, A.; Le Caer, S.; Ortega, J. M.; Glotin, F.; Maitre, P. Gas-phase Infrared Spectroscopy of Selectively Prepared Ions *Phys. Rev. Lett.* **2002**, 89, 273002.

CHAPTER 1

**Isomeric  $C_5H_{11}Si^+$  ions from the trimethylsilylation of acetylene:  
an experimental and theoretical study**

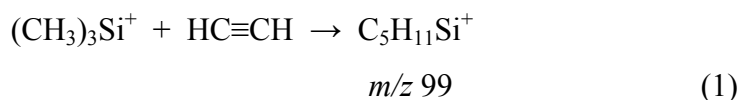
**DOI: [10.1016/j.ijms.2012.10.007](https://doi.org/10.1016/j.ijms.2012.10.007)**

## 1.1. Introduction

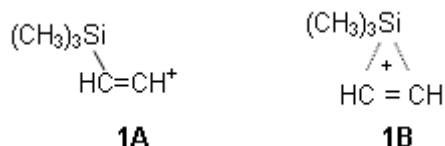
The electrophilic silylation of hydrocarbons can in principle be obtained by delivering a formal  $R_3Si^+$  species on an unsaturated compound. However, the neat process is not easily accomplished in solution. Indeed, trivalent  $R_3Si^+$  silylium ions are hardly accessible in condensed phases due to their high reactivity and enormous electrophilicity, though being thermodynamically more stable than equally substituted carbenium ions<sup>1-12</sup>. In recent years considerable efforts have been devoted to the development of powerful sources of “ $R_3Si^+$ ” and conventional trialkylsilyl triflate reagents have been surpassed by reagents based on carborane anions<sup>13</sup>. Although the  $R_3Si$  (carborane) species do not contain free silylium ions they may react like silylium ions. Still, the silylation of a weak base such as benzene has yet to be established in the condensed phase<sup>13-15</sup>. An ideal environment where  $R_3Si^+$  ions can be easily generated and studied is the gas-phase<sup>16-17</sup>. In this medium the formation of trimethylsilylbenzene from the reaction of  $(CH_3)_3Si^+$  with benzene and neutralization by a strong nitrogen base was obtained<sup>18-22</sup>. In this gas-phase work it was recognized for the first time that the formation of the intermediate silylated  $\sigma$ -complex was promptly achieved but the critical step to obtain neutral phenylsilane was the deprotonation of the intermediate. Following these gas-phase studies demonstrating the key role of deprotonation, the aromatic silylation of toluene by  $R_3SiCl$  under  $AlCl_3$  catalysis has been successfully accomplished in the presence of hindered tertiary amines by Olah et al, although in only moderate yield<sup>23</sup>. In the gas-phase, not only benzene but also toluene and other aromatic and heteroaromatic compounds have been successfully silylated<sup>24-28</sup>. The silylium ions were formed in a gaseous environment at atmospheric pressure using a radiolytic approach<sup>29</sup>. Also a nucleogenic approach based on the  $\beta$ -decay of tritium has been used to generate silylium ions in the gas-phase and the reaction with  $\pi$ -nucleophiles has been reported<sup>30-33</sup>.

In the gas-phase at atmospheric pressure  $(CH_3)_3Si^+$  ions are found to react with acetylene yielding a substitution product, namely  $(CH_3)_3SiC\equiv CH$ <sup>34</sup>. However, mass spectrometric studies on the reaction of  $(CH_3)_3Si^+$  with acetylene have yielded apparently contrasting results. In high pressure mass spectrometry (HPMS) operating at 3–5 mbar,  $Me_3Si^+$  appears to be unreactive with acetylene (i.e. it does not yield the expected adduct ion) and the ion is ultimately captured by adventitious water<sup>35</sup>, a potent nucleophile toward

silylium ions. Quite in contrast, operating at  $10^{-8}$ – $10^{-7}$  mbar in the cell of an FT-ICR mass spectrometer, the formation of an adduct ion at  $m/z$  99 from the reaction of  $(\text{CH}_3)_3\text{Si}^+$  with acetylene has been reported to occur<sup>36</sup>, albeit with low efficiency (0.013, as measured by the ratio  $k_{\text{exp}}/k_{\text{coll}}$ , where  $k_{\text{exp}}$  is the bimolecular rate constant for reaction (1) and  $k_{\text{coll}}$  is the calculated collision rate constant)<sup>37</sup>.

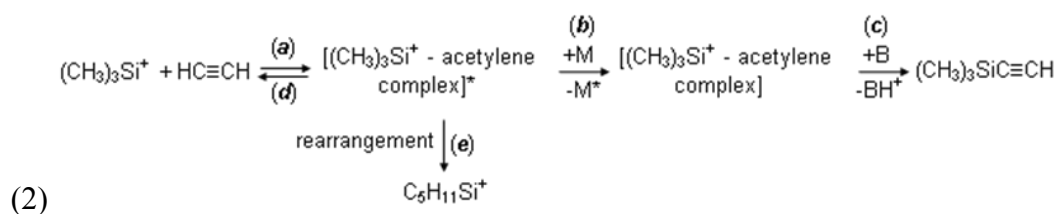


The nascent ionic addition product from the reaction of  $(\text{CH}_3)_3\text{Si}^+$  with acetylene may be assigned the structure of an unrearranged species with the features of a  $\beta$ -silyl-substituted vinyl cation (1A), possibly acquiring a cyclic geometry (1B)<sup>38-41</sup>.



$\beta$ -silyl hyperconjugative stabilization of viny cations is well documented. In solution  $\beta$ -silyl-substituted vinyl cation can be generated by protonation of silyl substituted allenes<sup>42</sup> and silyl substituted alkynes<sup>43-46</sup> under carefully controlled experimental conditions in non-nucleophilic solvents and by addition of incipient silylium ions to alkynes in the presence of inert counterions<sup>47-49</sup>. The determination of the X-ray structure of a vinyl cation stabilized by two  $\beta$ -silyl substituents has also been achieved<sup>50</sup>. The  $\beta$ -silyl effect, stabilizing a positively charged carbon, exerts a strong influence on gaseous carbenium ions<sup>51-57</sup> and the formation of an intermediate resembling 1A or 1B is inferred from the formation of the  $(\text{CH}_3)_3\text{SiC}\equiv\text{CH}$  substitution product in the experiments at atmospheric pressure, run in the presence of a strong base<sup>34</sup>. However, the structure of the adduct at  $m/z$  99 formed in the FT-ICR cell does not respond to any kind of behavior expected from a species like 1A or 1B. For example, the reaction with water, expected to yield  $(\text{CH}_3)_3\text{SiOH}_2^+$  by  $(\text{CH}_3)_3\text{Si}^+$  transfer to the oxygen nucleophile, leads rather to  $(\text{CH}_3)_2\text{SiOH}^+$  with concomitant loss of  $\text{C}_3\text{H}_6$ , an indication that a rearrangement process has taken place. The same  $\text{C}_3\text{H}_6$  neutral is lost in collision-induced dissociation (CID) as the prevailing fragmentation channel. A unifying justification for the observed reactivity pattern has been put forward, based on the different pressure range prevailing in the three

experiments, as illustrated in Eq. (2)<sup>36</sup>. At nearly atmospheric pressure, the adduct ions,  $[(\text{CH}_3)_3\text{Si}^+ \text{-acetylene complex}]^*$ , primarily excited by the exothermicity of the formation process (step (a) in Eq. (2)), undergo an efficient cooling by collisions with unreactive molecules (M) of the bath gas (step (b) in Eq. (2)), thus allowing the formation of thermalized adduct ions,  $[(\text{CH}_3)_3\text{Si}^+ \text{-acetylene complex}]$ , that can subsequently be deprotonated to yield the substitution product  $(\text{CH}_3)_3\text{SiC}\equiv\text{CH}$  (step (c) in Eq. (2))<sup>34</sup>.



In the 3-5 mbar environment of the HPMS experiments the  $[(\text{CH}_3)_3\text{Si}^+ \text{-acetylene complex}]$  is apparently a fleeting species, undergoing fast desilylation by ubiquitous water. However, it is only at the  $10^{-8}$  -  $10^{-7}$  mbar pressure in the FT-ICR cell that the excess energy released in the adduct ion may not be dissipated (unless by radiative emission, a poorly efficient process in a small molecule)<sup>58-60</sup> and remains available to surmount the activation energy barriers leading to rearranged ions  $\text{C}_5\text{H}_{11}\text{Si}^+$  (step (e) in Eq. (2)). The latter species, that reasonably lie in a deeper energy well, become resistant to dissociation under the prevailing environmental conditions. Probing these suggested rearrangement processes and uncovering the structure of the end product ions was the aim of the present contribution. The problem has been tackled with a combined approach based on bimolecular ion-molecule reactions with appropriate neutrals as diagnostic tools to test ion structures and on ab initio calculations to assist in assigning plausible rearrangement pathways. The study of this system (namely  $(\text{CH}_3)_3\text{Si}^+ + \text{HC}\equiv\text{CH}$ ) lends itself to uncover important issues in the reactivity of silyl-substituted carbenium ions and silacations such as the thermodynamic drive to the most stable species on the  $\text{C}_5\text{H}_{11}\text{Si}^+$  potential energy surface, the electronic factors affecting their stability, the kinetic barriers involved in the rearrangement processes, representing a number of fundamental questions about the chemistry of these reactive intermediates.

## 1.2. Experimental Details

### 1.2.1. Materials

The hydrocarbons CH<sub>4</sub>, C<sub>2</sub>H<sub>2</sub>, and C<sub>3</sub>H<sub>8</sub> were high-purity (99.9 mol %) gases from Matheson Gas Products Inc. The other chemicals used as reagents or as precursors of desired ions were purchased from Sigma-Aldrich. The silylated alkenes that were not commercially available were prepared from the Wurtz-Fittig reaction of (CH<sub>3</sub>)<sub>3</sub>SiCl with the appropriate alkenyl bromide<sup>61</sup> and were purified by preparative GLC using a 4-m long, 4-mm i.d. stainless steel column, packed with 5% DC 200 methylsilicone on Supelcoport. Their identity was verified by NMR spectroscopy and mass spectrometry.

### 1.2.2. FT-ICR Mass Spectrometry

The experiments were performed with a Bruker Spectrospin Apex TM 47e mass spectrometer equipped with a cylindrical “infinity” cell within a 4.7 T superconducting magnet and with an external ion source. In this source, the chemical ionization (CI) of a neutral admitted through a probe for volatile compounds is effected by the ions of a chosen CI reagent, ionized by a 200eV electron beam. The ions formed in the external source are led into the FT-ICR cell by an ion guide that should not impart any excess translational energy to the ions. The ions can be further allowed to equilibrate at the room temperature of the FT-ICR cell by unreactive collisions with argon, admitted in the cell at 10<sup>-5</sup> mbar by a pulsed valve. After a delay time the ions of interest were selected by ejecting unwanted ions using rf sweeps and single shots. The selected ions were then let to react with a neutral reagent leaked in the cell by a needle valve at a constant pressure, typically in the range of 10<sup>-8</sup> - 10<sup>-7</sup> mbar. The pressure readings were obtained by a cold cathode gauge calibrated using the rate constant value of 1.1 × 10<sup>-9</sup> cm<sup>3</sup> s<sup>-1</sup> for the reference reaction CH<sub>4</sub><sup>+</sup> + CH<sub>4</sub> → CH<sub>3</sub><sup>+</sup> + CH<sub>5</sub><sup>+</sup>, and corrected using individual response factors<sup>62-63</sup>. The kinetics of the ion-molecule reactions were monitored by recording 10 - 20 averaged scans for each mass spectrum in series of runs corresponding to increasing reaction time. In these conditions the kinetics are pseudo first order and the rate constants (k<sub>obs</sub>) were obtained from the slope of the semilogarithmic decrease of reactant ion abundance versus reaction time. The

pseudo first order rate constants divided by the substrate concentration yield the bimolecular rate constants ( $k_{\text{exp}}$ ). Their values have an estimated error ( $\pm 30\%$ ) largely due to the uncertainty affecting the pressure reading of the neutral. The reported  $k_{\text{exp}}$  values are the average of at least three values for kinetic runs at different neutral pressure. The reaction efficiencies ( $\Phi$ ) were calculated as % ratio of  $k_{\text{exp}}$  relative to the collision rate constant ( $k_c$ ) calculated by the parameterized trajectory theory<sup>37</sup>. The elemental composition of the product ions was verified by  $m/z$  measurements at high resolution.

### 1.2.3. Computational Details

The quantum chemical calculations were performed using the Gaussian 09 suites of programs<sup>64</sup>. All structures were fully optimized using standard methods (Density Functional Theory (DFT) hybrid methods with the B3LYP functional). The 6-311G(2d,p) basis set was used for geometry optimizations and frequency calculations. Analytical vibrational analyses at the same level were performed to determine the zero-point vibrational energy (ZPE) and to ascertain each stationary point as a minimum or first-order saddle point. Corrections for ZPE (not scaled) are included in the calculated energies. All transition states were found by using QST2 and QST3 methods and their correct connection with the relative reagents and products was verified by means of intrinsic reaction coordinate calculations<sup>65,66</sup>. Extra valence functions and polarization functions as in the 6-311++G(2d,2p) basis set were used to allow CCSD(T)/6-311++G(2d,2p) energy calculations of B3LYP/6-311G(2d,p) optimized geometries. In order to further check the reliability of the obtained geometries, MP2 optimizations have also been performed with the same basis set on few exemplary structures. MP2/6-311G(2d,p) geometries display very small differences, showing that B3LYP/6-311G(2d,p) can give a good description of the geometrical features of the investigated system. Thus, the relative energies, interconversion pathways and transition state structures that are finally reported were evaluated at CCSD(T)/6-311++G(2d,2p)//B3LYP/6-311G(2d,p) level of theory.



## 1.3. Results and Discussion

### 1.3.1. Sample Ion(s) and Model Ions

The ion (or, possibly, ion mixture) of interest is the adduct at  $m/z$  99 formed from the addition of  $(\text{CH}_3)_3\text{Si}^+$  (obtained by chemical ionization of  $(\text{CH}_3)_4\text{Si}$  using  $\text{CH}_4$  gas) to acetylene in the cell of an FT-ICR mass spectrometer, henceforth named sample ion(s) **S**. In order to obtain experimental information that could allow a structural assignment to this species, model ions were sought whose reactivity behavior, compared with that of the sample ion **S**, can yield diagnostic information. To this end a number of Me<sub>3</sub>Si-substituted propenes have been synthesized, namely 2-(trimethylsilyl)propene, allyltrimethylsilane, (E)- and (Z)-1-(trimethylsilyl)propene. The chemical ionization (CI) using  $\text{C}_3\text{H}_8$  as neutral precursor of reagent  $\text{C}_3\text{H}_7^+$  ions forms abundant  $\text{C}_5\text{H}_{11}\text{Si}^+$  product ions that are expected to retain the structure of the parent neutrals. The ensuing species (labeled **2,3,4,6**) are depicted in Chart 1 together with the trimethylsilyl cation complex with acetylene (**1**) and an  $\alpha$ -silylvinyl cation (**5**) that may be involved as transient intermediate. Their reactivity behavior toward selected reagents is demonstrated to be quite distinct for each one of them (with the possible exception of the (E)- and (Z)-isomers of 1-propenyl-dimethylsilyl cation, i. e. **2** and **4**), supporting the idea that the mild CI by  $\text{C}_3\text{H}_7^+$  ions, while able to abstract a methide anion<sup>16,67</sup>, does not confer any excess energy to the incipient silyl cation that could activate subsequent rearrangement processes. The notable stability of the silicon containing cations, in which the charge is located on a silicon atom, is the driving force of the reaction, as found responsible for example for the facile cleavage of a Si-C bond in radical cations<sup>17,68</sup>. The distinct behavior of so-formed species **2,3,4,6** (and therefore their distinct structure) is retained also when they are formed by the more fierce CI by  $\text{CH}_5^+$  ions and, conversely, when the ions are submitted to collisional relaxation by a pulse of argon at  $10^{-5}$  bar.

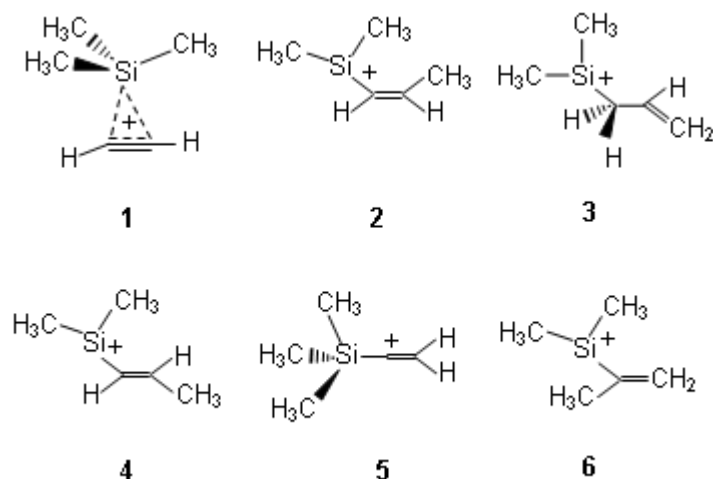
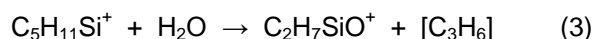


**Chart 1.** Distinct possible structures for  $C_5H_{11}Si^+$  isomers.

### 1.3.2. Ion-Molecule Reactions of $C_5H_{11}Si^+$ Ions

CID experiments on ion **S** have suggested the formation of a covalent Si-C bond in an addition product that subsequently evolves by loss of  $C_3H_6$ . However, CID is not structurally diagnostic for simple alkylsilyl cations<sup>69</sup> and any characterization using this tool was not further attempted. Ion-molecule reactions appear as more selective probes for structural elucidation. In particular, one may rely on the well established notion that cations in which the positive charge is borne by the silicon atom are powerful electrophiles and tend to form strong covalent bonds with various compounds containing electronegative atoms including water, alcohols and amines<sup>70</sup>. Accordingly, potentially diagnostic reagents have been sought in the ROR' class of compounds ( $R,R' = H,H; i-C_3H_7,H; t-C_4H_9,CH_3$ ), though preliminary experiments were run to explore also the reactivity towards alkyl chlorides such as  $C_3H_5Cl$  and  $t-C_4H_9Cl$ . The reactions of both the sample ion **S** and the model ions (**2,3,4,6**) have been studied by allowing the ions formed in the external ions source to react with the neutral present in the FT-ICR cell at a controlled pressure value in the range of  $10^{-8} - 10^{-7}$  mbar. The reaction with water leads to a unique product ion of  $C_2H_7SiO^+$  composition, likely corresponding to  $(CH_3)_2SiOH^+$  [Eq. (3)].



An exemplary plot of the time dependence of ion abundances is reported in Fig. 1, illustrating the reaction of model ion **3**, from  $\text{Cl}(\text{C}_3\text{H}_8)$  of allyltrimethylsilane. The second order rate constants were obtained from kinetics run at three or more different values of the  $\text{H}_2\text{O}$  pressure and found to yield the same value within experimental error. The results are listed in Table 1 showing that  $\text{C}_5\text{H}_{11}\text{Si}^+$  ions display the same reactivity with water, irrespective of their origin. This reagent is therefore unsuitable to discriminate among the different structures of the model ions.

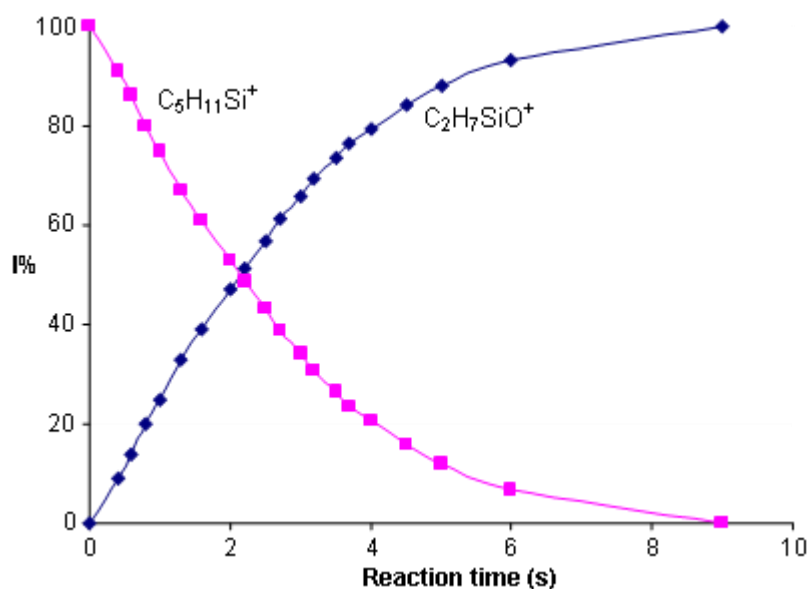


**Fig. 1.** Time dependence of the relative ion abundances (I%) when selected model ions **3** (■) at  $m/z$  99 from  $\text{Cl}(\text{C}_3\text{H}_8)$  of allyltrimethylsilane, are allowed to react with  $\text{H}_2\text{O}$  at  $1.5 \times 10^{-8}$  mbar. Product ions are formed at  $m/z$  75 (◆).

The reaction of  $\text{C}_5\text{H}_{11}\text{Si}^+$  ions with  $i\text{-C}_3\text{H}_7\text{OH}$  proceeds along two competing pathways leading to  $\text{C}_2\text{H}_7\text{SiO}^+$  (likely corresponding to  $(\text{CH}_3)_2\text{SiOH}^+$ ) and to  $\text{C}_5\text{H}_{13}\text{SiO}^+$  (which may be assigned to  $i\text{-C}_3\text{H}_7\text{OSi}(\text{CH}_3)_2^+$ ) [Eq. (4a-b)]. In the presence of  $i\text{-C}_3\text{H}_7\text{OH}$ ,  $(\text{CH}_3)_2\text{SiOH}^+$  ions react further to give  $(\text{CH}_3)_2\text{Si}(\text{OH})(\text{OH}_2)^+$  and  $i\text{-C}_3\text{H}_7\text{OSi}(\text{CH}_3)_2(\text{OH}_2)^+$  as the plausible products at  $m/z$  93 and  $m/z$  135 from two subsequent reaction steps. An exemplary kinetic run is shown in Fig. 2 illustrating the relative ion abundances for the reaction of model ion **2**, from  $\text{Cl}(\text{C}_3\text{H}_8)$  of (*Z*)-1-(trimethylsilyl)propene, with  $i\text{-C}_3\text{H}_7\text{OH}$ . The kinetic results obtained at different values of the neutral pressure were averaged and are listed in Table 1.

Precursor of reactant ion <sup>a</sup>	ROR'	$k_{\text{exp}}$ <sup>b</sup>	$\Phi$ <sup>c</sup>
(Z)-1-(trimethylsilyl)propene ( <b>2</b> )	H <sub>2</sub> O	2.2 ± 0.8	12 ± 4
(E)-1-(trimethylsilyl)propene ( <b>4</b> )	H <sub>2</sub> O	2.1 ± 1.2	12 ± 6
2-(trimethylsilyl)propene ( <b>6</b> )	H <sub>2</sub> O	2.0 ± 1.3	11 ± 7
Allyltrimethylsilane ( <b>3</b> )	H <sub>2</sub> O	2.3 ± 0.5	13 ± 3
<b>S</b>	H <sub>2</sub> O	2.0 ± 0.6	11 ± 3
(Z)-1-(trimethylsilyl)propene ( <b>2</b> )	<i>i</i> -C <sub>3</sub> H <sub>7</sub> OH	4.5 ± 1.5	29 ± 10
(E)-1-(trimethylsilyl)propene ( <b>4</b> )	<i>i</i> -C <sub>3</sub> H <sub>7</sub> OH	5.3 ± 0.5	34 ± 3
2-(trimethylsilyl)propene ( <b>6</b> )	<i>i</i> -C <sub>3</sub> H <sub>7</sub> OH	6.0 ± 1.5	40 ± 10
Allyltrimethylsilane ( <b>3</b> )	<i>i</i> -C <sub>3</sub> H <sub>7</sub> OH	4.1 ± 0.2	26 ± 2
<b>S</b>	<i>i</i> -C <sub>3</sub> H <sub>7</sub> OH	5.3 ± 1.2	34 ± 4
<b>S</b>	<i>t</i> -C <sub>4</sub> H <sub>9</sub> OCH <sub>3</sub>	7.6 ± 0.8	49 ± 5

<sup>a</sup> Reactant ion designated in parentheses

<sup>b</sup> Second order rate constant in units of 10<sup>-10</sup> cm<sup>3</sup> molecule<sup>-1</sup> s<sup>-1</sup>, at 300 K.

<sup>c</sup> Reaction efficiency =  $k_{\text{exp}}/k_{\text{coll}}$ , expressed as percentage.

**Table 1.** Kinetic data for the gas-phase reaction of C<sub>5</sub>H<sub>11</sub>Si<sup>+</sup> ions with ROR' nucleophiles.

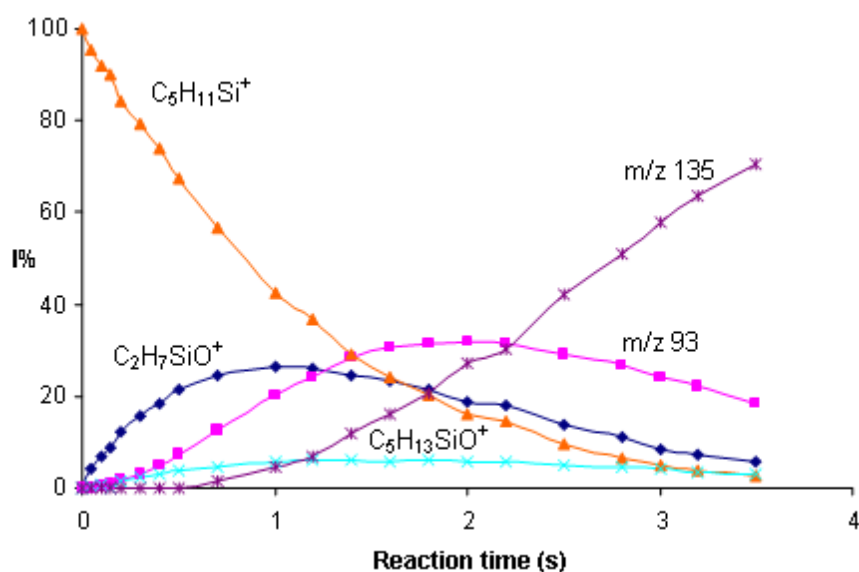


**Fig. 2.** Time dependence of the relative ion abundances (I%) when selected model ions **2** ( $\blacktriangle$ ) at  $m/z$  99 from  $\text{Cl}(\text{C}_3\text{H}_8)$  of (Z)-1-(trimethylsilyl)propene, are allowed to react with *i*-C<sub>3</sub>H<sub>7</sub>OH at  $4.3 \times 10^{-8}$  mbar. Primary product ions are formed at  $m/z$  75 ( $\blacklozenge$ ) and  $m/z$  117 ( $\times$ ). Secondary product ions are at  $m/z$  93 ( $\blacksquare$ ) and  $m/z$  135 ( $\ast$ ).

Precursor of reactant ion <sup>a</sup>	ROR'	P <sub>1</sub> /P <sub>2</sub> <sup>b</sup>
( <i>Z</i> )-1-(trimethylsilyl)propene ( <b>2</b> )	<i>i</i> -C <sub>3</sub> H <sub>7</sub> OH	8.5 ± 1.7 <sup>c</sup>
( <i>E</i> )-1-(trimethylsilyl)propene ( <b>4</b> )	<i>i</i> -C <sub>3</sub> H <sub>7</sub> OH	11 ± 1.8 <sup>c</sup>
2-(trimethylsilyl)propene ( <b>6</b> )	<i>i</i> -C <sub>3</sub> H <sub>7</sub> OH	20 ± 5 <sup>c</sup>
Allyltrimethylsilane ( <b>3</b> )	<i>i</i> -C <sub>3</sub> H <sub>7</sub> OH	4.3 ± 0.5 <sup>c</sup>
<b>S</b>	<i>i</i> -C <sub>3</sub> H <sub>7</sub> OH	21 ± 2 <sup>c</sup>
( <i>Z</i> )-1-(trimethylsilyl)propene ( <b>2</b> )	<i>t</i> -C <sub>4</sub> H <sub>9</sub> OCH <sub>3</sub>	2.6 ± 0.3 <sup>d</sup>
( <i>E</i> )-1-(trimethylsilyl)propene ( <b>4</b> )	<i>t</i> -C <sub>4</sub> H <sub>9</sub> OCH <sub>3</sub>	2.5 ± 0.3 <sup>d</sup>
2-(trimethylsilyl)propene ( <b>6</b> )	<i>t</i> -C <sub>4</sub> H <sub>9</sub> OCH <sub>3</sub>	4.6 ± 0.7 <sup>d</sup>
Allyltrimethylsilane ( <b>3</b> )	<i>t</i> -C <sub>4</sub> H <sub>9</sub> OCH <sub>3</sub>	24 ± 5 <sup>d</sup>
<b>S</b>	<i>t</i> -C <sub>4</sub> H <sub>9</sub> OCH <sub>3</sub>	4.1 ± 0.7 <sup>d</sup>

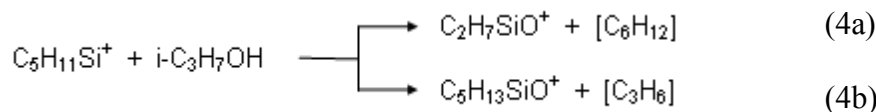
<sup>a</sup> Reactant ion designated in parentheses

<sup>b</sup> Ratio of the yields of product ions P<sub>1</sub> and P<sub>2</sub> obtained from the ion-molecule reactions run at 300 K.

<sup>c</sup> P<sub>1</sub> = C<sub>2</sub>H<sub>7</sub>SiO<sup>+</sup> and P<sub>2</sub> = C<sub>5</sub>H<sub>13</sub>SiO<sup>+</sup>.

<sup>d</sup> P<sub>1</sub> = C<sub>3</sub>H<sub>9</sub>SiO<sup>+</sup> and P<sub>2</sub> = C<sub>6</sub>H<sub>15</sub>SiO<sup>+</sup>.

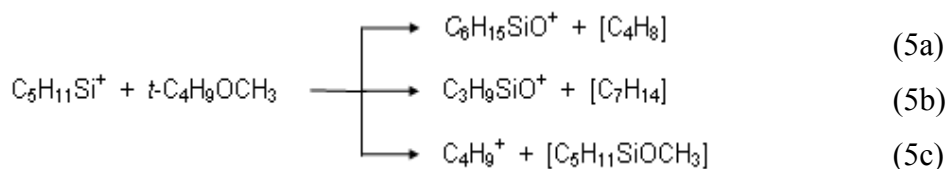
**Table 2.** Product ratios for the gas-phase reaction of C<sub>5</sub>H<sub>11</sub>Si<sup>+</sup> ions with ROR' nucleophiles.



As expected from a nucleophile stronger than water, the reaction efficiencies are higher, their values comprised within 26-40%, and do not lend a useful tool to distinguish among isomeric structures. The branching between the two reaction channels 4a and 4b appears more informative and is extracted by extrapolating the relative ion yields to initial time. The formation of C<sub>2</sub>H<sub>7</sub>SiO<sup>+</sup> is always favored with respect to C<sub>5</sub>H<sub>13</sub>SiO<sup>+</sup> but the branching ratio is different for the various isomers ranging from 4.3 to 21 (Table 2). Thus, while the C<sub>5</sub>H<sub>11</sub>Si<sup>+</sup> ions deriving from (*Z*)- and (*E*)-1-(trimethylsilyl)propene showing ratios of 8.5 and 11, respectively, are not clearly discriminated, the observed value of 21 for the sample ion **S** is quite close to the value for the model ion **6** from Cl(C<sub>3</sub>H<sub>8</sub>) of 2-(trimethylsilyl)propene and is far from the ratio of 4.3 displayed by the model ion **3** from allyltrimethylsilane.

In a further effort to obtain safer support for a structural assignment, the reactivity pattern toward *tert*-butyl methyl ether (*t*-C<sub>4</sub>H<sub>9</sub>OCH<sub>3</sub>) has been examined. When C<sub>5</sub>H<sub>11</sub>Si<sup>+</sup> ions are allowed to react with *t*-C<sub>4</sub>H<sub>9</sub>OCH<sub>3</sub> three primary product ions are observed,

namely  $C_6H_{15}SiO^+$ ,  $C_3H_9SiO^+$ , and  $C_4H_9^+$ , as shown in Eq. (5). The plausible composition of  $C_6H_{15}SiO^+$ ,  $C_3H_9SiO^+$ , and  $C_4H_9^+$  is likely corresponding to  $t-C_4H_9OSi(CH_3)_2^+$ ,  $CH_3OSi(CH_3)_2^+$ , and  $t-C_4H_9^+$ , respectively.



The exemplary plot of Fig. 3 shows the kinetic progress of the reaction of the sample ion **S** from the addition of  $(CH_3)_3Si^+$  to acetylene. As in the case of the nucleophiles  $H_2O$  and  $i-C_3H_7OH$ , the evaluation of the efficiency for the reactions of the model ions does not appear to yield distinct values that could be used for any reliable structural assignment and further efforts to collect these data were not engaged. Given the higher nucleophilicity of  $t-C_4H_9OCH_3$  also the reaction efficiency is higher, on the order of 50 %, and the value for the reaction of **S** is reported in Table 1.

As observed for the reaction with  $i-C_3H_7OH$  as probe nucleophile, it is the branching ratio into the different product channels that is most revealing about structural differences in the model ions. The branching ratio into the  $C_3H_9SiO^+$  and  $C_6H_{15}SiO^+$  product ions is found to be the most informative.

The third product ion,  $C_4H_9^+$ , is however interfering due to a proton transfer reaction to  $t-C_4H_9OCH_3$  which forms a cation ( $C_5H_{13}O^+$ ) formally isobaric with  $C_3H_9SiO^+$ . The high resolving power of the FT-ICR mass spectrometer has permitted to solve the problem by the distinct separation of the two ion signals at  $m/z$  89.0961 ( $C_5H_{13}O^+$ ) and  $m/z$  89.0417 ( $C_3H_9SiO^+$ ). The values of the branching ratios gained by the correct evaluation of the relative abundance of the  $C_3H_9SiO^+$  species is reported in Table 2.

The relative abundances of  $C_3H_9SiO^+$  and  $C_6H_{15}SiO^+$  product ions are fairly constant with respect to reaction time (though only the early part of the kinetic progress of the reaction was considered) and neutral pressure. The data collected in Table 2 indicate that the reactivity behavior of the sampled ion population **S** conforms to the one displayed by the model ion **6** from 2-(trimethylsilyl)propene. The partition into the  $C_2H_7SiO^+$  and  $C_5H_{13}SiO^+$  products of the reaction with  $i-C_3H_7OH$  is  $20 \pm 5$  from the model ion and  $21 \pm 2$  from **S**. The two values are equal within experimental error and so are the corresponding

ratios for the formation of  $C_3H_9SiO^+$  and  $C_6H_{15}SiO^+$  product ions,  $4.6 \pm 0.7$  and  $4.1 \pm 0.7$ , respectively, from the reaction with  $t\text{-}C_4H_9OCH_3$ . The results of the ion-molecule reactions clearly suggest that the  $C_5H_{11}Si^+$  addition product from the  $(CH_3)_3Si^+$  reaction with acetylene should be ascribed the structure of 2-propenyl-dimethylsilyl cation **6** [Eq. (6)].

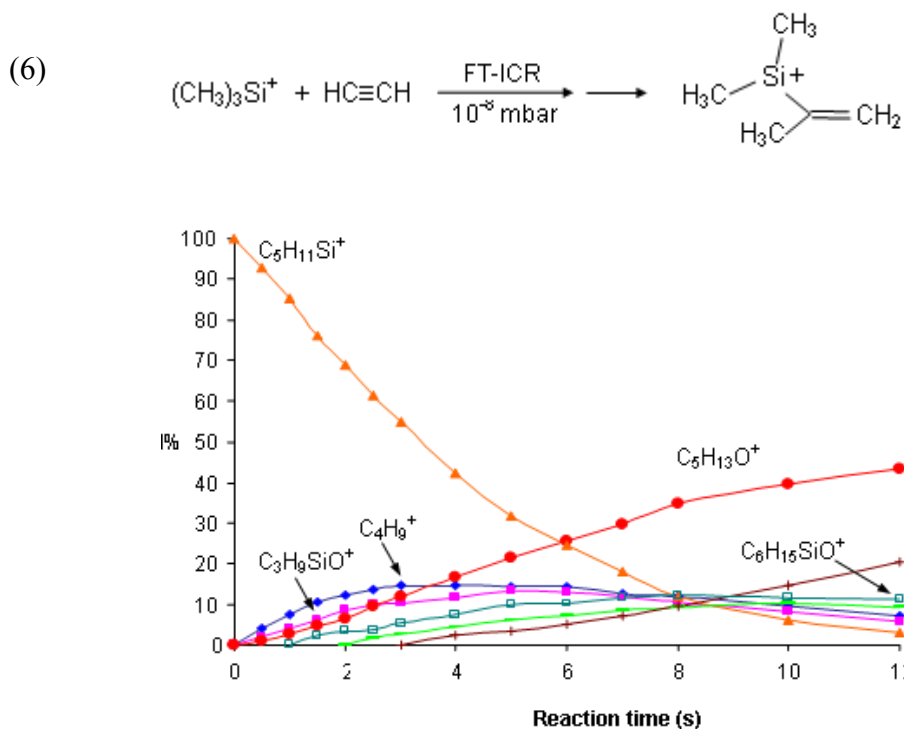


**Fig. 3.** Time dependence of the relative ion abundances (I%) when selected sample ions **S** at  $m/z$  99 from the addition of  $(CH_3)_3Si^+$  to acetylene ( $\blacktriangle$ ) are allowed to react with  $t\text{-}C_4H_9OCH_3$  at  $1.9 \times 10^{-8}$  mbar. Primary product ions are formed at  $m/z$  131 ( $\square$ ) ( $C_6H_{15}SiO^+$ ),  $m/z$  89 ( $\blacksquare$ ) ( $C_3H_9SiO^+$ ), and  $m/z$  57 ( $\blacklozenge$ ) ( $C_4H_9^+$ ). Secondary product ions are at  $m/z$  89 ( $\bullet$ ) ( $C_5H_{13}O^+$ ), and  $m/z$  121 ( $+$ ).

### 1.3.3. $C_5H_{11}Si^+$ Isomers and Rearrangement Pathways: a Quantum Chemical Assay

The rearrangement reaction depicted in Eq. (6) involves a complex pathway that is conceivably initiated after the formation of a nascent  $(CH_3)_3Si^+$ -acetylene complex. This adduct seemingly undergoes at least a 1,2-methyl migration from Si to C and a 1,2-H shift process. The driving force of the reaction lies in the formation of an ion where the positive charge is formally placed on silicon but the involvement of activation barriers is underlined by the reactivity behavior observed at higher pressure (3 mbar to 1 atmosphere), where the isomerization does not take place. In order to elucidate the relative energies of the various ionic intermediates and the energy profile of the plausible paths linking them, ab initio calculations at the CCSD(T)/6-311++G(2d,2p)//B3LYP/6-311G(2d,p) level of

theory were undertaken whose results are summarized. The significant structures that were investigated include the isomers depicted in Chart 1 together with the nascent  $(\text{CH}_3)_3\text{Si}^+$ -acetylene complex **1**, formerly described by the limiting geometries **1A** and **1B**.

Fig. 4 illustrates the optimized geometries of the stable isomers and the transition states for the rearrangement paths obtained by B3LYP/6-311G(2d,p) calculations. Table S1 data summarizes the computational data obtained at both B3LYP/6-311G(2d,p) and CCSD(T)/6-311++G(2d,2p)//B3LYP/6-311G(2d,p) level about all relevant species that have been examined and Table S2 provide the Cartesian coordinates of the optimized structures.

Species	$E^{a,b}$	ZPE <sup>b,c</sup>	$E_{\text{rel}}^{b,c}$	$E^d$	$E_{\text{rel}}^{c,e}$
$(\text{CH}_3)_3\text{Si}^+$ + acetylene	-486.407603 [0]	355.5	183.6	0.000000	186.2
<b>1</b>	-486.437097 [0]	365.4	116.6	-485.401855	95.1
<b>2</b>	-486.480107 [0]	378.2	16.4	-485.437121	15.2
<b>3</b>	-486.464690 [0]	374.0	52.7	-485.424757	43.5
<b>4</b>	-486.485995 [0]	377.2	0	-485.442571	0
<b>5</b>	-486.423707 [0]	363.3	149.6	-485.381418	146.6
<b>6</b>	-486.474615 [0]	376.6	29.3	-485.434603	20.3
<b>TS</b> <sub>12</sub>	-486.407316 [1] (-439.97)	368.9	198.2	-485.366142	192.3
<b>TS</b> <sub>23</sub>	-486.385256 [1] (-959.42)	366.3	253.6	-485.333827	274.6
<b>TS</b> <sub>34</sub>	-486.3552795 [1] (-1735.38)	359.1	325.0	-485.304678	343.9
<b>TS</b> <sub>24</sub>	-486.410429 [1] (-1629.77)	357.1	178.3	-485.362819	198.6
<b>TS</b> <sub>15</sub>	-486.411313 [1] (-526.34)	356.4	175.3	-485.374816	157.1
<b>TS</b> <sub>56</sub>	-486.422118 [1] (-221.1)	366.9	157.3	-485.378983	156.6
<b>TS</b> <sub>46</sub>	-486.393542 [1] (-924.63)	366.1	231.6	-485.352772	224.6

<sup>a</sup> In Hartree particle<sup>-1</sup>, number of imaginary frequencies in square brackets and size of the imaginary frequency in parentheses.

<sup>b</sup> Computations at B3LYP/6-311G(2d,p) level of theory.

<sup>c</sup> In kJ mol<sup>-1</sup>.

<sup>d</sup> In Hartree particle<sup>-1</sup>, computations at CCSD(T)/6-311++G(2d,2p)//B3LYP/6-311G(2d,p) level.

<sup>e</sup> Computations at CCSD(T)/6-311++G(2d,2p)//B3LYP/6-311G(2d,p) level. ZPE contributions are included as obtained at B3LYP/6-311G(2d,p) level.



**Table S1.** Absolute electronic energies, zero point energies (ZPE) and relative energies at 0K of C<sub>5</sub>H<sub>11</sub>Si<sup>+</sup> isomers and of the transition states for their rearrangements. Computations at B3LYP/6-311G(2d,p) level and at CCSD(T)/6-311++G(2d,2p)//B3LYP/6-311G(2d,p) level.

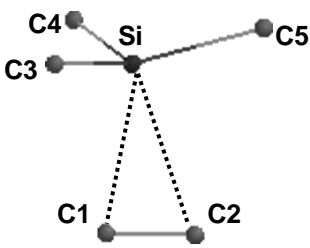
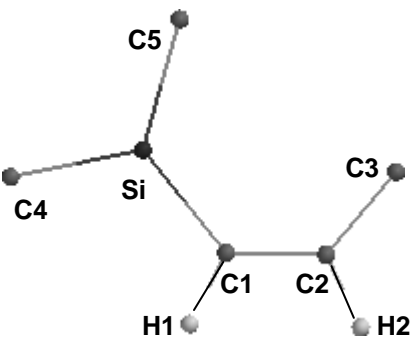
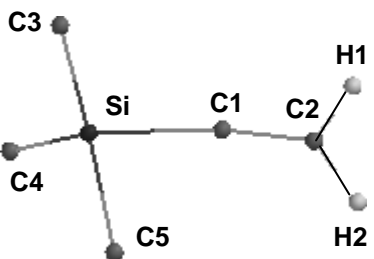
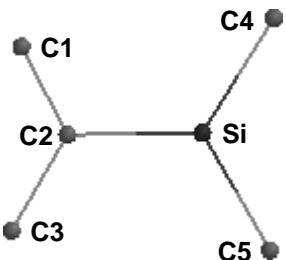
Because silylsubstituted vinyl cations are known to be quite flexible and the obtained structures may be dependent on the chosen method, also MP2 computations have been applied to optimize few significant species and check whether significantly different structures were obtained. To this purpose geometry optimization and frequency analysis at MP2/6-311G(2d,p) level of theory have been performed on species **1,2,5,6**, **TS<sub>12</sub>** and **TS<sub>15</sub>**. The so-obtained thermodynamic data are listed in Table S3. Table S4 presents a comparison of selected geometrical parameters evaluated by the B3LYP and MP2 methods. The MP2 results do not present significant differences with respect to the corresponding structures optimized at B3LYP/6-311G(2d,p) level. In view of the substantial consistency of B3LYP/6-311G(2d,p) and MP2/6-311G(2d,p) computational results, the forthcoming discussion will refer to the final data computed at CCSD(T)/6-311++G(2d,2p)//B3LYP/6-311G(2d,p) level.

Species	E <sup>a</sup>	ZPE <sup>b</sup>	E <sub>rel</sub> <sup>b</sup>
(CH <sub>3</sub> ) <sub>3</sub> Si <sup>+</sup>	-408.156197 [0]	289.6	} 175.6
HCCH	-77.1256165 [0]	69.0	
<b>1</b>	- 485.321039 [0]	369.4	83.4
<b>2</b>	- 485.352087 [0]	383.3	15.9
<b>4</b>	- 485.357709 [0]	382.2	0
<b>5</b>	- 485.287933 [0]	366.7	167.7
<b>6</b>	- 485.350244 [0]	381.7	19.1
<b>TS<sub>12</sub></b>	- 485.284266 [1] (-510)	373.5	184.1
<b>TS<sub>15</sub></b>	- 485.286983 [1] (-616)	362.3	165.8

<sup>a</sup> In Hartree particle<sup>-1</sup>, number of imaginary frequencies in square brackets and size of the imaginary frequency in parentheses.

<sup>b</sup> In kJ mol<sup>-1</sup>.

**Table S3.** Absolute electronic energies, zero point energies (ZPE) and relative energies at 0K of selected  $C_5H_{11}Si^+$  isomers and of the transition states for their rearrangements. Computations at MP2/6-311G(2d,p) level.

B3LYP/6-311G(2d,p)			MP2/6-311G(2d,p)	
r(C1-C2)	1.205		1.220	
r(Si-C1)	2.363		2.338	
r(Si-C2)	2.494		2.423	
$\theta$ (Si-C1-C2)	81.75		79.07	
$\theta$ (Si-C2-C1)	69.68		71.31	
$\theta$ (C3-Si-C4)	117.9		118.33	
$\theta$ (C3-Si-C5)	115.36		115.51	
1				
r(C1-C2)	1.356		1.359	
r(Si-C1)	1.797		1.799	
r(C2-C3)	1.480		1.485	
$\theta$ (Si-C1-C2)	129.80		128.79	
$\theta$ (C1-C2-C3)	129.54		128.85	
$\theta$ (C4-Si-C1)	117.24		117.38	
$\theta$ (H1-C1-C2)	116.65		116.66	
r(C1-C2)	1.274		1.283	
r(Si-C1)	1.877		1.882	
r(C2-H1)	1.095		1.096	
$\theta$ (Si-C1-C2)	170.40		171.25	
$\theta$ (C3-Si-C1)	109.82		109.61	
$\theta$ (C1-C2-H1)	119.16		119.49	
$\theta$ (H1-C2-H2)	117.49		117.38	
5				
r(C1-C2)	1.348		1.354	
r(Si-C4)	1.839		1.834	
r(Si-C2)	1.820		1.814	
$\theta$ (C1-C2-C3)	122.69		122.51	
$\theta$ (C1-C2-Si)	116.46		116.28	
$\theta$ (C2-Si-C4)	122.57		122.76	
$\theta$ (C4-Si-C5)	118.67		119.24	
6				

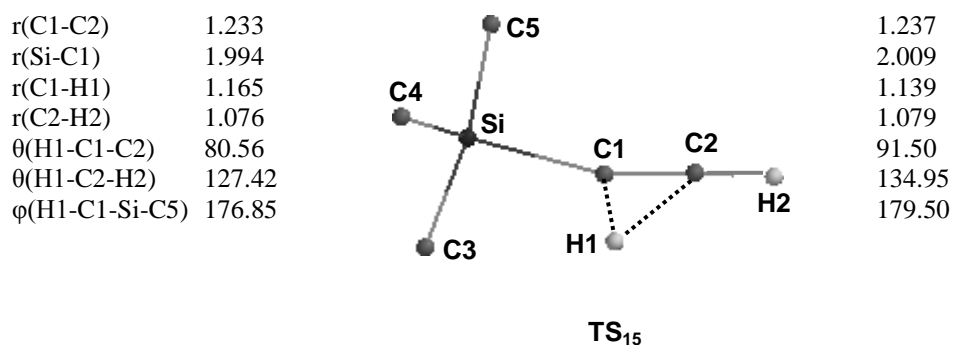
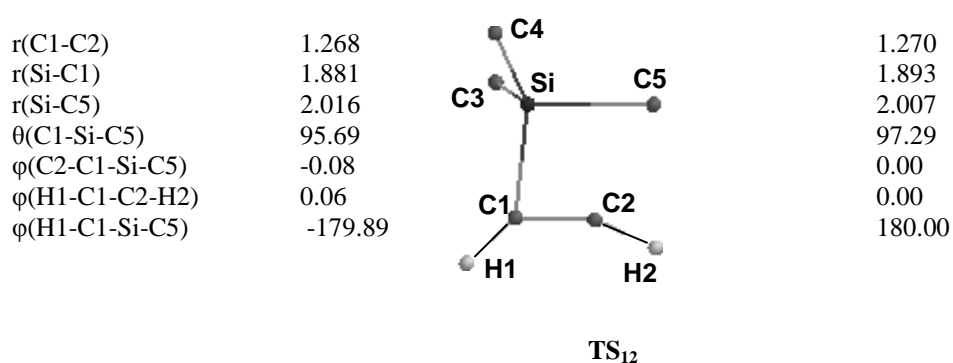


**Table S4.** Selected geometrical parameters (Å, degree) of C<sub>5</sub>H<sub>11</sub>Si<sup>+</sup> species optimized either at B3LYP/6-311G(2d,p) level or at MP2/6-311G(2d,p) level of theory.

As shown by the results collected in Fig. 4, ion **4** is the most stable species among all C<sub>5</sub>H<sub>11</sub>Si<sup>+</sup> ions that were examined, while the (CH<sub>3</sub>)<sub>3</sub>Si<sup>+</sup>-acetylene complex **1**, showing an optimized geometry in between the limiting structures **1A** and **1B**, is 95 kJ mol<sup>-1</sup> higher in energy. Complex **1** is endowed with a highly fluxional structure. In fact, the displacement of the silyl group between the two C-atoms in two equivalent geometries occurs via a C<sub>s</sub> transition state that is about 1 kJ mol<sup>-1</sup> less stable than **1**.

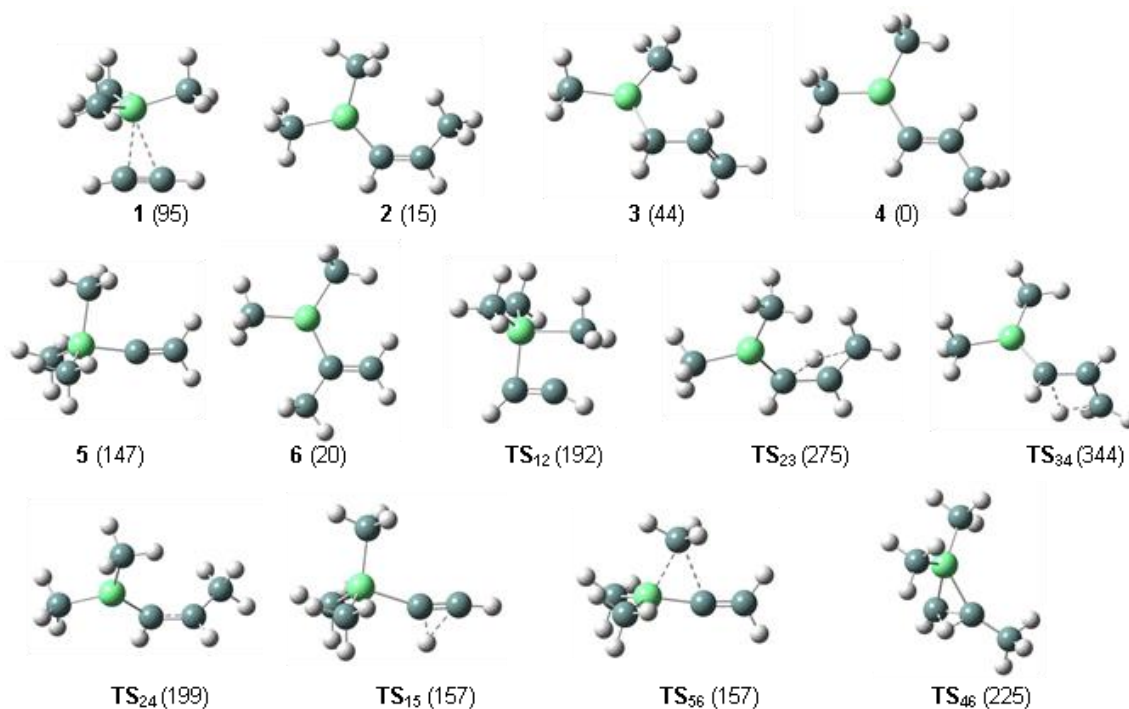
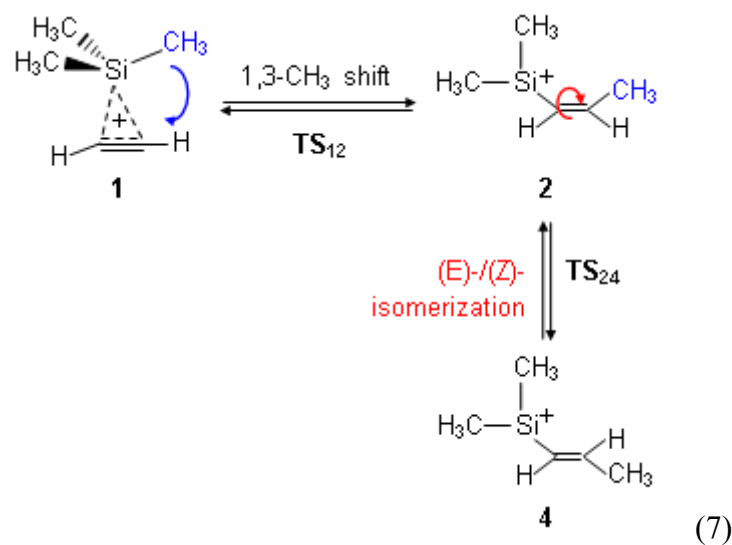
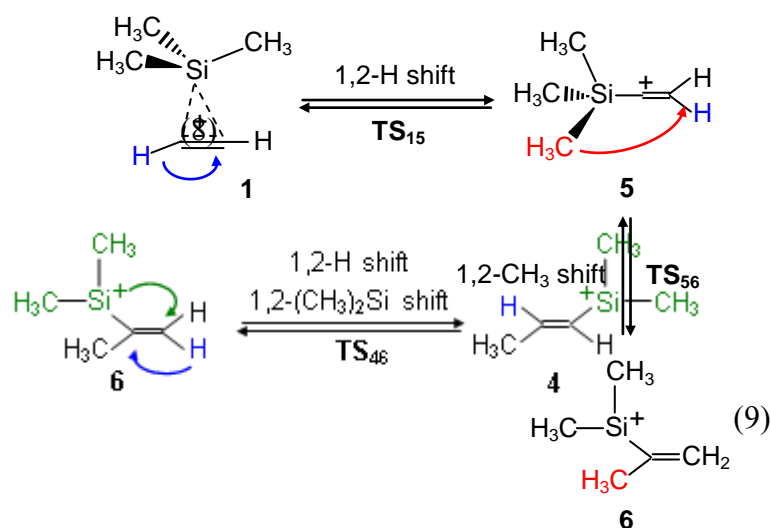


**Fig. 4.** Geometries of  $C_5H_{11}Si^+$  isomers and of the transition states linking them, obtained by B3LYP/6-311G(2d,p) computations. Relative energies are reported in  $\text{kJ mol}^{-1}$ .

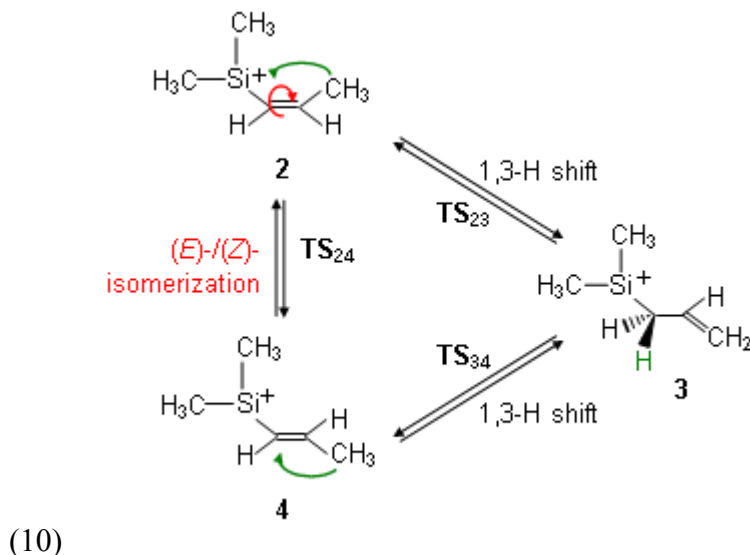
To explore the relevant sections of the potential energy surface whereby the conceivable rearrangements of  $C_5H_{11}Si^+$  ions can take place, several paths have been explored. Eq. (7) shows the rearrangement of **1** to ion **2** involving the migration of a methyl group from silicon to carbon (transition state **TS**<sub>12</sub>). The arrows in Eq. (7) point out the motion of the  $CH_3$  group and the rotation around the double bond. The product ion **2** is the second most stable species but the isomerization to **4**, representing the most stable among the investigated structures, requires a (*Z*)  $\rightarrow$  (*E*) rearrangement (transition state **TS**<sub>24</sub>).



In a similar way, the formation of isomer **6** is depicted in Eq. (8). The process starts from **1** and proceeds by a 1,2-H shift to form an intermediate  $\alpha$ -silyl vinyl cation **5** (transition state **TS<sub>15</sub>**). A 1,2-shift of a methyl group from Si to C leads from **5** to ion **6** holding the positive charge on silicon (transition state **TS<sub>56</sub>**). From ion **6** a rearrangement process can be conceived involving both a 1,2-shift of  $(\text{CH}_3)_2\text{Si}$  and a 1,2-shift of a hydrogen atom to give the most stable isomer **4** (transition state **TS<sub>46</sub>**), as shown in Eq. (9). In this equation, and in the following ones, the arrows point out the migration of an atom or group. Alternatively, a stepwise path for the **6** to **4** rearrangement has been taken into consideration involving an intermediate 2-silacyclopropyl cation which may then undergo electrocyclic ring opening to give **4**. However, the candidate 2-silacyclopropyl intermediate does not represent a local minimum evolving into structure **6** upon geometry optimization.



A pathway may be further envisioned leading to the allyldimethylsilyl cation **3**, whose formation derives from ions **2/4** by a formal 1,3-H shift (transition states **TS<sub>23</sub>** and **TS<sub>34</sub>**, respectively), as shown in Eq. (10).



The energy profile of the various paths that were envisioned is illustrated in Fig. 5, showing the relative energies of the significant species evaluated at CCSD(T)/6-311++G(2d,2p)//B3LYP/6-311G(2d,p) level of theory. Throughout the diagram a broken line marks the energy content of the separated  $(\text{CH}_3)_3\text{Si}^+$ -acetylene molecules combining to form complex **1** that is stabilized by  $91 \text{ kJ mol}^{-1}$  relative to the free reagents. The reaction exothermicity, however, remains stored in the adduct ion **1** unless dissipated by radiative emission or energy transfer by unreactive collisions with a bath gas. Both processes are inefficient for a relatively small species in a highly dilute environment<sup>58,59</sup> so that the energy released in the addition process contributes to form a ‘hot’ species that can undergo rearrangement processes involving substantial activation barriers [Eq. (2)]. The plot shows that the transition state lying lowest in energy, **TS<sub>15</sub>**, allows the conversion of **1** to **5**. Ion **5** is probably a fleeting intermediate because it can proceed without any appreciable activation barrier to form **6**. Ion **6** is likely to represent a dead end product under the prevailing experimental conditions.

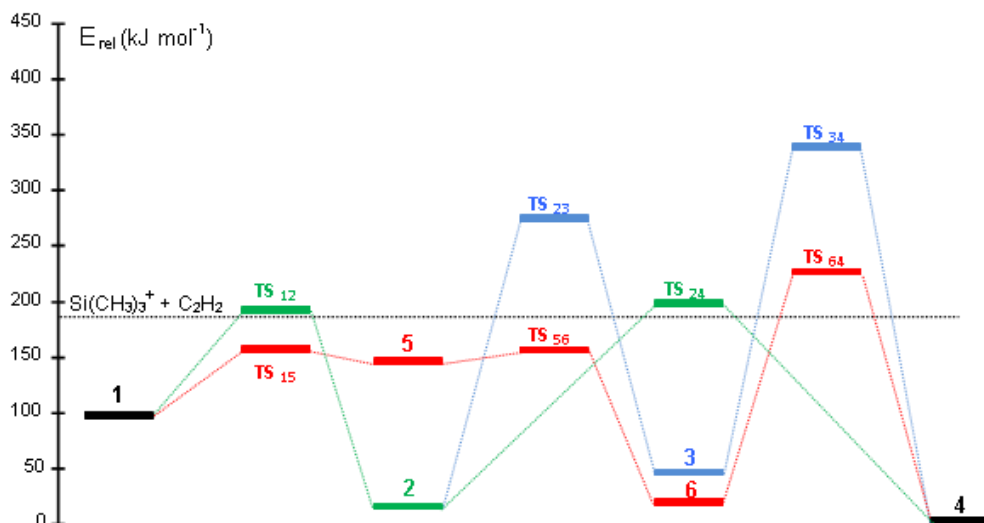


**Fig. 5.** Energy profiles of the proposed pathways following the  $(\text{CH}_3)_3\text{Si}^+$  addition to acetylene evaluated at CCSD(T)/6-311++G(2d,2p)//B3LYP/6-311G(2d,p) level of theory. Values of  $E_{\text{rel}}$  at 0K are given in  $\text{kJ mol}^{-1}$ .

A further rearrangement to the most stable species **4** requires passing an activation barrier that protrudes above the energy content of the reactant pair so that the corresponding transition state **TS<sub>46</sub>** is hardly accessible. The **TS<sub>46</sub>** transition state combines a 1,2-H shift with a 1,2- $(\text{CH}_3)_2\text{Si}$  shift involving the same two C-atoms, though in opposite direction [Eq. (9)]. The reaction path allowing the conversion of **1** into **2** could also be accessed because the corresponding transition state, **TS<sub>12</sub>**, lies only slightly higher in energy (by ca.  $6 \text{ kJ mol}^{-1}$ ) than the separated  $(\text{CH}_3)_3\text{Si}^+$ -acetylene couple. It could provide a route to isomer **4**, if a  $(Z) \rightarrow (E)$  isomerization were further allowed. However, not only is the latter process inhibited by a transition state placed above the reference level, but also the formation of **2** in any significant amount is rather disproven by the gathered experimental evidence. The lack of any evidence suggesting the presence of the allyl-substituted silyl cation **3** is amply justified by the high energy barrier associated to the 1,3-H shift linking **3** to the  $(E)/(Z)$  isomers **2** and **4** by way of **TS<sub>23</sub>** and **TS<sub>34</sub>**. The high barriers computed for the 1,3-H shifts are indeed what is expected for this rearrangement in allylic systems on the basis of FMO theory. It may further be noted that the reference species **2,3,4,6** do indeed retain the original structure from each individual precursor because of the high activation barriers for their interconversion, as testified by the computed energy profiles.

## 1.4. Conclusions

The neat process of  $(\text{CH}_3)_3\text{Si}^+$  addition to acetylene can only be examined in the gas-phase where the  $\text{Cl}(\text{CH}_4)$  of  $(\text{CH}_3)_4\text{Si}$  provides an entry to naked  $(\text{CH}_3)_3\text{Si}^+$  ions in a dilute environment lacking potential nucleophiles that tend to trap this highly electrophilic species, masking its intrinsic reactivity. Though seemingly simple, the  $(\text{CH}_3)_3\text{Si}^+$  addition to acetylene is a complex process when examined at low pressure in the  $10^{-8}$  -  $10^{-7}$  mbar range of FT-ICR mass spectrometry. The formation of formal adduct ions,  $\text{C}_5\text{H}_{11}\text{Si}^+$ , reveals the occurrence of a rearrangement process allowed by the excess internal energy released in the primary addition of  $(\text{CH}_3)_3\text{Si}^+$  to acetylene. The structure of  $\text{C}_5\text{H}_{11}\text{Si}^+$  ions has been probed by ion-molecule reactions, taking advantage of the temporal resolution allowing kinetic determinations and also of the mass resolution which permitted to discriminate formally isobaric product ions. When confronted with the reactivity pattern of model ions, the sampled  $\text{C}_5\text{H}_{11}\text{Si}^+$  adducts, ions **S**, are found to behave in a quite similar way as the 2-propenyl-dimethylsilyl cation **6**. Additionally, the partition in competing paths following the reaction with selected neutrals (*i*- $\text{C}_3\text{H}_7\text{OH}$  and *t*- $\text{C}_4\text{H}_9\text{OCH}_3$ ) is different when other stable isomers (**2,3,4**) are tested. The structural assignment of the observed  $\text{C}_5\text{H}_{11}\text{Si}^+$  adducts, allowed by the distinct ion-molecule reactivity, is further supported by the quantum chemical calculations of the potential isomers and the related energy profiles for their interconversion pathways. The computational results confirm the experimental findings. The nascent  $(\text{CH}_3)_3\text{Si}^+$ -acetylene complex **1** may rearrange to isomer **6** passing the lowest activation energy barrier associated to a 1,2-H shift from  $\text{C}_\alpha$  to  $\text{C}_\beta$  of the former acetylene unit. The so-formed  $\alpha$ -silyl vinyl cation **5** is a transient intermediate that can proceed to **6** in a nearly barrierless process involving a Si to C methyl migration and forming a stable species with a positive charge centered on silicon. Further rearrangements to other isomers including the most stable one, **4**, is inhibited by activation energy barriers protruding above the energy level of the reactant pair. An alternative path energetically accessible, namely **1**  $\rightarrow$  **2**, is associated to an activation energy barrier of ca.  $97 \text{ kJ mol}^{-1}$ . This rearrangement does not appear to take place, though, suggesting that the differential energy barrier of ca.  $35 \text{ kJ mol}^{-1}$  relative to **1**  $\rightarrow$  **6** is effective in rendering the reaction selective. At the same time, the **1**  $\rightarrow$  **6** rearrangement is hampered by the collisional relaxation occurring at 3-5 mbar in HPMS where adventitious water is a final



trap for  $(\text{CH}_3)_3\text{Si}^+$  ions whereas **1** is efficiently stabilized at atmospheric pressure where it ultimately undergoes deprotonation to the neutral substitution product,  $(\text{CH}_3)_3\text{SiC}\equiv\text{CH}$ . In conclusion, the integrated approach combining bimolecular ion-chemistry with quantum chemical calculations has provided a consistent view of the reactivity going on in  $(\text{CH}_3)_3\text{Si}^+$ -acetylene adducts in gaseous environments at widely different pressures. In this context, it is interesting to compare the behavior of the gaseous  $(\text{CH}_3)_3\text{Si}^+$ -acetylene complex with a related system that has been recently investigated using matrix isolation IR spectroscopy and quantum chemical calculation<sup>71</sup>. Trimethylsilylacetylenes ( $(\text{CH}_3)_3\text{SiC}\equiv\text{CR}$ , R = H, CH<sub>3</sub>, Si(CH<sub>3</sub>)<sub>3</sub>) have been codeposited with SbF<sub>5</sub> and submitted to vibrational analysis after deposition and upon warming of the matrix. New bands appearing in the 1600 cm<sup>-1</sup> spectral region have been assigned to silaallylcations such as **2** and **6** suggested to arise by protonation and ensuing isomerization processes. Vibrational spectroscopy of the gaseous sample ion **S** using IR multiple photon dissociation spectroscopy<sup>72-73</sup> is a forthcoming effort to settle the significant features of the potential energy surface of gaseous C<sub>5</sub>H<sub>11</sub>Si<sup>+</sup> ions.

## 1.5. References

- (1) Lickiss, P.D. Silicenium ions: experimental aspects, in: Z. Rappoport, Y. Apeloig (Eds.), *The Chemistry of Organic Silicon Compounds Wiley*, Chichester, **1998**, vol. 2, pp. 557-594.
- (2) Reed, C. A. The silylium ion problem,  $R_3Si^+$ . *Bridging Organic and Inorganic Chemistry, Acc. Chem. Res.* **1998**, 31, 325-332.
- (3) Olah, G. A.; Rasul, G.; Li, X.; Buchholz, H. A.; Sandford, G.; Prakash, G. K. S. Triethylsilyl Cations *Science* **1994**, 263, 983-984.
- (4) Arshadi, M., Johnels, D., Edlund, U., Ottosson, C.-H., Cremer, D. Solvated Silylium Cations: Structure Determination by NMR Spectroscopy and the NMR/Ab Initio/IGLO Method *J. Am. Chem. Soc.* **1998**, 118, 5120-5131.
- (5) Lambert, J. B., Zhao, Y., Wu, H., Tse, W. C., Kuhlmann, B. The Allyl Leaving Group Approach to Tricoordinate Silyl, Germyl, and Stannyl Cations *J. Am. Chem. Soc.* **1999**, 121, 5001-5008.
- (6) Lambert, J. B., Lin, L. The Tridurylsilylium and Tridurylstannylium Cations: Free and not so Free *J. Org. Chem.* **2001**, 66, 8537-8539.
- (7) Kim, K.-C., Reed, C. A., Elliott, D. W., Müller, L. J., Tham, F., Lin, L., Lambert, J. B. Crystallographic Evidence for a Free Silylium ion *Science*, **2002**, 297, 825-827.
- (8) Sekiguchi, A., Matsuno, T., Ichinohe, M. The Homocyclotrisilylium Ion: a Free Silyl Cation in the Condensed Phase *J. Am. Chem. Soc.* **2000**, 122, 11250-11251.
- (9) Karni, M., Apeloig, Y., Kapp, J., Schleyer, P. v. R. Theoretical aspects of compounds containing Si, Ge, Sn and Pb, in: Z. Rappoport, Y. Apeloig, (Eds.), *The Chemistry of Organic Silicon Compounds Wiley*, Chichester, **2001**, 3, 1-163.
- (10) Müller, T., Bauch, C., Ostermeier, M., Bolte, M., Auner N. Norbornyl cations of group 14 Elements *J. Am. Chem. Soc.* **2003**, 125, 2158-2168.
- (11) Duttwyler, S., Do, Q.-Q., Linden, A., Baldrige, K. K., Siegel, J. S. Synthesis of 2,6-Diarylphenyldimethylsilyl Cations: Polar- $\pi$  Distribution of Cation Character *Angew. Chem. Int. Ed.* **2008**, 47, 1719-1722.
- (12) Schulz, A., Villinger, A. Tamed Silylium Ions: Versatile in Catalysis *Angew. Chem. Int. Ed.* **2012**, 51, 4526-4528.
- (13) Reed, C. A.  $H^+$ ,  $CH_3^+$  and  $R_3Si^+$  Carborane Reagents: when Triflates Fail *Acc. Chem. Res.* **2010**, 43, 121-128.
- (14) Reed, C. A., Kim, K.-C., Stoyanov, E. S., Stasko, D., Tham, F. S., Müller, L. J., Boyd P. D. W. Isolating Benzenium Ion Salts *J. Am. Chem. Soc.* **2003**, 125, 1796-1804.
- (15) Lambert, J. B., Zhang, S., Stern, C. L., Huffman, J. C. Crystal Structure of a Silyl Cation with no Coordination to Anion and Distant Coordination to Solvent *Science* **1993**, 260, 1917-1918.
- (16) Schwarz, H. Positive and Negative Ion Chemistry of Silicon-Containing Molecules in the Gas-Phase, in: S. Patai, Z. Rappoport (Eds.) *The Chemistry of Organic Silicon Compounds Wiley* **1989**, 445-510.
- (17) Goldberg, N., Schwarz, H. Gas-phase Ion Chemistry of Silicon-Containing Molecules, in: Z. Rappoport, Y. Apeloig (Eds.), *The Chemistry of Organic Silicon Compounds Wiley* **1998**, 2, 1105-1142.
- (18) S. Fornarini, Direct Aromatic Substitution by Trimethylsilyl Cations *J. Org. Chem.* **1988**, 53, 1314-1316.
- (19) Fornarini, S. Mechanistic Views on Aromatic Substitution Reactions by Gaseous Cations *Mass Spectrom. Rev.* **1996**, 15, 365-389.
- (20) Fornarini, S., Crestoni, M. E. Gaseous Arenium Ions at Atmospheric Pressure: Elementary Reactions and Internal Solvation Effects *Acc. Chem. Res.* **1998**, 31, 827-834.
- (21) Fornarini, S. Ion-Molecule Reactions of Silicon Cations, in: Z. Rappoport, Y. Apeloig (Eds.), *The Chemistry of Organic Silicon Compounds Wiley*, Chichester, **2001**, 3, 1027-1057.
- (22) Cacace, F., Crestoni, M. E., Fornarini, S., Gabrielli, R. Cationic Aromatic Silylation in the Gas-Phase *Int. J. Mass Spectrom. Ion Processes* **1988**, 84, 17-32.
- (23) Olah, G. A., Bach, T., Prakash, G. K. S. Aromatic substitution. 56. Observation of Aluminum Trichloride-Catalyzed Trialkylsilylation of Benzene and Toluene with Chlorotrialkylsilanes in the Presence of Huenig Bases *J. Org. Chem.* **1989**, 54, 3770-3771.
- (24) Crestoni, M. E., Fornarini, S. Long-lived *ipso*-Silylated *p*-Toluenium Ions: Evidence From a Kinetic Isotope Effect *Angew. Chem. Int. Ed. Engl.* **1994**, 33, 1094-1096.

- (25) Cacace, F., Attinà, M., Fornarini, S.  $[R_3Si^+arene]^+$   $\sigma$ -Complexes in the Gas-Phase *Angew. Chem. Int. Ed. Engl.* **1995**, 34, 654-655.
- (26) Crestoni, M. E., Fornarini, S., Speranza, M. Gas-phase Heteroaromatic Substitution. 9. Silylation of Simple Five-Membered Heteroaromatic Rings by Trimethylsilyl Cations *J. Am. Chem. Soc.* **1990**, 112, 6929-6935.
- (27) Crestoni, M. E. The Gas-Phase Reactivity of *p*-Me<sub>3</sub>Si-Substituted 1,3-Diphenylpropane Towards Charged Electrophiles: Intra- and Interannular Hydrogen Migrations *Chem. Eur. J.* **1998**, 4, 993-999.
- (28) Chiavarino, B., Crestoni, M. E., Fornarini, S. Aromatic Silylation of Trimethylgermylbenzene by Gaseous Me<sub>3</sub>Si<sup>+</sup> Ions via Me<sub>3</sub>Ge<sup>+</sup> Displacement *Organometallics* **1995**, 14, 2624.
- (29) Cacace, F. Radiolytic Approach to Gas-Phase Ion Chemistry *Acc. Chem. Res.* **1988**, 21, 215-222.
- (30) Kochina, T.A., Vrazhnov, D.V., Ignatyev, I.S., Sinotova, E. N., Voronkov, M. G. Nucleogenic Silylium Cations and their Analogs *J. Organomet. Chem.* **2011**, 696, 1331-1340.
- (31) Kochina, T.A., Shchukin, E.V., Nefedov, V.D., Sinotonova, E.N., Ignatyev, I.S. Radiochemical Study of Ion-Molecule Reactions of Free Ethylsilylenium Ions with Benzene in the Gas-Phase *Radiochemistry* (Engl. Transl.) **2000**, 42, 184-187.
- (32) Kochina, T.A., Vrazhnov, D.V., Ignatyev, I.S., Nefedov, V.D., Sinotova, E.N. Ion-Molecule Reactions of Free Diethylsilylenium Ions with Benzene in the Gas and Liquid Phases *Russ. J. Gen. Chem.* (Engl. Transl.) **1999**, 69, 905-909.
- (33) Shchukin, E.V., Kochina, T.A., Sinotova, E.N., Ignatyev, I.S. Ion-molecule Reactions of Free Diethylsilylenium Ions with Benzene in the Gas and Liquid phases *Russ. J. Gen. Chem.* (Engl. Transl.) **1999**, 69, 905-909.
- (34) Chiavarino, B., Crestoni, M. E., Fornarini, S. Radiolytic Silylation of Alkenes and Alkynes by Gaseous R<sub>3</sub>Si<sup>+</sup> Ions. Stereochemical evidence for the  $\beta$ -silyl effect *J. Am. Chem. Soc.* **1998**, 120, 1523-1527.
- (35) Zhang, W., Stone, J. A., Brook, M. A., McGibbon, G. A. Stabilization of Vinyl Cations by  $\beta$ -silicon: a Quantitative Mass Spectrometric Study *J. Am. Chem. Soc.* **1996**, 118, 5764-5771.
- (36) Chiavarino, B., Crestoni, M. E., Fornarini, S. The Trimethylsilylation of Acetylene *Chem. Comm.* **2002**, 1418-1419.
- (37) Su, T.; Chesnavich, W. J. Parametrization of the Ion-Polar Molecule Collision Rate Constant by Trajectory Calculations *J. Chem. Phys.* **1982**, 76, 5183-5186.
- (38) Siehl, H.-U.; Müller, B.; Fuss, M.; Tsuji, Y. NMR Spectroscopic Investigation of the  $\beta$ -Silyl Effect in Carbocations, in: N. Auner, J. Weis (Eds.), *Organosilicon Chemistry II: from Molecules to Materials Wiley VCH, Weinheim*, **1996**, pp. 361-366.
- (39) Siehl, H.-U.; Müller, T. Silyl-substituted carbocations, in: Rappoport, Z., Apeloig, Y. (Eds.), *The Chemistry of Organic Silicon Compounds Wiley* **1998**, 2, 595-701.
- (40) Siehl, H.-U. Experimental and computational nmr spectroscopic investigation of silyl-substituted carbocations, in: K. Laali (Ed.), *Recent Developments in Carbocation and Onium Ion Chemistry ACS Symposium Series*, Washington, DC, **2007**, 965, 1-31.
- (41) Mo, O.; Yanez, M.; Gal, J.-F.; Maria, P. C.; Guillemin, J.-C. Vinyl- and Ethynylsilanes, -Germanes and -Stannanes. A New Case of Dissociative Proton Attachment *J. Phys. Org. Chem.* **2002**, 15, 509-513.
- (42) Siehl, H.-U.; Kaufmann, F.-P.; Apeloig, Y.; Braude, V.; Danovich, D.; Berndt, A.; Stamatis, N. The First Persistent  $\beta$ -silyl-Substituted Vinyl Cation *Angew. Chem. Int. Ed. Engl.* **1991**, 30, 1479-1482.
- (43) Siehl, H.-U.; Kaufmann, F.-P.; Hori, K. NMR Spectroscopic and Computational Characterization of 1-(*p*-anisyl)Vinyl Cations. Methoxy Group Rotation as a Probe of  $\beta$ -carbon-silicon,  $\beta$ -carbon-carbon and  $\beta$ -carbon-hydrogen hyperconjugation *J. Am. Chem. Soc.* **1992**, 114, 9343-9349.
- (44) Siehl, H.-U.; Kaufmann, F.-P. Carbon-13 NMR Spectroscopic Determination of the Magnitude of the  $\beta$ -silyl Stabilization Effect in 1-Mesitylvinyl Cations *J. Am. Chem. Soc.* **1992**, 114, 4937-4939.
- (45) Siehl, H.-U. NMR Spectroscopic Characterization, in: Z. Rappoport, P. Stang, (Eds.), *Dicoordinated Carbocations Wiley*, New York, **1997**, pp. 189-236.
- (46) Siehl, H.-U. Excursions into long-lived vinyl cations: NMR Spectroscopic Characterization  $\alpha$ -Aryl Vinyl Cations, in: G.K.S. Prakash, P. v. R. Schleyer, (Eds.), *Stable Carbocation Chemistry Wiley*, New York, **1997**, pp. 165-196.

- (47) Müller, T.; Lennartz, R.; Siehl, H.-U. Unusually Stable Vinyl Cations, *Angew. Chem. Int. Ed. Engl.* **2000**, 39, 3074-3077.
- (48) Müller, T.; Margraf, D.; Syha, Y.  $\sigma$ -Delocalization Versus  $\pi$ -Resonance in  $\alpha$ -Aryl-Substituted Vinyl Cations *J. Am. Chem. Soc.* **2005**, 127, 10852-10860.
- (49) Klaer, A.; Syha, Y.; Nasiri, H. R.; Müller, T. Trisilyl-substituted Vinyl Cations *Chem. Eur. J.* **2009**, 15, 8414-8423.
- (50) Müller, T.; Juhasz, M.; Reed, C. A. The X-ray Structure of a Vinyl Cation *Angew. Chem. Int. Ed. Engl.* **2004**, 43, 1543-1546.
- (51) Drewello, T.; Burgers, P. C.; Zummack, W.; Apeloig, Y.; Schwarz, H. Experimental Evidence for Novel Hydrogen/Methyl Exchange Processes Preceding the Unimolecular Dissociation of Silicon-Containing Cations in the Gas-Phase *Organometallics* **1990**, 9, 1161-1165.
- (52) Li, X.; Stone, J. A. Determination of the  $\beta$ -Silicon Effect From a Mass Spectrometric Study of the Association of Trimethylsilylium with Alkenes *J. Am. Chem. Soc.* **1989**, 111, 5586-5592.
- (53) Hajdasz, D.; Squires, R. Structure and Thermochemistry of  $\beta$ -Silicon Carbenium Ions in the Gas-Phase *Chem. Comm.* **1988**, 1212-1214.
- (54) Apeloig, Y.; Karni, M.; Stanger, A.; Schwarz, H.; Drewello, T.; Czekay, G. Rearrangement vs. Dissociation of Gaseous Silicon-Containing Cations: a Combined Experimental-Theoretical Approach *Chem. Comm.* **1987**, 989-991.
- (55) Ketvirtis, A. E.; Bohme, D. K.; Hopkinson, A. C. Organosilicon Cations: Potential Energy Surfaces for  $\text{SiC}_2\text{H}_n^+$  ( $n = 1, 3, \text{ and } 5$ ) *J. Phys. Chem.* **1994**, 98, 13225-13232.
- (56) McGibbon, G. A.; Brook, M. A.; Terlouw, J. K. Stabilization Energies for  $\alpha$ - and  $\beta$ -Silyl Substituents on Vinyl Cations Determined Using Mass Spectrometric Techniques *Chem. Comm.* **1992**, 360-362.
- (57) Bakhtiar, R.; Holznagel, C. M.; Jacobson, D. B. Rearrangement of Nascent  $\alpha$ -Silyl-Substituted Carbenium Ions in the Gas-Phase. 1,2-Hydrogen versus 1,2-methyl versus 1,2-phenyl migration *J. Am. Chem. Soc.* **1992**, 114, 3227-3235.
- (58) Klippenstein, S. J.; Yang, Y.-C.; Ryzhov, V.; Dunbar, R. C. Theory and Modeling of Ion-Molecule Radiative Association Kinetics *J. Chem. Phys.* **1996**, 104, 4502-4516.
- (59) Dunbar, R. C. Modeling radiative Association Kinetics *Int. J. Mass Spectrom. Ion Processes* **1997**, 160, 1-16.
- (60) Orlando, R.; Ridge, D. P.; Munson, B. Radiative Stabilization of Trimethylsilyl Adduct Ions *J. Am. Soc. Mass Spectrom.* **1990**, 1, 144-148.
- (61) Hudrlik, P. F.; Kulkarni, A. K.; Jain, S.; Hudrlik A. M. Stereochemistry of the Wurtz-Fittig preparation of vinylsilanes *Tetrahedron* **1983**, 39, 877-882.
- (62) Meot-Ner, M. Temperature and pressure effects in the Kinetics of Ion-Molecule Reactions, in: M. T. Bowers (Ed.), Gas-Phase Ion Chemistry *Academic Press*, New York, **1979**, vol. 1, pp. 197-271.
- (63) Bartmess, J. E.; Georgiadis R. M. Empirical methods for determination of ionization gauge relative sensitivities for different gases *Vacuum* **1983**, 33, 149-153.
- (64) Gaussian 09, Revision A.1, M. J. Frisch et al, Gaussian, Inc., Wallingford CT, **2009**.
- (65) Peng, C., Schlegel, H. B. Combining Synchronous Transit and quasi-Newton Methods to Find Transition States *Israel J. Chem.* **1993**, 33, 449-454.
- (66) Peng, C.; Ayala, P. Y.; Schlegel, H. B.; Frisch, M. J. Using Redundant Internal Coordinates to Optimize Equilibrium Geometries and Transition States *J. Comp. Chem.* **1996**, 17, 49-56.
- (67) Wojtyniak, A. C. M.; Li, X.; Stone, J. A. The Formation of  $(\text{CH}_3)_7\text{Si}_2^+$  in  $(\text{CH}_3)_4\text{Si}/\text{CH}_4$  Mixtures and  $\text{CH}_3^-$  Exchange Reactions Between  $(\text{CH}_3)_4\text{Si}$ ,  $(\text{CH}_3)_4\text{Ge}$ , and  $(\text{CH}_3)_4\text{Sn}$  Studied by High Pressure Mass Spectrometry *Can. J. Chem.* **1987**, 65, 2849-2854.
- (68) Nedev, H.; Denhez, J. P.; Leblanc, D.; Audier, H. E. Silicon- Versus Carbon-Containing Ions: 1,3- $\text{CH}_3^+$  Transfers *Int. J. Mass Spectrom.* **2002**, 217, 245-255.
- (69) Bakhtiar, R.; Holznagel, C. M.; Jacobson, D. B. Dyotropic Rearrangement of Organosilylenium Ions in the Gas-Phase *Organometallics* **1993**, 12, 880-887.
- (70) Stone, J. A. Gas-Phase Association Reactions of Trimethylsilylium  $((\text{CH}_3)_3\text{Si}^+)$  with Organic Bases *Mass Spectrom. Rev.* **1997**, 16, 25-49.
- (71) Cical, H.; Vancik, H.; Mihalic, Z. Reaction of Trimethylsilylacetylenes with Antimony Pentafluoride Under Matrix Isolation Conditions: Experimental and Computational Study *J. Org. Chem.* **2010**, 75, 6969-6972.
- (72) Chiavarino, B.; Crestoni, M. E.; Fornarini, S.; Lemaire, J.; Mac Aleese, L.; Maitre, P. Infrared Spectroscopy of Protonated Phenylsilane in the Gas-Phase *ChemPhysChem* **2005**, 6, 437-440.

(73) Chiavarino, B.; Crestoni, M. E.; Dopfer, O.; Maitre, P.; Fornarini, S. Benzylum Versus Tropylium Ion Dichotomy: Vibrational Spectroscopy of Gaseous  $C_8H_9^+$  Ions *Angew. Chem. Int. Ed.* **2012**, *51*, 4947-4949.



## CHAPTER 2

# **Vibrational signatures of the naked aqua complexes from platinum(II) anticancer drugs**

**DOI: [10.1021/jz401959s](https://doi.org/10.1021/jz401959s)**

## 2.1. Introduction

The great potential of *cis*-diamminedichloroplatinum(II) (cisplatin®) as an antitumor agent was first recognized by Rosenberg et al. in 1969<sup>1</sup>. Nowadays, platinum-based anticancer drugs are widely used in chemotherapy. cisplatin is known to undergo spontaneous hydrolysis in aqueous solution by nucleophilic substitution of chloride with water<sup>2,3</sup>. The process is linked to the anticancer activity of cisplatin because it is the initial step leading to reactive metabolites that ultimately give rise to DNA adducts<sup>4-6</sup>. The most important hydrolysis product is the *cis*-[PtCl(NH<sub>3</sub>)<sub>2</sub>(H<sub>2</sub>O)]<sup>+</sup> cation, characterized by a pK<sub>a</sub> value of 6.5<sup>2</sup>. This cationic species is highly reactive because water can be substituted easily by donor ligands and this mono-aqua complex is believed to react with one of the nitrogen-containing bases of DNA with the loss of water. Numerous experimental and theoretical investigations have analyzed the hydrolysis of cisplatin<sup>7</sup> and the intermediates that are formed from cisplatin by replacement of chloro ligands by water or hydroxyl groups<sup>2,8-10</sup>. However, the key *cis*-[PtCl(NH<sub>3</sub>)<sub>2</sub>(H<sub>2</sub>O)]<sup>+</sup> complex that is primarily formed has not yet been characterized by vibrational spectroscopy, one of the most fundamental tools for molecular structure elucidation. The aim of this work is to provide experimental vibrational spectroscopic data about *cis*-[PtCl(NH<sub>3</sub>)<sub>2</sub>(H<sub>2</sub>O)]<sup>+</sup> and *trans*-[PtCl(NH<sub>3</sub>)<sub>2</sub>(H<sub>2</sub>O)]<sup>+</sup>.

## 2.2. Results and Discussion

The direct characterization of these ions in solution faces problems due to proton-transfer equilibria, further hydrolysis, and formation of hydroxo-bridged oligomers.<sup>2</sup> However, when these species are allowed to form in solution and are then transferred to the gas-phase, they can be isolated and sampled without any interference by further reactive steps and aggregation phenomena. Furthermore, no solvent nor matrix is present that may somehow alter the intrinsic properties of the naked species. Using tunable IR lasers coupled with tandem mass spectrometry, reactive intermediates, either positively or negatively charged, have been characterized, relying on their IR multiple photon dissociation (IRMPD) spectra<sup>11-16</sup>. In the present study, the IR features of *cis*- and *trans*-[PtCl(NH<sub>3</sub>)<sub>2</sub>(H<sub>2</sub>O)]<sup>+</sup> have been explored in the NH/OH stretching region using a tabletop



optical parametric oscillator/amplifier (OPO/OPA) laser system coupled to a quadrupole ion trap mass spectrometer<sup>17-19</sup>. In order to aid in the interpretation of the IRMPD spectra, ab initio quantum chemical calculations have been performed. Optimized geometries for the species of interest have been obtained, and normal-mode frequency analysis has ensured their characterization as minimum-energy structures and provided theoretical IR spectra. Related to our study, theoretical investigations have been reported addressing the vibrational properties of cisplatin, transplatin, and water-substituted cisplatin complexes<sup>20-24</sup>. However, the availability of experimental data corroborating the theoretical results is critical. The primary reference for these studies relies on the IR spectra in the solid<sup>21,25,26</sup>. A vibrational spectroscopic study has been reported for the hydrated cisdiammineplatinum(II) ion,  $cis-[Pt(NH_3)_2(H_2O)_4]^{2+}$ , in acidic aqueous solution<sup>27</sup>. In this study, elucidating the IR bands for coordinated NH<sub>3</sub> and H<sub>2</sub>O has required subtraction of solvent bands, leaving weak residual bands. Obviously, this is not an issue in the presently described approach. The *cis*- and *trans*- $[PtCl(NH_3)_2(H_2O)]^+$  have been obtained as free, gaseous ions by electrospray ionization of aqueous solutions of *cis*- and *trans*-diamminedichloroplatinum(II), respectively. The ions were stored and mass selected in a Paul ion trap mass spectrometer. Irradiation by the tunable IR laser beam yields an IRMPD spectrum based on the frequencydependent photofragmentation yield associated with H<sub>2</sub>O loss.

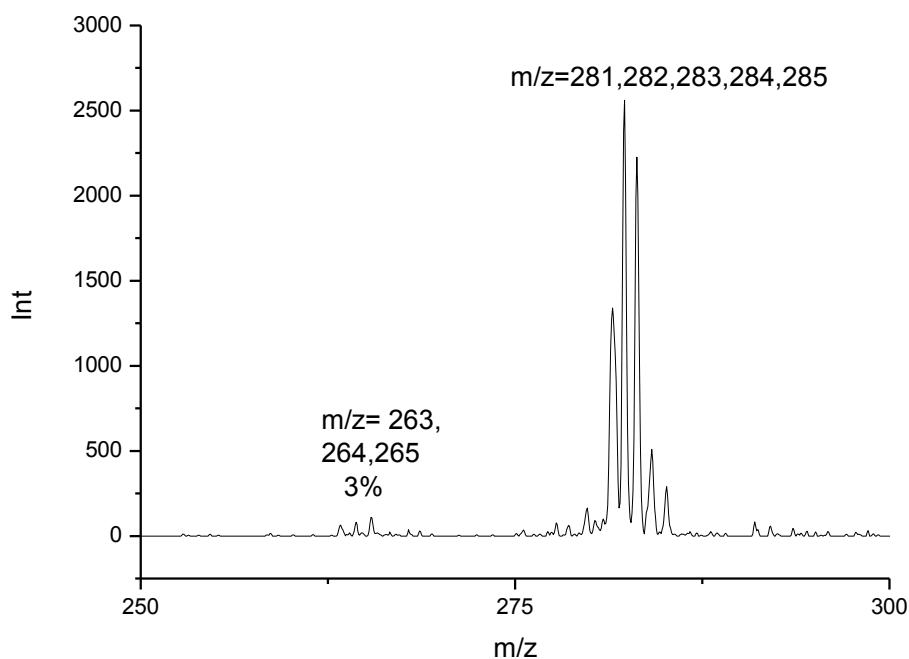


**Figure 1s.** Infra red induced mass spectrum (Ion abundances in arbitrary units) of *cis*-[PtCl(NH<sub>3</sub>)<sub>2</sub>(H<sub>2</sub>O)]<sup>+</sup> recorded at 3538 cm<sup>-1</sup>.

Figure 1 shows an exemplary mass spectrum recorded after irradiation of *cis*-[PtCl(NH<sub>3</sub>)<sub>2</sub>(H<sub>2</sub>O)]<sup>+</sup> ions with photons in resonance with an IR-active mode at 3538 cm<sup>-1</sup>. The IRMPD spectra of *cis*-[PtCl(NH<sub>3</sub>)<sub>2</sub>(H<sub>2</sub>O)]<sup>+</sup> and *trans*-[PtCl(NH<sub>3</sub>)<sub>2</sub>(H<sub>2</sub>O)]<sup>+</sup> plotted in Figures 2 and 3, respectively, are remarkably different, as expected from two distinct, noninterconverting species.

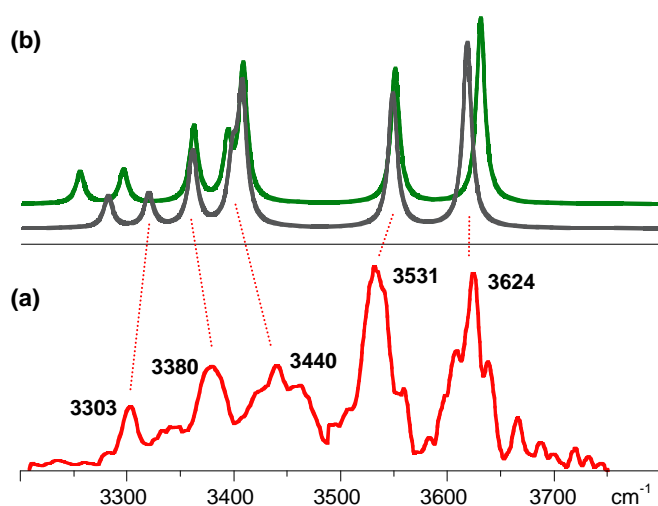


Figure 2. Experimental IRMPD spectrum (a) (red line) of *cis*-[PtCl(NH<sub>3</sub>)<sub>2</sub>(H<sub>2</sub>O)]<sup>+</sup> compared to calculated IR spectra (b) according to MP2 anharmonic (gray line) and harmonic (green line) frequency computations. Harmonic frequencies are scaled.

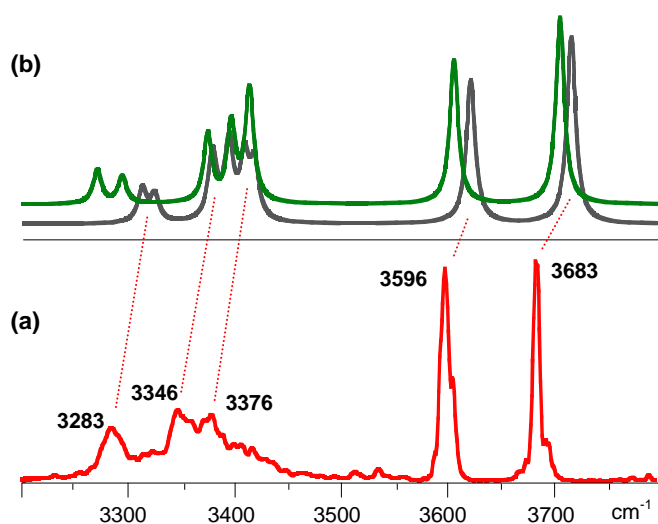
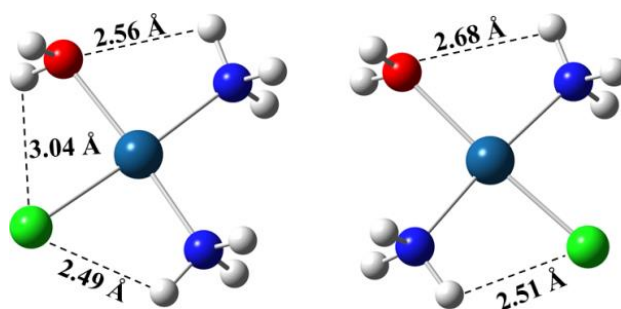


Figure 3. Experimental IRMPD spectrum (a) (red line) of *trans*-[PtCl(NH<sub>3</sub>)<sub>2</sub>(H<sub>2</sub>O)]<sup>+</sup> compared to calculated IR spectra (b) according to MP2 anharmonic (gray line) and harmonic (green line) frequency computations. Harmonic frequencies are scaled.

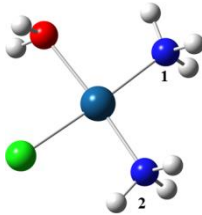
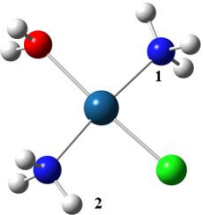
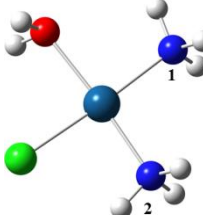
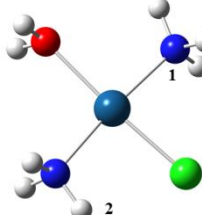
The most evident differences are in the two signatures for the OH stretching of the water ligand that appear as sharp bands at 3683 and 3596 cm<sup>-1</sup> in the IRMPD spectrum of the *trans* isomer whereas they look as broad signals at lower frequency, namely, at 3624 and 3531 cm<sup>-1</sup>, in the spectrum of the *cis* isomer. Notably, OH stretchings of coordinated water are observed in a remarkably low wavenumber region for hydrated Pt(II) ions in

water solution, likely due to extensive hydrogen bonding with the solvent<sup>27</sup>. These resonances are remarkably red-shifted with respect to the symmetric and asymmetric stretches of the free water molecule at 3657 and 3756  $\text{cm}^{-1}$ , respectively. Pronounced red shifts in these modes are however well-documented in water complexes of metal cations,  $\text{Me}^+(\text{H}_2\text{O})$ , sampled by IR spectroscopy using the method of argon tagging<sup>28</sup>. The effect is ascribed to the polarization of the lone pair electrons on oxygen, depleting electron density from the highest occupied molecular orbital of water and so weakening the O–H bonds. The photofragmentation yield is also different for the two isomers, reaching 0.10 in the case of the trans complex and only 0.02 from the cis one in their IRMPD spectra run under comparable conditions. This order of magnitude difference may be traced to the “*trans*” effect, positively influencing the departure of  $\text{H}_2\text{O}$  when the trans ligand is chlorine rather than ammonia in the square-planar complex<sup>29</sup>.



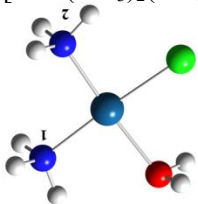
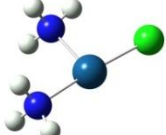
**Chart 1.** Structures of *cis*- $[\text{PtCl}(\text{NH}_3)_2(\text{H}_2\text{O})]^+$  and *trans*- $[\text{PtCl}(\text{NH}_3)_2(\text{H}_2\text{O})]^+$

The optimized structures of the two isomeric  $[\text{PtCl}(\text{NH}_3)_2(\text{H}_2\text{O})]^+$  complexes depicted in Chart 1 are obtained by calculations performed at MP2/cc-pVTZ level of theory using a relativistic pseudopotential (LANL2TZ) to describe the platinum atom as described in the Experimental Details. The trans configuration turns out to be energetically more favorable by about 3  $\text{kJ mol}^{-1}$ . Few exemplary hydrogen–heavy atom distances are reported in Chart 1, while more complete structural information is provided in Tables S1.

<i>MP2</i>		<i>B3LYP</i>	
<i>cis-</i> [Pt(NH <sub>3</sub> ) <sub>2</sub> Cl(H <sub>2</sub> O)] <sup>+</sup>	<i>trans-</i> [Pt(NH <sub>3</sub> ) <sub>2</sub> Cl(H <sub>2</sub> O)] <sup>+</sup>	<i>cis-</i> [Pt(NH <sub>3</sub> ) <sub>2</sub> Cl(H <sub>2</sub> O)] <sup>+</sup>	<i>trans-</i> [Pt(NH <sub>3</sub> ) <sub>2</sub> Cl(H <sub>2</sub> O)] <sup>+</sup>
$E_{rel} = 2.9 \text{ kJ mol}^{-1}$	$E_{rel} = 0.0 \text{ kJ mol}^{-1}$	$E_{rel} = 4.7 \text{ kJ mol}^{-1}$	$E_{rel} = 0.0 \text{ kJ mol}^{-1}$
			
<b>Bond Length (Å)</b>	<b>Bond Length (Å)</b>	<b>Bond Length (Å)</b>	<b>Bond Length (Å)</b>
Pt-N <sub>1</sub> 2.06	Pt-N <sub>1</sub> 2.03	Pt-N <sub>1</sub> 2.12	Pt-N <sub>1</sub> 2.07
Pt-N <sub>2</sub> 1.98	Pt-Cl 2.22	Pt-N <sub>2</sub> 2.04	Pt-Cl 2.26
Pt-Cl 2.25	Pt-N <sub>2</sub> 2.02	Pt-Cl 2.29	Pt-N <sub>2</sub> 2.08
Pt-O 2.08	Pt-O 2.13	Pt-O 2.12	Pt-O 2.18
<b>Angles (deg)</b>	<b>Angles (deg)</b>	<b>Angles (deg)</b>	<b>Angles (deg)</b>
O-Pt-N <sub>1</sub> 87.4	O-Pt-N <sub>1</sub> 88.3	O-Pt-N <sub>1</sub> 87.4	O-Pt-N <sub>1</sub> 87.9
N <sub>1</sub> -Pt-N <sub>2</sub> 96.6	N <sub>1</sub> -Pt-Cl 88.1	N <sub>1</sub> -Pt-N <sub>2</sub> 96.5	N <sub>1</sub> -Pt-Cl 88.8
N <sub>2</sub> -Pt-Cl 86.5	Cl-Pt-N <sub>2</sub> 86.6	N <sub>2</sub> -Pt-Cl 86.8	Cl-Pt-N <sub>2</sub> 86.9
Cl-Pt-O 89.5	N <sub>2</sub> -Pt-O 97.0	Cl-Pt-O 89.3	N <sub>2</sub> -Pt-O 96.4

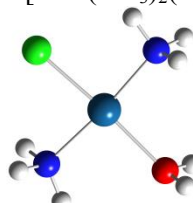
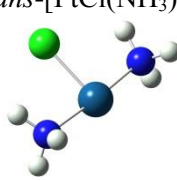
**Table S1.** Calculated parameters for *cis-* and *trans-*[PtCl(NH<sub>3</sub>)<sub>2</sub>(H<sub>2</sub>O)]<sup>+</sup> complexes obtained at MP2/cc-pVTZ and B3LYP/cc-pVTZ (Pt: LANL2TZ) level of theory.

Tables S3a and S3b summarize the computed electronic energies and zero-point vibrational energies of both the two isomeric [PtCl(NH<sub>3</sub>)<sub>2</sub>(H<sub>2</sub>O)]<sup>+</sup> complexes and their dissociation products involving loss of water. The data reported in Tables S3a and S3b (below) show that the H<sub>2</sub>O binding energy is 187 and 149 kJ mol<sup>-1</sup> for *cis-* and *trans-*[PtCl(NH<sub>3</sub>)<sub>2</sub>(H<sub>2</sub>O)]<sup>+</sup>, respectively.

Species	E <sup>a</sup>	ZPE <sup>b</sup>	E <sub>rel</sub> <sup>b</sup>
$cis\text{-}[\text{PtCl}(\text{NH}_3)_2(\text{OH}_2)]^+$ 	-767.3554274 [0]	285.8	0
$cis\text{-}[\text{PtCl}(\text{NH}_3)_2]^+$ 	-690.9601048 [0]	214.9	
H <sub>2</sub> O	-76.3186576 [0]	56.7	
$cis\text{-}[\text{PtCl}(\text{NH}_3)_2]^+ + \text{H}_2\text{O}$	-767.2787624	271.6	187.0

<sup>a</sup> In Hartree particle<sup>-1</sup>, number of imaginary frequencies in square brackets and size of the imaginary frequency in parentheses.  
<sup>b</sup> In kJ mol<sup>-1</sup>.

**Table S3a.** Absolute electronic energies, zero point energies (ZPE) and relative energies at 0K of  $cis\text{-}[\text{PtCl}(\text{NH}_3)_2(\text{H}_2\text{O})]^+$ ,  $cis\text{-}[\text{PtCl}(\text{NH}_3)_2]^+$  and H<sub>2</sub>O species. Computations at MP2/cc-pVTZ (Pt:LANL2TZ) level.

Species	E <sup>a</sup>	ZPE <sup>b</sup>	E <sub>rel</sub> <sup>b</sup>
$trans-[PtCl(NH_3)_2(OH_2)]^+$ 	-767.3565535 [0]	283.9	0
$trans-[PtCl(NH_3)_2]^+$ 	-690.9765107 [0]	215.4	
H <sub>2</sub> O	-76.3186576 [0]	56.7	
$trans-[PtCl(NH_3)_2]^+ + H_2O$	-767.2951683	272.1	149.3

**Table S3b.** Absolute electronic energies, zero point energies (ZPE) and relative energies at 0K of  $trans-[PtCl(NH_3)_2(H_2O)]^+$ ,  $trans-[PtCl(NH_3)_2]^+$  and H<sub>2</sub>O species. Computations at MP2/cc-pVTZ (Pt:LANL2TZ) level.

The size of the dissociation thresholds implies that the energy of four to five photons in the explored frequency range is required for the photofragmentation of water from the sampled complexes. The somewhat higher H<sub>2</sub>O binding energy for  $cis-[PtCl(NH_3)_2(H_2O)]^+$  is in line with the lower photofragmentation yield and could account for a more red-shifted IRMPD spectrum in comparison with the trans isomer<sup>30</sup>. However, this expectation is not borne out by the comparison of the experimental spectra with the IR spectra obtained by anharmonic calculations, as detailed in the following lines. The calculated frequencies allow a direct assignment of the IRMPD bands to the related vibrational modes, while computed IR spectra are drawn in Figures 2 and 3, either in the harmonic approximation or with anharmonic correction. A scaling factor of 0.951 was applied to the harmonic frequencies.

<u>Vibrational mode</u> <sup>a</sup>	<u>Experimental</u> <sup>b</sup>	<u>Theoretical</u> <sup>b,c</sup>
<i>cis</i> -[Pt(NH <sub>3</sub> ) <sub>2</sub> Cl(H <sub>2</sub> O)] <sup>+</sup>		
$\nu_{as}$ H <sub>2</sub> O	3624	3618 (184)
$\nu_s$ H <sub>2</sub> O	3531	3548 (133)
$\nu_{as}$ NH <sub>3</sub>	3440	3406 (134); 3405 (0.11)
$\nu_{as}$ NH <sub>3</sub>	3380	3396 (59); 3359 (75)
$\nu_s$ NH <sub>3</sub>	3303	3318 (33); 3280 (31)
<i>trans</i> -[Pt(NH <sub>3</sub> ) <sub>2</sub> Cl(H <sub>2</sub> O)] <sup>+</sup>		
$\nu_{as}$ H <sub>2</sub> O	3683	3715 (191)
$\nu_s$ H <sub>2</sub> O	3596	3620 (147)
$\nu_{as}$ NH <sub>3</sub>	3376	3417 (55); 3407 (61)
$\nu_{as}$ NH <sub>3</sub>	3346	3377 (69); 3393 (79)
$\nu_s$ NH <sub>3</sub>	3283	3323 (28); 3311 (34)

<sup>a</sup> $\nu_s$  and  $\nu_{as}$  stand for symmetric and asymmetric stretching modes, respectively. <sup>b</sup>cm<sup>-1</sup>. <sup>c</sup>Calculations at MP2/cc-pVTZ anharmonic level. IR intensity in parentheses (km mol<sup>-1</sup>).

**Table 1.** Vibrational frequencies for *cis*- and *trans*-[Pt(NH<sub>3</sub>)<sub>2</sub>Cl(H<sub>2</sub>O)]<sup>+</sup> complexes.

The anharmonic frequencies, devoid of any scaling factor, are listed in Table 1 and assigned to the experimentally observed features. The discrepancy between calculated anharmonic and observed frequencies is consistently less than 40 cm<sup>-1</sup>, or about 1%. The matching is overall less satisfactory when the IR spectra are obtained by hybrid DFT calculations at the B3LYP/cc-pVTZ level, as preliminarily performed and shown in Figure S2a/b.



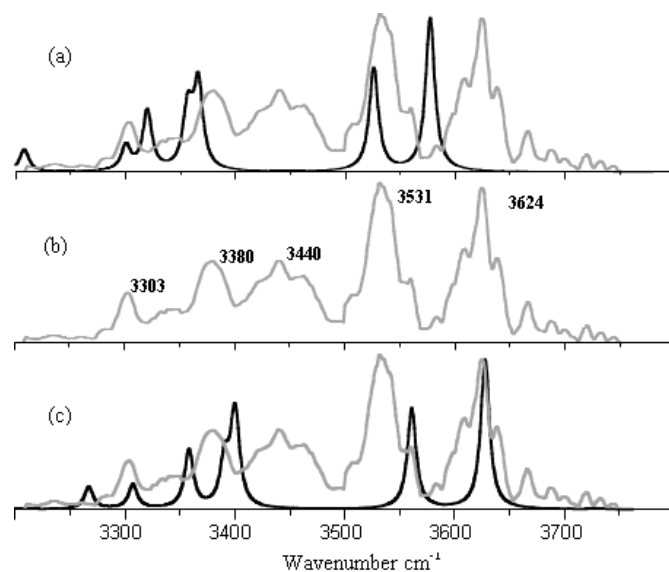


**Figure S2a.** Experimental IRMPD spectrum (a)(grey line) of *cis*-[PtCl(NH<sub>3</sub>)<sub>2</sub>(H<sub>2</sub>O)]<sup>+</sup> compared to calculated IR spectra according to B3LYP anharmonic (b)(black line) and harmonic (c)(black line) frequency computations in the region of 3200-3800 cm<sup>-1</sup>.

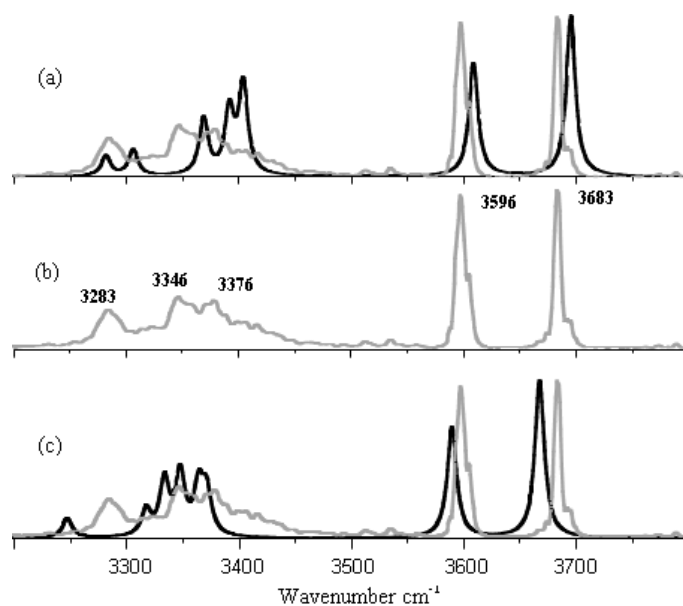


**Figure S2b.** Experimental IRMPD spectrum (a)(grey line) of *trans*-[PtCl(NH<sub>3</sub>)<sub>2</sub>(H<sub>2</sub>O)]<sup>+</sup> compared to calculated IR spectra according to B3LYP anharmonic (b)(black line) and harmonic (c)(black line) frequency computations in the region of 3200-3800 cm<sup>-1</sup>.

In the *cis* complex, one may recognize the presence of hydrogen bond interactions between the water H atoms and the neighboring Cl in a bifurcated bonding motif. The spectral reflection of this interaction lies in the relatively low frequency and comparatively large bandwidth for the OH stretching modes, already noted characteristics of the IRMPD spectrum of *cis*-[PtCl(NH<sub>3</sub>)<sub>2</sub>(H<sub>2</sub>O)]<sup>+</sup>. The asymmetric stretch frequency, *vas* H<sub>2</sub>O, is shifted by ~60 cm<sup>-1</sup> while the symmetric one, *vs* H<sub>2</sub>O, is shifted by 65 cm<sup>-1</sup> upon going from the *trans* to the *cis* isomer. NH groups of NH<sub>3</sub> ligands can in turn act as hydrogen bond donors in the molecular plane. Both *cis* and *trans* isomers present NH···Cl and NH···O interactions, the former slightly stronger than the latter. The symmetric stretch frequency, *vs* NH<sub>3</sub>, involving the NH<sub>3</sub> ligand holding a coplanar Pt—Cl···H—N arrangement is in fact systematically computed at lower frequency relative to *vs* NH<sub>3</sub>, involving the NH<sub>3</sub> ligand holding a coplanar Pt—O···H—N arrangement. The similar performance of these interactions in the two isomers is in agreement with the close position of the IRMPD band for *vs* NH<sub>3</sub> at 3303 cm<sup>-1</sup> for the *cis* and 3283 cm<sup>-1</sup> for the *trans* isomer. Other absorptions in the 3320–3550 cm<sup>-1</sup> range are assigned to asymmetric N—H stretching modes of the NH<sub>3</sub> ligands, and here, specific relationships to structural features are more difficult to trace.

In summary, we have presented vibrational spectroscopic data about the first intermediate in the hydrolytic path of cisplatin and transplatin. The intermediates have been obtained as free, long-lived ions in the gas-phase, and their sampling by IRMPD spectroscopy has revealed vibrational features unaffected by interferences due to the medium. This notion has allowed a direct interpretation of the IR signatures, backed by the results of MP2 calculations of the naked ions, which were thus characterized as distinct, noninterconverting species.

### 2.3. Experimental Method

The *cis*- and *trans*-diamminedichloroplatinum(II) were research-grade products from commercial sources (Sigma-Aldrich s.r.l. Milan, Italy). Stock aqueous solutions (1–2 × 10<sup>-3</sup> M) were obtained by magnetic stirring, which were then diluted to ~1 × 10<sup>-4</sup> M in water. The solutions were infused at a flow rate of 10 μL/min by a syringe pump to the electrospray ionization source of a Paul ion trap mass spectrometer (Esquire 6000+,

Bruker) allowing *cis*- and *trans*-[PtCl(NH<sub>3</sub>)<sub>2</sub>(H<sub>2</sub>O)]<sup>+</sup> complexes to be delivered as gaseous ions. The ions were massselected in the ion trap as the entire isotopic cluster comprising the predominant combinations of platinum and chlorine isotopes at *m/z* 281–285. The mass spectrometer is coupled to the beamline of an optical parametric oscillator/amplifier (OPO/OPA, LaserVision) laser. The parametric converter is pumped by a nonseeded Nd:YAG laser (Continuum Surlite II) operating at a 10 Hz repetition rate. The typical pulse width of this pump laser is 4–6 ns, with an output pulse energy of 600 mJ at 1064 nm. The OPO/OPA laser is tunable from 2000 to 4000 cm<sup>-1</sup>, and tunability is achieved by angle tuning of OPO and OPA crystals simultaneously. The angle tuning is controlled precisely using software-controlled stepping motors. The typical output energy from the OPO/OPA was 22–24 mJ/pulse in the spectral range of investigation, with a 3–4 cm<sup>-1</sup> bandwidth. The mid-IR output from the OPO/OPA is directed in the ion trap using a gold-coated plane mirror and is focused loosely using a MgF<sub>2</sub> lens. IR beam focusing is performed to achieve better overlap with the trapped ion cloud. Ions were accumulated for 50 ms prior to IR irradiation. The typical irradiation time used in the experiments was 2–4 s. The irradiation time is controlled using an electromechanical shutter synchronized precisely with the mass spectrometer. The ion abundances in the mass spectra recorded at each wavenumber allow calculation of the IRMPD yield,  $R = -\log[I_{\text{parent}}/(I_{\text{parent}} + \Sigma I_{\text{fragment}})]$ , where  $I_{\text{parent}}$  and  $I_{\text{fragment}}$  are the ion signal intensities for the parent and fragment ions, respectively.  $R$  is plotted against the wavenumber of the IR radiation to deliver the IRMPD spectra. Calculations were performed using the GAUSSIAN 03W (G03W) package<sup>31</sup>. In order to evaluate the effect of electron correlation (known to be particularly meaningful in systems containing transition-metal atoms)<sup>32</sup> on the predicted structural parameters and vibrational frequencies, different theoretical methods were considered, namely, the B3LYP<sup>33,34</sup> Density Functional and MP2<sup>35–38</sup> levels of theory, as implemented in G03W. Geometries were fully optimized by the Berny algorithm using redundant internal coordinates. Tight convergence criteria (G03W keyword opt = tight) were used in the optimization, namely, 0.000015 hartree/bohr for maximum force, 0.000010 hartree/bohr for root-mean-square force, 0.000060 bohr for maximum displacement, and 0.000040 bohr for root-mean-square displacement. For the nonmetal atoms, different basis sets were tested, cc-pVDZ and cc-pVTZ. In all cases, the relativistic LANL2TZ pseudopotential developed by Hay and Wadt<sup>39</sup> in a triple- $\zeta$  splitting scheme was used to

describe the platinum atom. The Pt-ECP scheme considers the outermost core electrons ( $5s^2$  and  $5p^6$ ) explicitly in the valence shell. In all cases, harmonic vibrational frequency calculations were performed to verify that the geometries correspond to a real minimum in the potential energy surface (no negative eigenvalues) as well as to quantify the zero-point vibrational energy correction. Vibrational frequencies are routinely computed assuming the harmonic approximation. To correct for the neglect of higherorder terms (anharmonicity), along with the inherent approximations of the employed level of theory, the harmonic frequencies are typically corrected by using an empirical method-dependent multiplicative scaling factor. In this work, a scaling factor of 0.961 was used for harmonic B3LYP calculations, and a value of 0.951 was used for harmonic MP2 calculations in the 3200–3800  $\text{cm}^{-1}$  frequency range. The introduction of anharmonic corrections greatly improves the agreement of the computed absorption bands with the experimental bands and often eliminates (or reduces) the need for empirical scaling factors. Anharmonic corrections were thus computed by numerical differentiation along normal modes, according to the scheme implemented in G03W. All frequencies obtained by anharmonic calculations are unscaled. To be consistent with the experimental spectral resolution, all calculated absorption lines were convoluted with a Lorentzian profile of 5  $\text{cm}^{-1}$ . The anharmonic simulations use anharmonic frequencies but with harmonic intensities.

## 2.4. References

- (1) Rosenberg, B. V. C.; Trosko, J. E.; Mansour, V. H. Platinum Compounds: a New Class of Potent Antitumour Agents *Nature* **1969**, 222, 385–386.
- (2) Berners-Price, S. J.; Appleton, T. G. The Chemistry of Cisplatin in Aqueous Solution. In *Platinum-Based Drugs in Cancer Therapy*; Kelland, L. R., Farrell, N., Eds.; *Humana Press* Totowa, NJ, **2000**; p 3.
- (3) Davies, M. S.; Berners-Price, S. J.; Hambley, T. W. Slowing of Cisplatin Aquation in the Presence of DNA but Not in the Presence of Phosphate: Improved Understanding of Sequence Selectivity and the Roles of Monoaquated and Diaquated Species in the Binding of Cisplatin to DNA *Inorg. Chem.* **2000**, 39, 5603–5613.
- (4) Bancroft, D. P.; Lepre, C. A.; Lippard, S. J. Pt-195 NMR Kinetic and Mechanistic Studies of *cis*-Diamminedichloroplatinum and *trans*-Diamminedichloroplatinum(II) Binding to DNA *J. Am. Chem. Soc.* **1990**, 112, 6860–6871.
- (5) Jamieson, E. R.; Lippard, S. J. Structure, Recognition, and Processing of Cisplatin-DNA Adducts. *Chem. Rev.* **1999**, 99, 2467–2498.
- (6) Monjardet-Bas, V.; Bombard, S.; Chottard, J. C.; Kozelka, M. GA and AG Sequences of DNA React with Cisplatin at Comparable Rates *Chem. Eur. J.* **2003**, 9, 4739–4745.
- (7) Burda, J. V.; Zeizinger, M.; Leszczynski, J. Activation Barriers and Rate Constants for Hydration of Platinum and Palladium Square-Planar Complexes: An Ab Initio Study *J. Chem. Phys.* **2004**, 120, 1253–1262.
- (8) Rotzinger, F. P. Treatment of Substitution and Rearrangement Mechanisms of Transition Metal Complexes with Quantum Chemical Methods *Chem. Rev.* **2005**, 105, 2003–2037.
- (9) Zhang, Y.; Guo, Z. J.; You, X. Z. Hydrolysis Theory for Cisplatin and Its Analogues Based on Density Functional Studies *J. Am. Chem. Soc.* **2001**, 123, 9378–9387.
- (10) Jalilvand, F.; Laffin, L. J. Structure of the Hydrated Platinum(II) Ion and the *cis*-Diammineplatinum(II) Complex in Acidic Aqueous Solution: An EXAFS Study *Inorg. Chem.* **2008**, 47, 3248–3254.
- (11) Eyler, J. R. Infrared Multiple Photon Dissociation Spectroscopy of Ions in Penning Traps *Mass Spectrom. Rev.* **2009**, 28, 448–467.
- (12) Polfer, N. C. Infrared Multiple Photon Dissociation Spectroscopy of Trapped Ions *Chem. Soc. Rev.* **2011**, 40, 2211–2221.
- (13) Roithova, J. Characterization of Reaction Intermediates by Ion Spectroscopy *Chem. Soc. Rev.* **2012**, 41, 547–559.
- (14) Crestoni, M. E.; Chiavarino, B.; Steinmetz, V.; Fornarini, S. Communication: Vibrational Study of a Benzyl Carbanion: Deprotonated 2,4-Dinitrotoluene *J. Chem. Phys.* **2012**, 137, 181101.
- (15) Chiavarino, B.; Crestoni, M. E.; Dopfer, O.; Maitre, P.; Fornarini, S. Benzylum versus Tropylium Ion Dichotomy: Vibrational Spectroscopy of Gaseous C<sub>8</sub>H<sub>9</sub><sup>+</sup> Ions *Angew. Chem., Int. Ed.* **2012**, 51, 4947–4949.
- (16) Chiavarino, B.; Crestoni, M. E.; Fornarini, S.; Taioli, S.; Mancini, I.; Tosi, P. Infrared Spectroscopy of Copper–Resveratrol Complexes: A Joint Experimental and Theoretical Study *J. Chem. Phys.* **2012**, 137, 024307.
- (17) Crestoni, M. E.; Chiavarino, B.; Scuderi, D.; Di Marzio, A.; Fornarini, S. Discrimination of 4-Hydroxyproline Diastereomers by Vibrational Spectroscopy of the Gaseous Protonated Species *J. Phys. Chem. B* **2012**, 116, 8771–8779.
- (18) Sinha, R. K.; Maitre, P.; Piccirillo, S.; Chiavarino, B.; Crestoni, M. E.; Fornarini, S. Cysteine Radical Cation: A Distonic Struccare Probed by Gas-Phase IR Spectroscopy *Phys. Chem. Chem. Phys.* **2010**, 12, 9794–9800.
- (19) Chiavarino, B.; Crestoni, M. E.; Fornarini, S.; Scuderi, D.; Salpin, J. Y. Interaction of Cisplatin with Adenine and Guanine: A Combined IRMPD, MS/MS, and Theoretical Study *J. Am. Chem. Soc.* **2013**, 135, 1445–1455.
- (20) Carloni, P.; Andreoni, W.; Hutter, J.; Curioni, A.; Giannozzi, P.; Parrinello, M. Structure and Bonding in Cisplatin and Other Pt(II)Complexes *Chem. Phys. Lett.* **1995**, 234, 50–56.
- (21) Pavankumar, P. N. V.; Seetharamulu, P.; Yao, S.; Saxe, J. D.; Reddy, D. G.; Hausheer, F. H. Comprehensive Ab Initio Quantum Mechanical and Molecular Orbital (MO) Analysis of Cisplatin: Structure, Bonding, Charge Density, and Vibrational Frequencies *J. Comput. Chem.* **1999**, 20, 365–382.

- (22) Costa, L. A. S.; Rocha, W. R.; De Almeida, W. B.; Dos Santos, H. F. The Hydrolysis Process of the *cis*-Dichloro(ethylenediamine)-platinum(II): A Theoretical Study *J. Chem. Phys.* **2003**, 118, 10584–10592.
- (23) Michalska, D.; Wysokinski, R. The Prediction of Raman Spectra of Platinum(II) Anticancer Drugs by Density Functional Theory *Chem. Phys. Lett.* **2005**, 403, 211–217.
- (24) Amado, A. M.; Fiuza, S. M.; Marques, M. P. M.; de Carvalho, L. A. E. B. Conformational and Vibrational Study of Platinum(II) Anticancer Drugs: *cis*-Diamminedichloroplatinum(II) as a Case Study *J. Chem. Phys.* **2007**, 127, 185104.
- (25) Nakamoto, K.; McCarthy, P. J.; Fujita, J.; Condrate, R. A.; Behnke, G. T. Infrared Studies of Ligand–Ligand Interaction in Dihalogenodiammineplatinum(II) Complexes *Inorg. Chem.* **1965**, 4, 36–43.
- (26) Wysokinski, R.; Michalska, D. The Performance of Different Density Functional Methods in the Calculation of Molecular Structures and Vibrational Spectra of Platinum(II) Antitumor Drugs: Cisplatin and Carboplatin *J. Comput. Chem.* **2001**, 22, 901–912.
- (27) Kocsis, L.; Mink, J.; Jalilehvand, F.; Laffin, L. J.; Berkesi, O.; Hajba, L. Vibrational Spectroscopic Study of the Hydrated Platinum-(II), Palladium(II) and *cis*-Diammineplatinum(II) Ions in Acidic Aqueous Solutions *J. Raman Spectrosc.* **2009**, 40, 481–490.
- (28) Carnegie, P. D.; Bandyopadhyay, B.; Duncan, M. A. Infrared Spectroscopy of  $Mn^+(H_2O)$  and  $Mn^{2+}(H_2O)$  via Argon Complex Predissociation *J. Phys. Chem. A* **2011**, 115, 7602–7609 and references therein.
- (29) Appleton, T. G.; Clarck, H. C.; Manzer, L. E. The *Trans*-Influence: Its Measurement and Significance *Coord. Chem. Rev.* **1973**, 10, 335–422.
- (30) Oomens, J.; Sartakov, B. G.; Meijer, G.; von Helden, G. Gas-Phase Infrared Multiple Photon Dissociation Spectroscopy of Mass-Selected Molecular Ions *Int. J. Mass Spectrom.* **2006**, 254, 1–19.
- (31) Frisch, M. J.; Trucks, G. W.; Schlegel, H. B.; Scuseria, G. E.; Robb, M. A.; Cheeseman, J. R.; Montgomery, J. A., Jr.; Vreven, T.; Kudin, K. N.; Burant, J. C.; Millam, J. M.; Iyengar, S. S.; Tomasi, J.; Barone, V.; Mennucci, B.; Cossi, M.; Scalmani, G.; Rega, N.; Petersson, G. A.; Nakatsuji, H.; Hada, M.; Ehara, M.; Toyota, K.; Fukuda, R.; Hasegawa, J.; Ishida, M.; Nakajima, T.; Honda, Y.; Kitao, O.; Nakai, H.; Klene, M.; Li, X.; Knox, J. E.; Hratchian, H. P.; Cross, J. B.; Bakken, V.; Adamo, C.; Jaramillo, J.; Gomperts, R.; Stratmann, R. E.; Yazyev, O.; Austin, A. J.; Cammi, R.; Pomelli, C.; Ochterski, J. W.; Ayala, P. Y.; Morokuma, K.; Voth, G. A.; Salvador, P.; Dannenberg, J. J.; Zakrzewski, V. G.; Dapprich, S.; Daniels, A. D.; Strain, M. C.; Farkas, O.; Malick, D. K.; Rabuck, A. D.; Raghavachari, K.; Foresman, J. B.; Ortiz, J. V.; Cui, Q.; Baboul, A. G.; Clifford, S.; Cioslowski, J.; Stefanov, B. B.; Liu, G.; Liashenko, A.; Piskorz, P.; Komaromi, I.; Martin, R. L.; Fox, D. J.; Keith, T.; Al-Laham, M. A.; Peng, C. Y.; Nanayakkara, A.; Challacombe, M.; Gill, P. M. W.; Johnson, B.; Chen, W.; Wong, M. W.; Gonzalez, C.; Pople, J. A. Gaussian 03, revision D.01; Gaussian, Inc.: Wallingford, CT, **2004**.
- (32) Chermette, H. Density Functional Theory: A Powerful Tool for Theoretical Studies in Coordination Chemistry *Coord. Chem. Rev.* **1998**, 178, 699–721.
- (33) Lee, C. T.; Yang, W. T.; Parr, R. G. Local Softness and Chemical-Reactivity in the Molecules CO, SCN<sup>-</sup>, and H<sub>2</sub>CO *J. Mol. Struct.* **1988**, 40, 305–313.
- (34) Becke, A. D. Density-Functional Thermochemistry. The Role of Exact Exchange *J. Chem. Phys.* **1993**, 98, 5648–5652.
- (35) Frisch, M. J.; Head-Gordon, M.; Pople, J. A. Semidirect Algorithms for the MP2 Energy and Gradient *Chem. Phys. Lett.* **1990**, 166, 281–289.
- (36) Frisch, M. J.; Head-Gordon, M.; Pople, J. A. A Direct MP2 Gradient-Method *Chem. Phys. Lett.* **1990**, 166, 275–280.
- (37) Frisch, M.; Head-Gordon, M.; Pople, J. Direct Analytic SCF Second Derivatives and Electric-Field Properties *Chem. Phys.* **1990**, 141, 189–196.
- (38) Head-Gordon, M.; Pople, J. A.; Frisch, M. J. MP2 Energy Evaluation by Direct Methods *Chem. Phys. Lett.* **1988**, 153, 503–506.
- (39) Hay, P. J.; Wadt, W. R. Ab Initio Effective Core Potentials for Molecular Calculations - Potentials for K to Au Including the Outermost Core Orbitals *J. Chem. Phys.* **1985**, 82, 299–310.

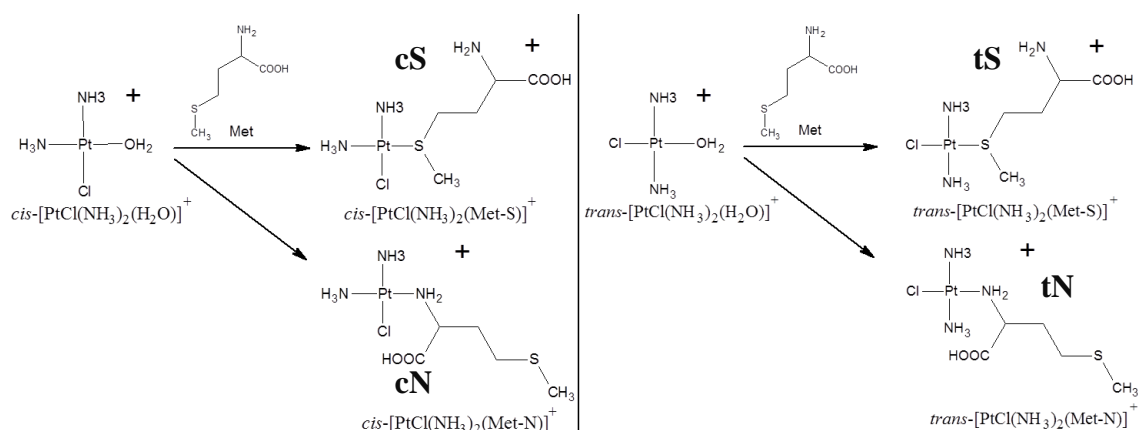
## CHAPTER 3

### **Cisplatin and transplatin complexes with L-methionine:**

#### **an assay by IRMPD spectroscopy**

### 3.1. Introduction

In platinum(II) drugs the most important hydrolytic product is the *cis*-[PtCl(NH<sub>3</sub>)<sub>2</sub>(H<sub>2</sub>O)]<sup>+</sup> cation. This cationic species is highly reactive because water can be substituted easily by donor ligands (e.g. nitrogen, sulphur) and this monoaqua complex is also believed to react with one of the nitrogen-containing bases of DNA with the loss of water. Elucidation of the mechanism of interaction between cisplatin and transplatin with aminoacids could throw light on the spectrum of activity and high toxicity of this drugs<sup>1</sup>. Sulfur-containing amino acids such as methionine have strong affinity for Pt(II) and could form very stable adduct<sup>2,3</sup>. The binding with L-methionine decreases the rate of reaction of cisplatin with base residues in DNA. At the same time, the possibility that cisplatin bound to methionine residues serves as a drug reservoir available for platination of DNA in the nucleus of tumor cells appears likely. The interaction of Pt(II) complexes with sulfur-containing biomolecules has been associated to resistance, nephrotoxicity and neurotoxicity<sup>4</sup>; however, it has been also suggested that reactions of platinum with biological thiols (e.g. GSH, methionine, cysteine) may be a pathway for drug detoxification and<sup>5</sup>. In cisplatin, strong sulphur *trans* effect and *trans* influence can contribute to the ammonia release, and this mechanism can possibly lead to cisplatin inactivation<sup>6,7</sup>. Pt(II)-sulphur adducts have been postulated to be a drug reservoir for platinum and may act as intermediates of platinum compounds and transform them into Pt-DNA adducts<sup>8,9</sup>.



**Scheme 1.** Reactions of *cis*- and *trans*-[PtCl(NH<sub>3</sub>)<sub>2</sub>(H<sub>2</sub>O)]<sup>+</sup> with L-methionine at the sulfur and nitrogen binding sites.



L-methionine and cisplatin or transplatin may form various complexes. The reaction sequence with methionine may first involve the formation of the potent electrophilic intermediate, *cis*-[PtCl(NH<sub>3</sub>)<sub>2</sub>(H<sub>2</sub>O)]<sup>+</sup> and *trans*-[PtCl(NH<sub>3</sub>)<sub>2</sub>(H<sub>2</sub>O)]<sup>+</sup>, by chloride substitution by water (Scheme 1). For cisplatin, the first ligand-exchange product is the monodentate adduct, where the water molecule is replaced by L-methionine either at the sulfur or the nitrogen site, so yielding *cis*-[PtCl(NH<sub>3</sub>)<sub>2</sub>(Met-S)]<sup>+</sup> and *cis*-[PtCl(NH<sub>3</sub>)<sub>2</sub>(Met-N)]<sup>+</sup>, respectively. A similar chemical behavior may be expected for transplatin.

### 3.2. Experimental Details

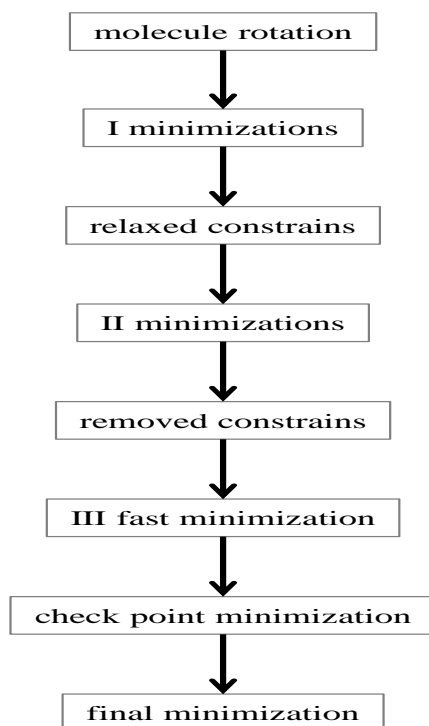
The *cis*- and *trans*-[PtCl(NH<sub>3</sub>)<sub>2</sub>(Met)]<sup>+</sup> (*m/z* 412) have been obtained as free, gaseous ions by electrospray ionization of aqueous solutions of *cis*- and *trans*-diamminedichloroplatinum(II) mixed with L-methionine. The electrosprayed ions were first stored and mass-selected in the analyzer of a mass spectrometer, and then irradiated by the tunable and bright IR laser beam at the CLIO-FEL facility. The IRMPD spectra based on the frequency dependent fragmentation yield associated with NH<sub>3</sub> loss were recorded. Figures 1/1a and 3/3a shows two mass spectrum recorded after irradiation of *cis*-[PtCl(NH<sub>3</sub>)<sub>2</sub>(Met)]<sup>+</sup> and *trans*-[PtCl(NH<sub>3</sub>)<sub>2</sub>(Met)]<sup>+</sup> (*m/z* 412) respectively, obtained in two different spectral regions, the so-called fingerprint region (800-2000 cm<sup>-1</sup>), using the beamline of the IR-FEL at CLIO, coupled to a modified Ft-icr mass spectrometer, and in the X-H (X = C,N,O) stretching region (2900-3700 cm<sup>-1</sup>), using a tabletop IR OPO/OPA laser coupled to a modified Paul ion-trap. In order to support the IRMPD spectroscopy data obtained on the selected ions, an high-performance ab initio package (Jaguar) was employed. Jaguar is a very helpful software in treating metal containing systems. Conversely, molecular mechanics method, like MMFF for example, are very limited by their parametrization, and often fail to treat metal containing systems, or experience large errors in computed results. High-level quantum mechanics is still the most accurate and direct way to study these challenging systems, despite the increased computational cost, due to the presence of the platinum(II) atom ([Xe] 4f<sup>14</sup> 5d<sup>8</sup>). On the first ten conformers, geometry optimization and vibrational frequencies were obtained with the Density

Functional Theory method, largely discussed in the general introduction of this thesis. Geometries were fully optimized testing the 6-31g\* basis set. Instead, the platinum atom was treated with the relativistic LANL2DZ pseudopotential. In all cases, harmonic vibrational frequency calculations were performed to verify that the geometries correspond to a real minimum in the potential energy surface (no negative eigenvalue). A scaling factor of 0.98 and 0.96 was used for the vibrational analysis in the 800-2000 cm<sup>-1</sup> and 2900-3700 cm<sup>-1</sup> frequency range, respectively.

### **3.3. Results and Discussion**

#### **3.3.1. Conformational Analysis**

In this work, a variety of possible side chain arrangements within the monodentate complexes of platinum drugs with methionine was explored using a conformational analysis with SPARTAN for the four possible monodentate structures shown in Scheme 1 (**cS**, **cN**, **tS**, **tN**). The Merck molecular force field (MMFF) was used in order to accurately treat conformational changes and non-bonding interactions both in gas-phase and condensed phase calculation. The conformational search were obtained with the help of a MONTECARLO algorithm and a simulated annealing method to generate conformers. The algorithm permits to randomly rotate bonds within the molecule until a preferential (minimum energy) geometry is attained. Initially, the molecule is considered to be in a high-temperature system; this means that it has enough energy and is thus flexible enough to move from a low to a high energy conformation. Often the global minimum configuration of a molecule may be very different from the initial conformation. As more conformations are explored, the temperature of the system decrease, making the molecule less inclined to move out of low energy conformations, and thus looking more closely at other minima in the currently nearby proximity (Scheme 2).



**Scheme 2.** Workflow of the minimization method in SPARTAN

After the final minimization step, twenty conformers for each structure of Scheme 1 were obtained. Only the energy of the first ten most stable conformers are listed in Table 1, selected with a cutoff energy of  $40 \text{ kJ mol}^{-1}$ . The structures deriving from the nitrogen chelation in *cis*-[PtCl(NH<sub>3</sub>)<sub>2</sub>(Met-N)]<sup>+</sup> (isomers **cN**) and in *trans*-[PtCl(NH<sub>3</sub>)<sub>2</sub>(Met-N)]<sup>+</sup> (isomers **tN**) are lower in energy than the sulfur chelating counterpart, where the chelating atom is the sulfur (isomers **cS** and **tS**). Furthermore, the platination on the N position in the *trans*-isomer results as the most stable structure (isomer **tN**), placed about  $13 \text{ kJ mol}^{-1}$  below the *cis*- one (**cN**).

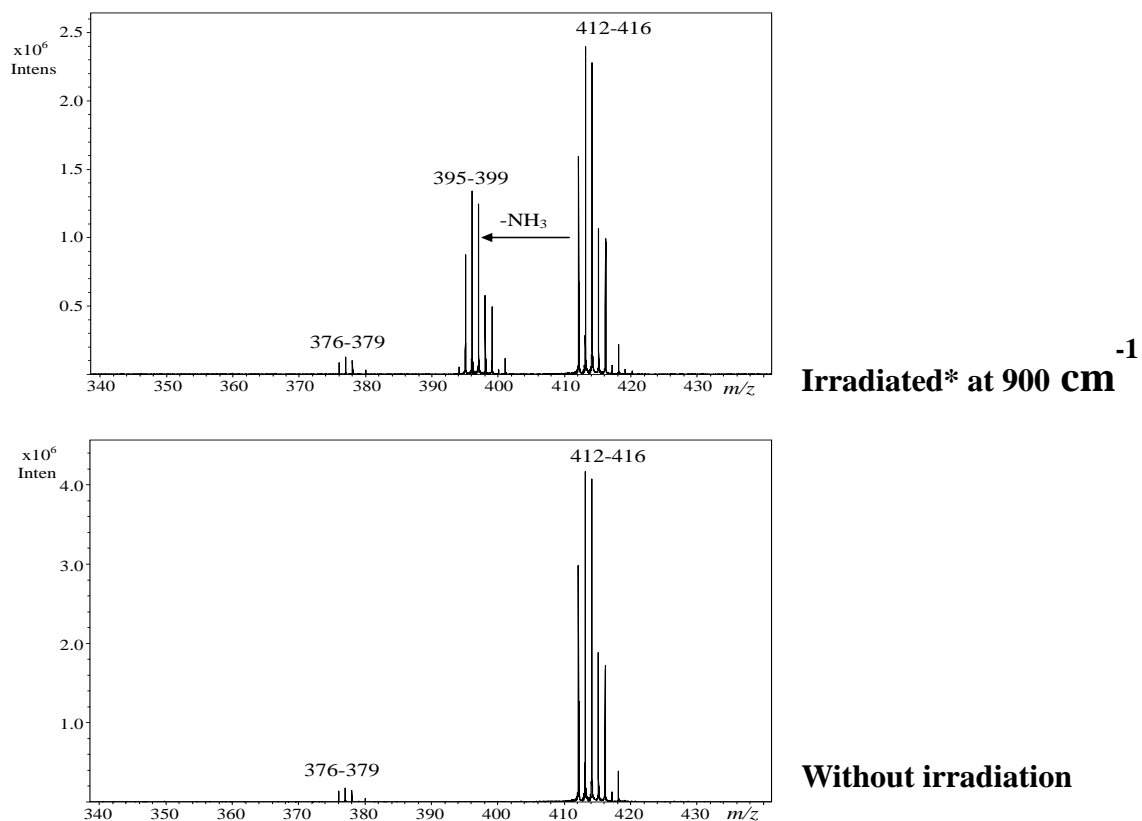
rank number	cS	cN	tS	tN
<b>1</b>	4.43	0.00	11.70	0.00
<b>2</b>	6.10	0.67	11.74	1.35
<b>3</b>	10.01	3.35	11.76	3.20
<b>4</b>	11.48	6.65	12.33	3.97
<b>5</b>	20.73	6.67	12.34	28.19
<b>6</b>	21.08	6.89	14.00	30.12
<b>7</b>	22.36	7.60	17.21	30.76
<b>8</b>	23.45	9.02	17.54	33.24
<b>9</b>	24.70	13.04	22.73	34.87
<b>10</b>	24.72	13.12	22.84	38.35

\* Values are given in kJ mol<sup>-1</sup>

**Table 1.** Relative energies of all calculated conformers at the DFT level of theory. Isomer **tN1** is the most stable structure.

### 3.3.2. Vibrational analysis

The aim of this study is to gather a structural characterization of the four families of free, monodentate adducts *cis*- and *trans*-[PtCl(NH<sub>3</sub>)<sub>2</sub>(Met)]<sup>+</sup> (**cS**, **cN**, **tS**, **tN**) at *m/z* 412 by means of IRMPD spectroscopy and theoretical chemistry. Figure 1 shows an exemplary mass spectrum recorded after irradiation of *cis*-[PtCl(NH<sub>3</sub>)<sub>2</sub>Cl(Met)]<sup>+</sup> ions with photons in resonance with an IR-active mode at 3490 cm<sup>-1</sup>.



**Spectrum 1.** Infra red induced mass spectrum (Ion abundances in arbitrary units) of  $cis$ -[PtCl(NH<sub>3</sub>)<sub>2</sub>(Met)]<sup>+</sup> recorded at 990 cm<sup>-1</sup>.

Some structural features of methionine interaction with cisplatin via sulphur or nitrogen atoms have been obtained in recent years<sup>10</sup>, and the sulphur atom was identified as the preferred platination target<sup>3</sup>. For this reason, both sulfur and nitrogen methionine binding sites were considered here in order to describe potential candidates for the [PtCl(NH<sub>3</sub>)<sub>2</sub>(Met)]<sup>+</sup> complexes obtained in solution and transferred to the gas-phase by ESI. Figure 1 illustrates the most stable monodentate conformers obtained for the **cS** complexes at the B3LYP/6-31g\* level of theory.

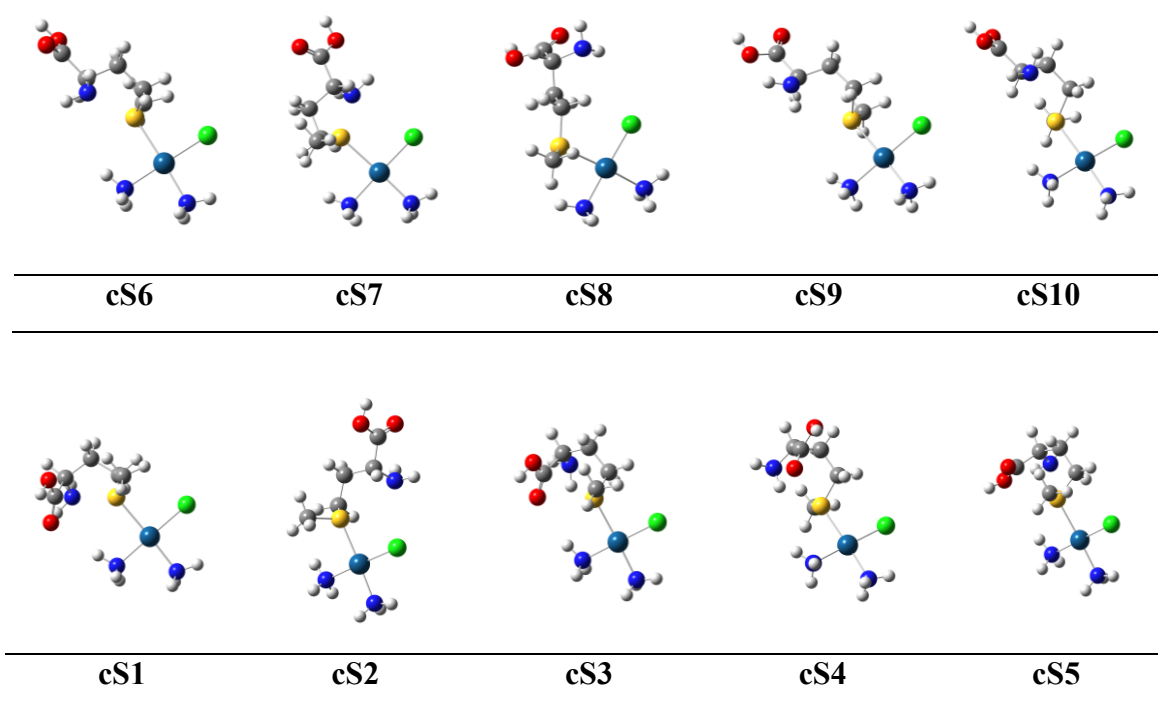


**Figure 1.** Optimized structures of the most stable ten conformers of general formula  $cis\text{-}[\text{PtCl}(\text{NH}_3)_2(\text{Met-S})]^+$  at the B3LYP/631g\* level of theory.

In order to extrapolate structural informations, the IRMPD spectrum of **cS/cN** ions is compared with the calculated IR spectra of the first five potential candidate conformers (Figure 2). According to Scheme 1, binding of cisplatin or transplatin to either S or N gives rise to the two list of conformers of Table 1.

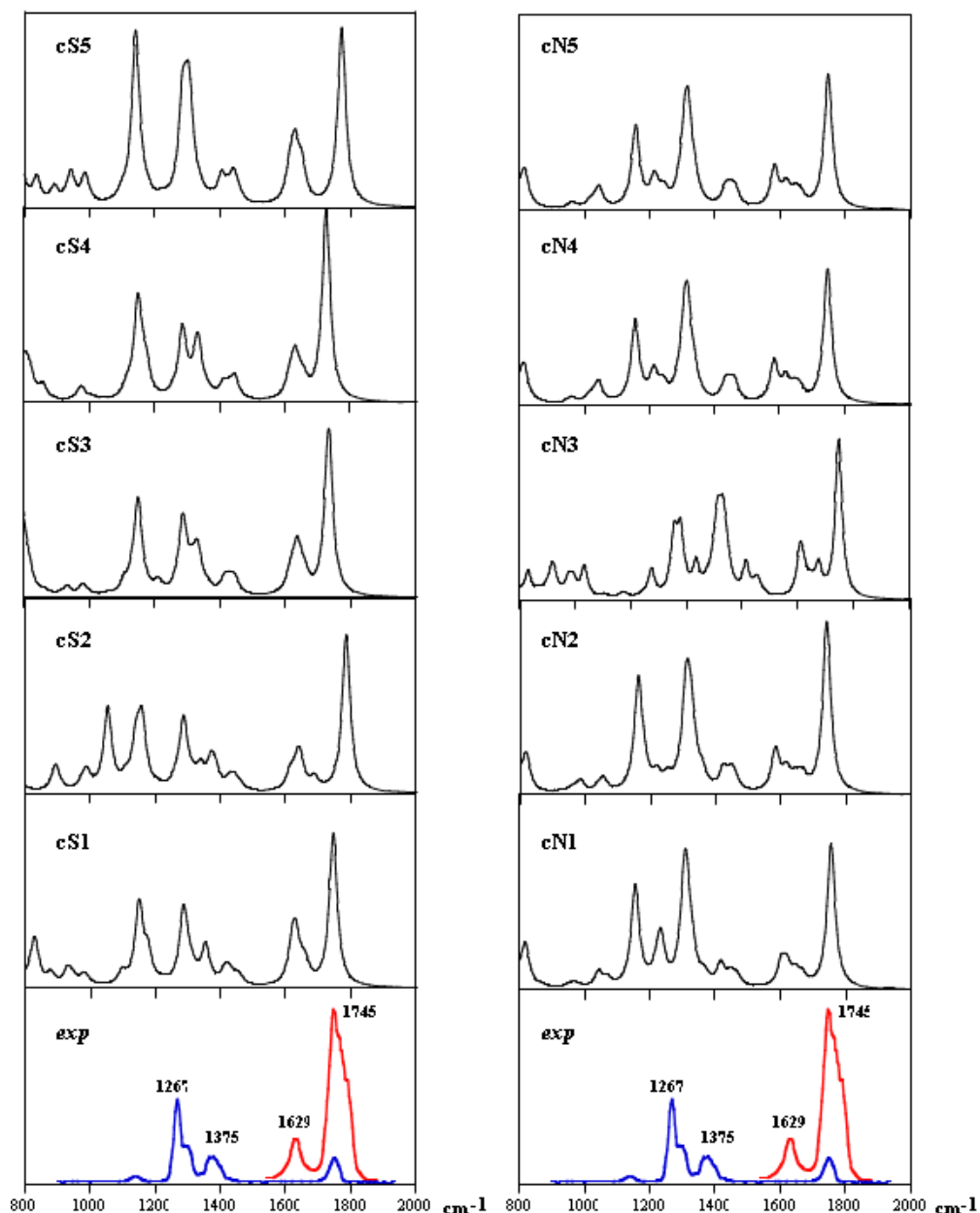


**Figure 2** Experimental IRMPD spectrum (exp) of *cis*-[PtCl(NH<sub>3</sub>)<sub>2</sub>(Met)]<sup>+</sup> compared to calculated IR spectra (black lines) according to B3LYP/6-31G\* frequency computations in the spectral range of 800–2000 cm<sup>-1</sup>. Comparison for cS and cN first five plausible isomers.

Examination of both profiles of Figure 2 shows that the most informative IR resonances for *cis*-[PtCl(NH<sub>3</sub>)<sub>2</sub>(Met)]<sup>+</sup> are the C=O stretching at 1745 cm<sup>-1</sup>, the NH<sub>2</sub> scissoring at 1629 cm<sup>-1</sup>, the umbrella bending mode of the NH<sub>3</sub> group at 1375 cm<sup>-1</sup> and, finally, the band at 1267 cm<sup>-1</sup> assigned the C—OH bending. Overall, the experimental resonances are well matched by the computed spectra of the *cis*-[PtCl(NH<sub>3</sub>)<sub>2</sub>(Met-S)]<sup>+</sup> isomers (Structures **cS1-5** in the Figure 1). The low wavenumber region of the spectrum

(1000-1500  $\text{cm}^{-1}$ ), appears particularly revealing, with an overall better agreement between the experimental and the linear IR spectrum of the sulfur-chelating species **cS1**, as compared to the other sulfur binding conformers (**cS2-cS5**).

Figure 3 displays the optimized structures of the most stable conformer for plausible *trans*-[PtCl(NH<sub>3</sub>)<sub>2</sub>(Met)]<sup>+</sup> isomers as obtained at the B3LYP/6-31g\* level of theory.

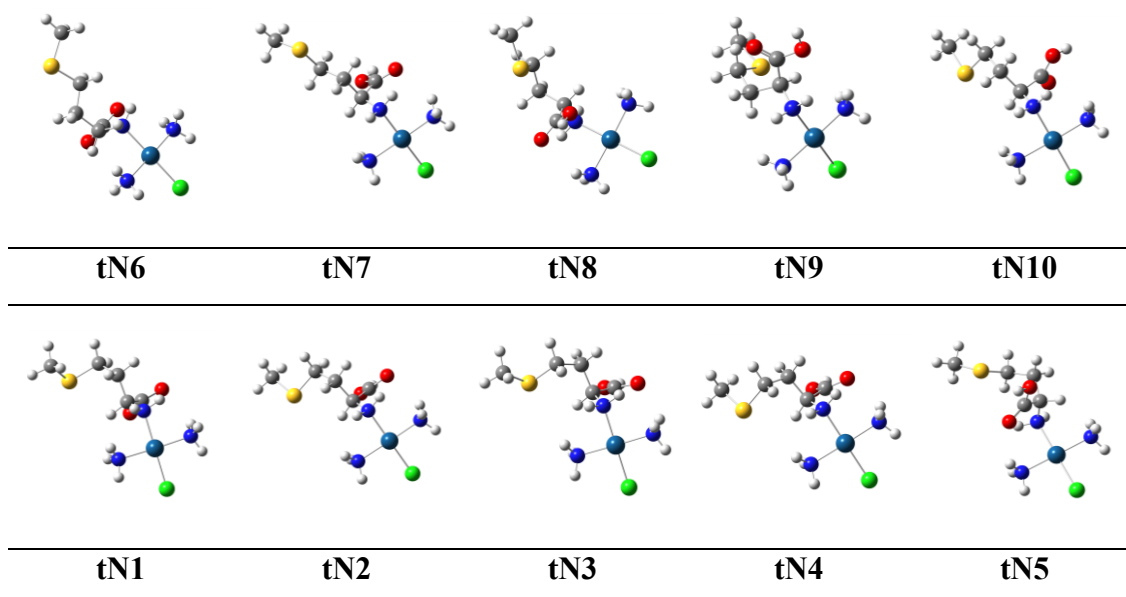


**Figure 3.** Optimized structures of the first five conformers of general formula *trans*-[PtCl(NH<sub>3</sub>)<sub>2</sub>(Met-N)]<sup>+</sup>.

When the *trans*-[PtCl(NH<sub>3</sub>)<sub>2</sub>(Met)]<sup>+</sup> (*m/z* 412) complex was investigated, we obtained an IRMPD spectrum of the isomer, as showed in the Figure 4. It presents three prominent bands at 1125, 1275 and 1746  $\text{cm}^{-1}$ , along with several minor absorptions at 941, 1371, 1416 and 1591  $\text{cm}^{-1}$ .



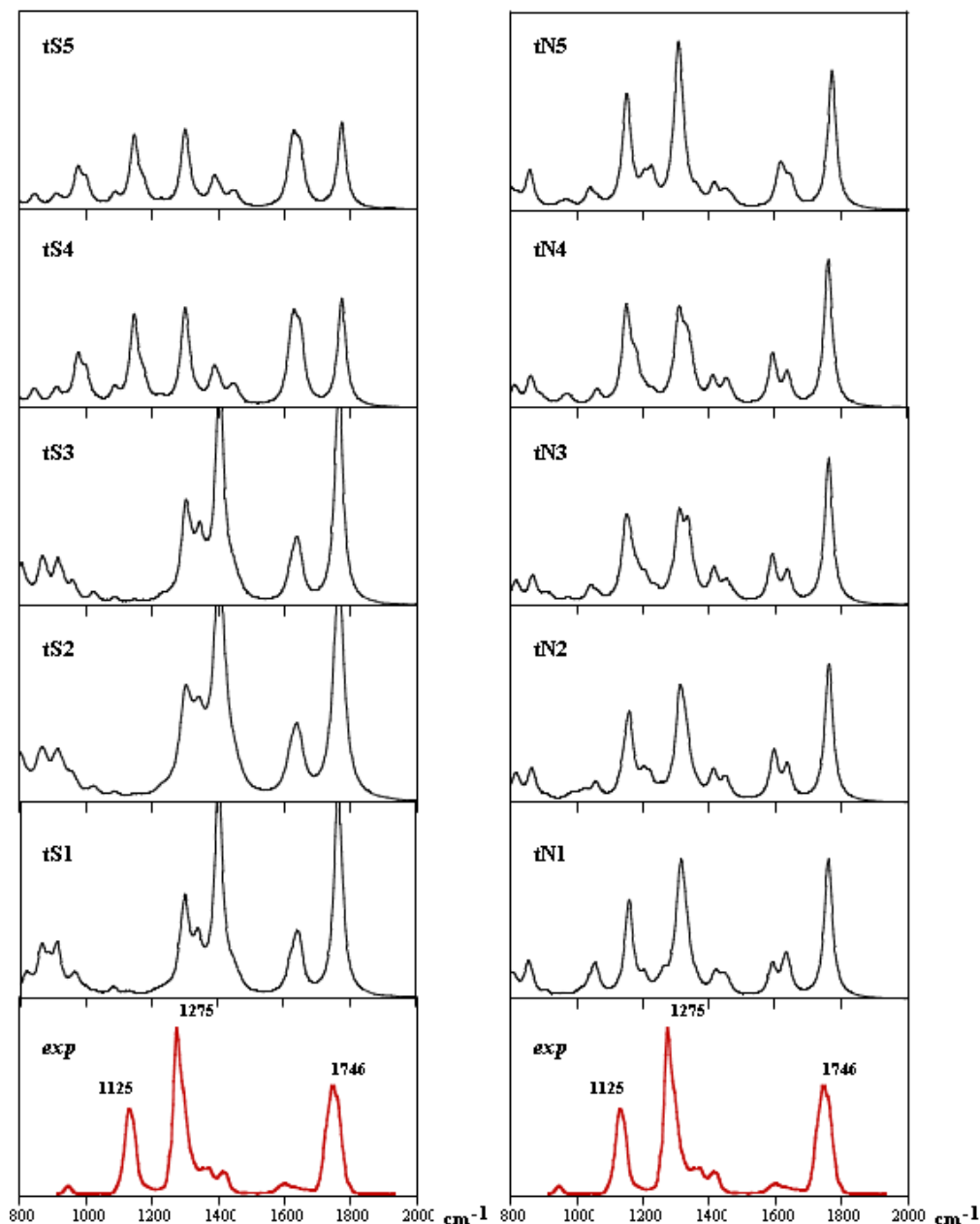


**Figure 4.** Experimental IRMPD spectrum (*exp*) of *trans*-[PtCl(NH<sub>3</sub>)<sub>2</sub>(Met)]<sup>+</sup> compared to calculated IR spectra (black lines) according to B3LYP/6-31G\* frequency computations in the spectral range of 800–2000 cm<sup>-1</sup>. Comparison for tS and tN first five plausible isomers.

Examination of Figure 4 shows that the IR signatures of the most stable *trans*-[PtCl(NH<sub>3</sub>)<sub>2</sub>(Met-N)]<sup>+</sup> conformer are in good agreement with the experimental spectrum. In the bunch of ten computed spectra (black lines), the nitrogen chelating complexes seem to better reproduce the band of NH<sub>2</sub> scissoring in the experimental *trans* spectra. Note that the direct binding of Pt(II) to the nitrogen, in the *trans* complex cause the red-shift of the NH<sub>2</sub> scissoring at 1600 cm<sup>-1</sup>, with respect to the absorption at 1629 cm<sup>-1</sup> in the *cis* isomer.

The IR linear spectra obtained from conformers **tN1** and **tN2** faithfully reproduces the experimental signatures. The main feature at  $1275\text{ cm}^{-1}$  can be assigned to the C-OH stretching mode of **tN** complexes, where they appear slightly overestimated. The absorption at  $1746\text{ cm}^{-1}$  corresponds to the C=O stretching mode calculated with a blue-shift of ca  $10\text{ cm}^{-1}$  in each conformer. Finally the bands at  $1125\text{ cm}^{-1}$  are consistent with the C-N stretching calculated with a perfect agreement.

Comparing the experimental spectra depicted in Figures 2 and 4, the most evident differences between the *cis* and *trans* isomers are in the two signatures for the NH<sub>2</sub> scissoring and C—N stretching respectively. The NH<sub>2</sub> scissoring appears at  $1629\text{ cm}^{-1}$  in the *cis*- isomer (red profile in Figure 2) while at  $1600\text{ cm}^{-1}$  in the *trans*- isomer (Figure 4). The intense C-N stretching mode at  $1125\text{ cm}^{-1}$ , registered for the *trans*- isomer, does conversely results as a minor band in the the spectrum of *cis*- isomer (Figure 2). Interestingly, it is worthy to note that the C=O stretching mode is red-shifted in both the *cis* and *trans*-[PtCl(NH<sub>3</sub>)<sub>2</sub>(Met)]<sup>+</sup> complexes with respect to a free C=O stretching vibration, expected at ca.  $1800\text{ cm}^{-1}$ . This effect can be due to an hydrogen bond interaction that involves the carbonyl group so lowering its double bond character.

An inversion of the first chelating site of methionine to platinum(II) in *cis*- and *trans*- [PtCl(NH<sub>3</sub>)<sub>2</sub>(Met-N)]<sup>+</sup> cannot be excluded, when a neutral molecule of methionine reacts in solution with the two different charged intermediate *cis*- and *trans*- [PtCl(NH<sub>3</sub>)<sub>2</sub>(H<sub>2</sub>O)]<sup>+</sup> formed by aquation (Scheme 1). In a previously work, Zimmermann et al. demonstrated the peculiar stability of the *trans*-[PtCl(NH<sub>3</sub>)<sub>2</sub>(Met-N)]<sup>+</sup> in solution. The nitrogen is the most preferred amino acid donor and the [PtCl(NH<sub>3</sub>)<sub>2</sub>Met-N]<sup>+</sup> complexes is the most stable. However, the **cS** monodentate complex seems to dominate in a large range (2.5 - 9.7) of pH, confirming the pH dependent migration of a platinum between S and N donor atom. The nitrogen donor is preferred at pH value greater than 9.7. Our mid-infrared ( $800\text{-}2000\text{ cm}^{-1}$ ) assay of bare *cis*- and *trans*-[PtCl(NH<sub>3</sub>)<sub>2</sub>(Met)]<sup>+</sup> ions, complemented by a theoretical investigation based on DFT method, confirms that competition between S or N chelating agents is a key step in the formation of the most stable final products of the reactions with methionine. As a whole, sulphur chelating mechanism seems to guide the complex formation in the reaction between *cis*-

$[\text{PtCl}(\text{NH}_3)_2(\text{H}_2\text{O})]^+$  and L-methionine, at contrary with the *trans*- isomer, where the water replacing mechanism seem to take place with the nitrogen atom.

The *cis* and *trans*- $[\text{PtCl}(\text{NH}_3)_2(\text{Met})]^+$  ions ( $m/z$  412) have also been investigated in the range from 2900 to 3600  $\text{cm}^{-1}$ . Numerous resonances are present in the spectra (red lines) shown in Figure 5.

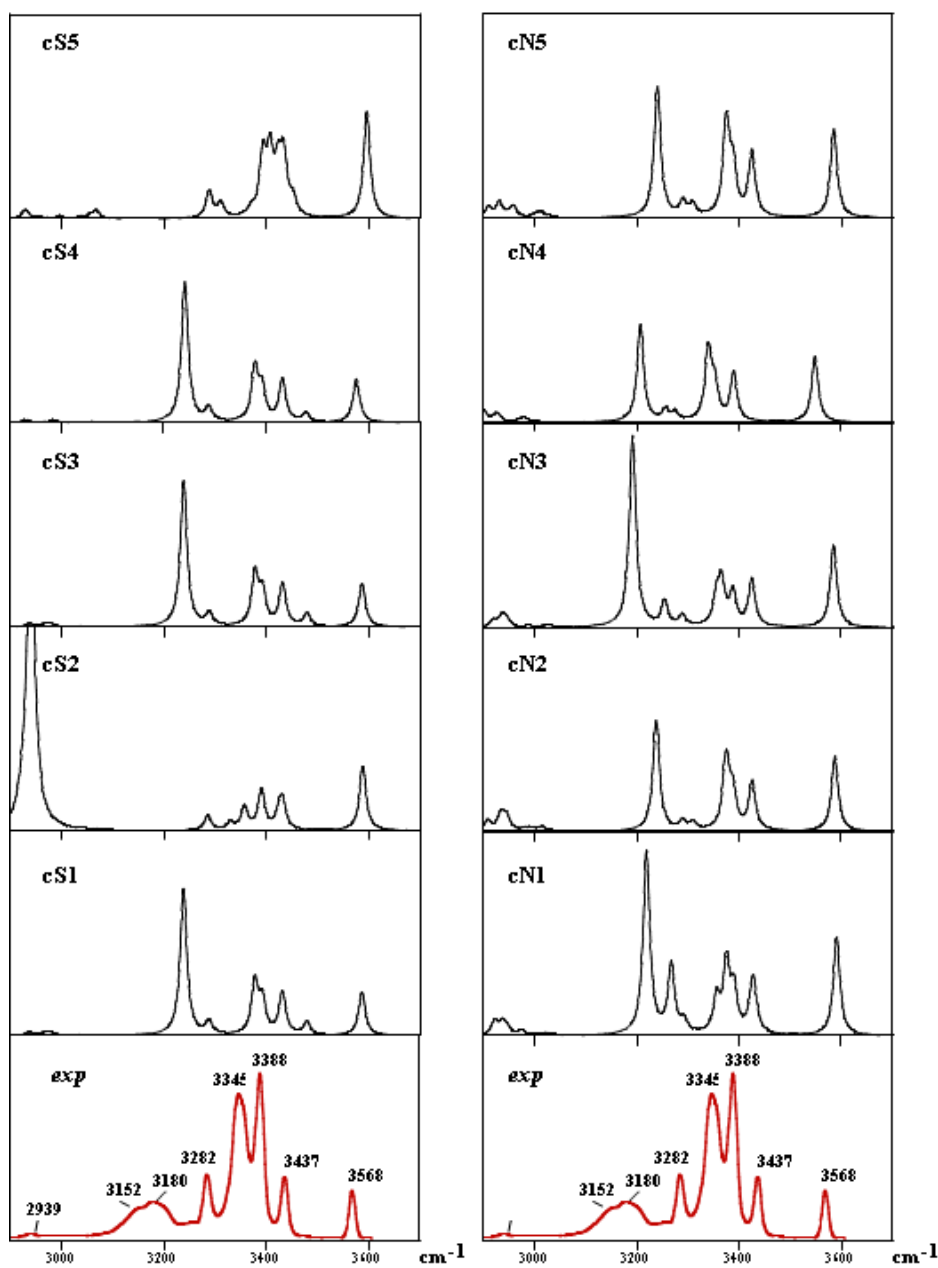


**Figure 5.** Experimental IRMPD spectrum (*exp*) of *cis*- $[\text{PtCl}(\text{NH}_3)_2(\text{Met})]^+$  compared to calculated IR spectra (black lines) according to B3LYP/6-31G\* frequency computations in the spectral range of 2900–3700  $\text{cm}^{-1}$ . Comparison for cS and cN first five plausible isomers.

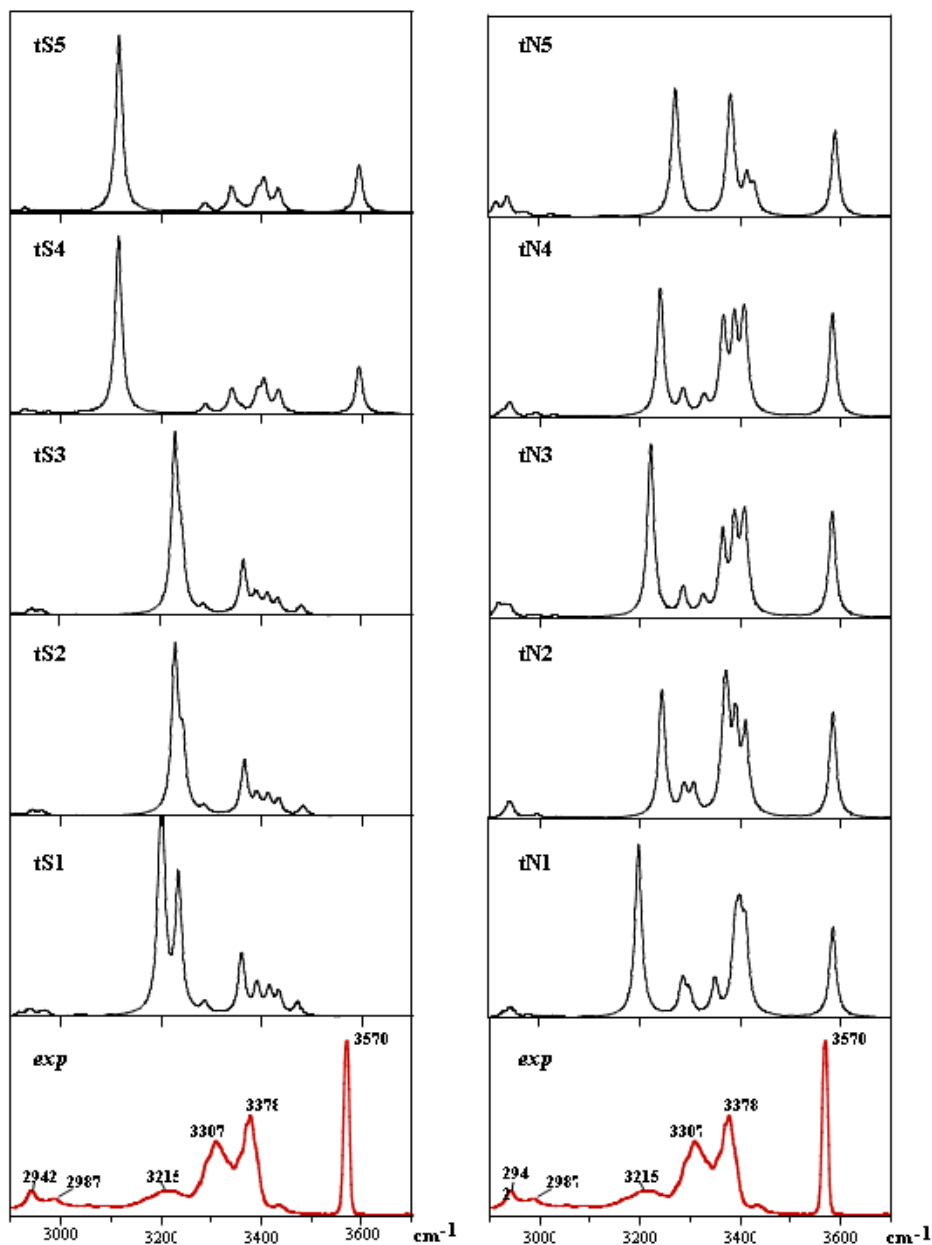


**Figure 6.** Experimental IRMPD spectrum (*exp*) of  $trans\text{-}[\text{PtCl}(\text{NH}_3)_2(\text{Met})]^+$  compared to calculated IR spectra (black lines) according to B3LYP/6-31G\* frequency computations in the spectral range of 2900–3700  $\text{cm}^{-1}$ . Comparison for tS and tN first five plausible isomers.

Most of the information that is used to interpret an IRMPD spectrum is obtained from the functional group region, where several N—H and O—H hydrogen stretching modes give rise to the high IR activity of the ions of interest. It is evident that both complexes exhibit similar spectral features. For the sake of comparison, Figures 5-6 report also the IR spectra of the corresponding most stable Met-S (left) and Met-N (right) platinum conformers calculated at the b3lyp/6-31g\* level of theory. In the *cis* complex

(Figure 5, red lines), five relatively narrow IR bands are observed in the 3200-3600  $\text{cm}^{-1}$  spectral range, 3282, 3345, 3388, 3437 and 3568  $\text{cm}^{-1}$ . Each resonance is reproduced quite well by the **cS** conformers, especially in the N—H region. The broad bands at 3152 and 3180  $\text{cm}^{-1}$  are always accompanied by a narrower and distinct shoulder on the blue side on theoretical spectra of Met-S platinum conformers. This broad absorption around 3160  $\text{cm}^{-1}$  may be assigned to the NH stretching of the N—H bond involved in hydrogen-bonding with the carbonyl oxygen of methionine. Nevertheless, the experimental bands are much weaker than the corresponding calculated modes when involved in hydrogen bonding. It is by now undisputed that the broadening and red-shift effect have been observed<sup>11-13</sup> in the hydrogen bond NH and OH stretches, and this can account for the broad structures below 3200  $\text{cm}^{-1}$ . Conformers **cS1**, **cS3** and **cS4**, where hydrogen bonding has been predicted, well reproduce the main features of the experimental spectrum (Figure 5). Furthermore it is not possible to exclude the effect of the N—H stretching mode, registered at 3180  $\text{cm}^{-1}$  (red line) and calculated at 3200  $\text{cm}^{-1}$  (**cN3**), on the weak and broad active mode revealed in the IRMPD spectra for N—H stretching. In agreement with previous work, this is an example of NH vibration involved in hydrogen bonding revealed by IRMPD spectroscopy, in the gas-phase, as already observed<sup>14</sup>. It would be very interesting to note that the experimental spectrum of *cis* isomer shows one signature at 3437  $\text{cm}^{-1}$  that does not find a counterpart in the IRMPD spectrum of *trans* isomer (Figure 3a, red lines), where no N—H stretching modes above 3378  $\text{cm}^{-1}$  have been observed. This has been theoretically confirmed by the calculated spectra of *trans*-[PtCl(NH<sub>3</sub>)<sub>2</sub>(Met-N)]<sup>+</sup> ions (Figure 6, black lines). The pattern of O—H and N—H hydrogen bonded stretching modes, at 3570 and 3215  $\text{cm}^{-1}$ , respectively, is well reproduced by the nitrogen chelating complexes (**tN**).

### 3.4. Conclusions

The purpose of this study was to carry out a structural characterization of the monofunctional adduct between cisplatin and transplatin with L-methionine, using IRMPD spectroscopy of gaseous ions directly performed in the cell of a mass spectrometer. Both the IR characterization and the computational results point to a non-uniform mode of interaction of the amino acid with platinum drugs. The chelating action by methionine depends on the initial structures of the hydrated species<sup>15</sup>. The *cis*-[Pt(NH<sub>3</sub>)<sub>2</sub>(Met)]<sup>+</sup> complex seems to be characterized by a sulphur bridge, where Pt is bound to the S atom of methionine. This is evident both in the CLIO and in the OPO regions. Signatures for *cis*-complex, like the umbrella mode of NH<sub>2</sub> and the C-OH stretching (1375 and 1267 cm<sup>-1</sup> respectively) and the N—H stretching (3200-3400 cm<sup>-1</sup>), can be easily assigned to the computed conformers of the **cS** family. Spectra of the conformers **cS1** and **cS3**, in both infrared regions, are well consistent with the experimental ones. Conversely, in *trans*-hydrated species L-methionine prefers to coordinate Pt(II) via the nitrogen atom. This assumption confirms the results already obtained for these species in solution<sup>2</sup>. This features may open the way toward a better understanding of the toxicity and bioavailability of this drug.

### 3.5. References

- (1) Vrana, O.; Brabec, V. L-methionine inhibits reaction of DNA with Anticancer *cis*-diamminedichloroplatinum(II) *Biochemistry* **2002**, 41, 10994-10999.
- (2) Zimmermann, T.; Burda, J. V. Cisplatin Interaction with Amino Acids Cysteine and Methionine from Gas-Phase to Solutions with Constant pH *Int. Sciences* **2010**, 2, 98-114.
- (3) Zimmermann, T.; Burda, J. V. Reactions of Cisplatin with Cysteine and Methionine at Constant pH; a Computational Study *Dalt Trans.* **2010**, 39, 1295-1301.
- (4) Reedijk, J. Why does Cisplatin reach Guanine-n7 with Competing s-Donor Ligands Available in the Cell *Chem. Rev.* **1999**, 99, 2499-2510.
- (5) Poirson-Bichat, F.; Goncalves, R. A.; Miccoli, L.; Dutrillaux, B.; Poupon, M. F. Methionine Depletion Enhances the Antitumoral Efficacy of Cytotoxic Agents in Drug-Resistant Human Tumor Xenografts *J. Am. Ass. for Cancer Research* **2000**, 6, 643-653.
- (6) Lau, J. K.; Deubel, D. V. Loss of Amine from Platinum(II) Complexes: Implications for Cisplatin Inactivation, storage, and resistance *Chemistry* **2005**, 11, 2849-2855.
- (7) Zimmermann, T.; Zeizinger, M.; Burda, J. V. Cisplatin Interaction with Cysteine and Methionine, a Theoretical DFT Study *J. of Inorg. Bioch.* **2005**, 99, 2184-2196.
- (8) Frey, U.; Ranford, J. D.; Sadler, P. Hydrogen-bonding in Mononucleotide and Polynucleotide Adducts of Platinum Anticancer Complexes in Aqueous Solution *J. Inorg. Chem.* **1993**, 32, 1333-1340.
- (9) van Boom, S. S. G. E.; Chen, B. W.; Teuben, J. M.; Reedijk, J. Platinum-thioether Bonds can be Reverted by Guanine-N7 Bonds in Pt(dien)(2+) Model Adducts *J. Inorg. Chem.* **1999**, 38, 1450-1455.
- (10) Zimmermann, T.; Chval, Z.; Burda, J. V. Cisplatin Interaction with Cysteine and Methionine in Aqueous Solution: Computational DFT/PCM Study *J. Phys. Chem. B* **2009**, 113, 3139-3150.
- (11) Kamariotis, A.; Boyarkin, O. V.; Mercier, S. R.; Beck, R. D.; Bush, M. F.; Williams, E. R.; Rizzo, T. R. Infrared Spectroscopy of Hydrated Amino Acids in the Gas-Phase: Protonated and Lithiated Valine *J. Am. Chem. Soc.* **2006**, 128, 905-916.
- (12) Bakker, J. M.; Sinha, R. K.; Besson, T.; Brugnara, M.; Tosi, P.; Salpin, J. Y.; Maitre, P. Tautomerism of Uracil Probed via Infrared Spectroscopy of Singly Hydrated Protonated Uracil *J. Phys. Chem. A* **2008**, 112, 12393-12400.
- (13) Scuderi, D.; Le Barbu-Debus, K.; Zehnacker, A. The role of Weak Hydrogen Bonds in Chiral Recognition *Phys. Chem. Chem. Phys.* **2011**, 13, 17916-17929.
- (14) Chiavarino, B.; Crestoni, M. E.; Fornarini, S.; Scuderi, D.; Salpin, J.-Y. Interaction of Cisplatin with Adenine and Guanine: A Combined IRMPD, MS/MS, and Theoretical Study *J. of Am. Chem. Soc.* **2012**, 135, 1445.
- (15) De Petris, A.; Ciavardini, A.; Coletti, C.; Re, N.; Chiavarino, B.; Crestoni, M. E.; Fornarini, S. Vibrational Signatures of the Naked Aqua Complexes from Platinum(II) Anticancer Drugs *J. of Phys. Chem. Letters* **2013**, 4, 3631-3635.





## CHAPTER 4

# **Binding interactions in heme-azole complexes: combined application of energy-resolved collision-induced dissociation and Car-Parrinello molecular dynamics calculations**

#### 4.1. Introduction

Fungal infections are a continuous and serious threat to human health and life. Different kinds of mycoses, especially invasive and resistant<sup>1</sup>, have become an important public health problem as their incidences has increased dramatically in the last decades<sup>2</sup>. Management of fungal infections is markedly limited by problems of drug safety, resistance and bioavailability. Moreover fungi rarely cause disease in healthy immunocompetent hosts. Disease results when fungi accidentally penetrate host barriers or when immunologic defects or other debilitating conditions exist that favor fungal entry and growth. Thus, the main factor for the propagation of fungal infections is the growth in the population of immune-compromised patients either with AIDS, or undergoing cancer chemotherapy, or immunosopressive therapy<sup>3,4</sup>. Additional factors include treatment with broad-spectrum antibacterial drugs or glucocorticosteroids.

The P450 sterol 14 $\alpha$ -demethylase enzyme, normally called CYP51, is an important target in fungal infections. Inhibition of CYP51 by drugs containing the azole group does result in a decreased ergosterol synthesis, the principal component of the fungal cell membrane. Azole containing drug which act as inhibitors were shown to coordinate tightly to CYP51 from the bacterium and to inhibit mycobacterial growth. They prevent the 14- $\alpha$  demethylation of lanosterol into ergosterol in the ergosterol synthetic pathway<sup>5</sup>. The active site of the CYP51 enzymes contains a central heme moiety as the prostetic group linked to the binding site environment<sup>6</sup>. Azole inhibitors occupy one of the proximal axial ligand position of iron rendering it inactive to oxygen chemistry. There are several reversible inhibitors with azole functional group that target the P450 sterol 14 $\alpha$ -demethylase<sup>7</sup>. Any azole drug contains an imidazole or a triazole functional group that is expected to bind the iron center.

In the biological fields, azole drugs were extensively studied in the inhibition of CaCYP51 (*Candida albicans* 14 $\alpha$ -demethylase) and HsCYP51 (Homo Sapiens CYP51). UV-vis ligand binding and CO displacement studies have been used in tandem to provide screening mechanisms for *in silico* design of new antifungal drugs of therapeutic interest; Vanden Bossche et al. reported IC<sub>50</sub> values for a variety of azole inhibitors using membranes isolated form *C. albicans*<sup>8</sup>; Warrilow et al. characterized azole binding properties with CaCYP51 and HsCYP51, contributing to a large screening of new

therapeutic azole antifungal agents. Inhibition of HsCYP51 may also results in endocrine disruption since follicular fluid-meiosis activating steroid (FF-MAS), the first product of lanosterol demethylation, is involved in the control of meiosis. Starting from this assumption and monitoring the FF-MAS product formation by LC-MS/MS analysis could provide an alternative tool to measure the biological activity of antifungal agents. In 2006 Lutz et al. established a comparison of inhibitory potencies of azole compounds toward human and fungal CYP51 using an LC-MS/MS analysis. In this work, fluconazole and itraconazole, belonging to the family of triazole-like drugs, showed the lowest IC<sub>50</sub> values against *Candida albicans* CYP51 (Table 1)<sup>9</sup>, while imidazole-like drugs such as ketoconazole, bifonazole and miconazole were listed as the weaker inhibitors. The inhibitory potencies of azole fungicides on human CYP51 (IC<sub>50</sub> HsCYP51) showed a wider range of activity from 0.43 μM to 30.0 μM. Miconazole was the most potent of all azoles tested (Table 1). Three of the six antifungal drugs (miconazole, bifonazole and ketoconazole) were more potent than the most potent fungicide (bitertanol). These are all imidazole compounds and are the older compounds on the market compared to the two newer triazole compounds, fluconazole and itraconazole.

<b>Drug</b>	<b>IC<sub>50</sub> CaCYP51</b>	<b>IC<sub>50</sub> HsCYP51</b>
Bifonazole	0.30	0.80
Fluconazole	0.051	>30
Itraconazole	0.039	≈30
Ketoconazole	0.064	0.43
Miconazole	0.072	0.057

All data are in μM (data are from ref 24).

**Table 1.** Comparison of IC<sub>50</sub> Values for *Candida albicans* (CaCYP51) and Human CYP51 (HsCYP51).

The binding of azole antifungal agents to P450s has been extensively studied. As early as 1967, Estabrook et al.<sup>10</sup> reported type-II spectral shifts arising from the binding of nitrogen-containing compounds, such as pyridine and nicotine, to human liver P450s. Van den Bossche postulated that the target of the azole antifungal drugs is the CYP51<sup>7</sup>. Schuster studied the effect of azoles on human P450s, concluding that the metabolism of xenobiotic substrates by the P-450 of liver should be severely impeded by azole drugs<sup>11</sup>.

Since then, there have been innumerable reports on the binding of azole antifungals to CYP51 and human P450s, including many studies on drug-drug interactions involving azole binding to CYP3A4<sup>12-14</sup> and a number of studies on the binding of azole antifungals to *Mycobacterium tuberculosis* (Mtb) P450s<sup>15-17</sup>. The first crystal structures of azole bound P450s were obtained for the fluconazole and phenylimidazole complexes of Mtb CYP51B1<sup>18,19</sup>, and these complexes showed a nitrogen atom coordinated to the heme iron. The inhibitors bind directly to the iron and form an Fe-N bond. Crystal structures have been also solved for the ketoconazole complex with human P450s<sup>20</sup> and the ligand free state of the CYP51 from *Trypanosoma brucei*<sup>21</sup>. Rupp et al. tried to explain the enantioselectivity of the ketoconazole binding mode by using molecular dynamics simulation and parameterizing the iron azole binding complex with the help of Density Functional Theory (DFT)<sup>22</sup>. Further DFT calculations on inhibitor binding to the active site of P450 enzymes have been carried out by Balding et al.<sup>23</sup>. In the former study only theoretical relative binding energies of methylimidazole, methyltriazole and pyridine with heme were investigated, no further drugs were tested. On an experimental perspective, mass spectrometry is potentially suitable to ascertain the binding features in metal ion complexes sampled in an isolated state. For example, Ryzhov et al. used energy-variable collision-induced dissociation (CID) to determine the relative gas-phase binding strength of square pyramidal and octahedral Co(III) complexes of porphyrins, chlorins and porphyrin analogues to the first and second axially bound imidazoles, thus revealing that positive ion mode electrospray ionization(ESI)-MS is a premier technique to probe electronic and structural properties<sup>24</sup>. However, there are no experimental evidences on the naked relative binding properties of azole compounds with the prostetic group of CYP51, that could support the theoretical data.

Electrospray ionization (ESI) is a soft ionization method that allows to obtain intact gas-phase ions with minimal fragmentation during the ionization process. Thus, studies of gas-phase thermochemical properties of ionic species originating from solution are quite accessible by ESI-MS. Indeed, some aspects of the gas-phase studies need to be consistent with the solution-phase world in order for the ESI-MS experiments to have some utility for medicinal chemistry. An indication that solution-phase binding events are indeed being correctly monitored in the gas-phase derives from ESI-MS reports on the determination of the relative and absolute strength of solution-phase interactions<sup>25-27</sup>.

Actually the gas-phase represents a unique medium to investigate the association reaction of various ligands to bare heme complexes. Using the ESI source, mid and large size ions may be analyzed in the absence of any solvent or matrix that could alter the intrinsic properties of the naked complexes. As gas-phase binding assays provide a means to characterize the inherent affinity ofazole compounds (Figure 1) to Fe(III)-protoporphyrin IX ( $\text{Fe}^{\text{III}}(\text{PPIX})^+$ ), they may play an important role in the drug discovery process. Energetic gas-phase collisions with atoms or molecules is a physical process used in mass spectrometry to increase the internal energy of the ion of interest up to the dissociation threshold. In the present study, the term ‘internal energy’ refers to the (final) total internal energy distribution of the collisionally activated ion population. Under equilibrium condition, the internal energy of the selected ion population obtained by ESI-MS is assumed to have a Maxwell–Boltzmann distribution<sup>28</sup>. However, control experiments are necessary to rule out ubiquitous nonspecific interactions (i.e., heme aggregated complexes) and caution needs to be exercised each time when interpreting data from such ESI-MS experiments<sup>29</sup>.

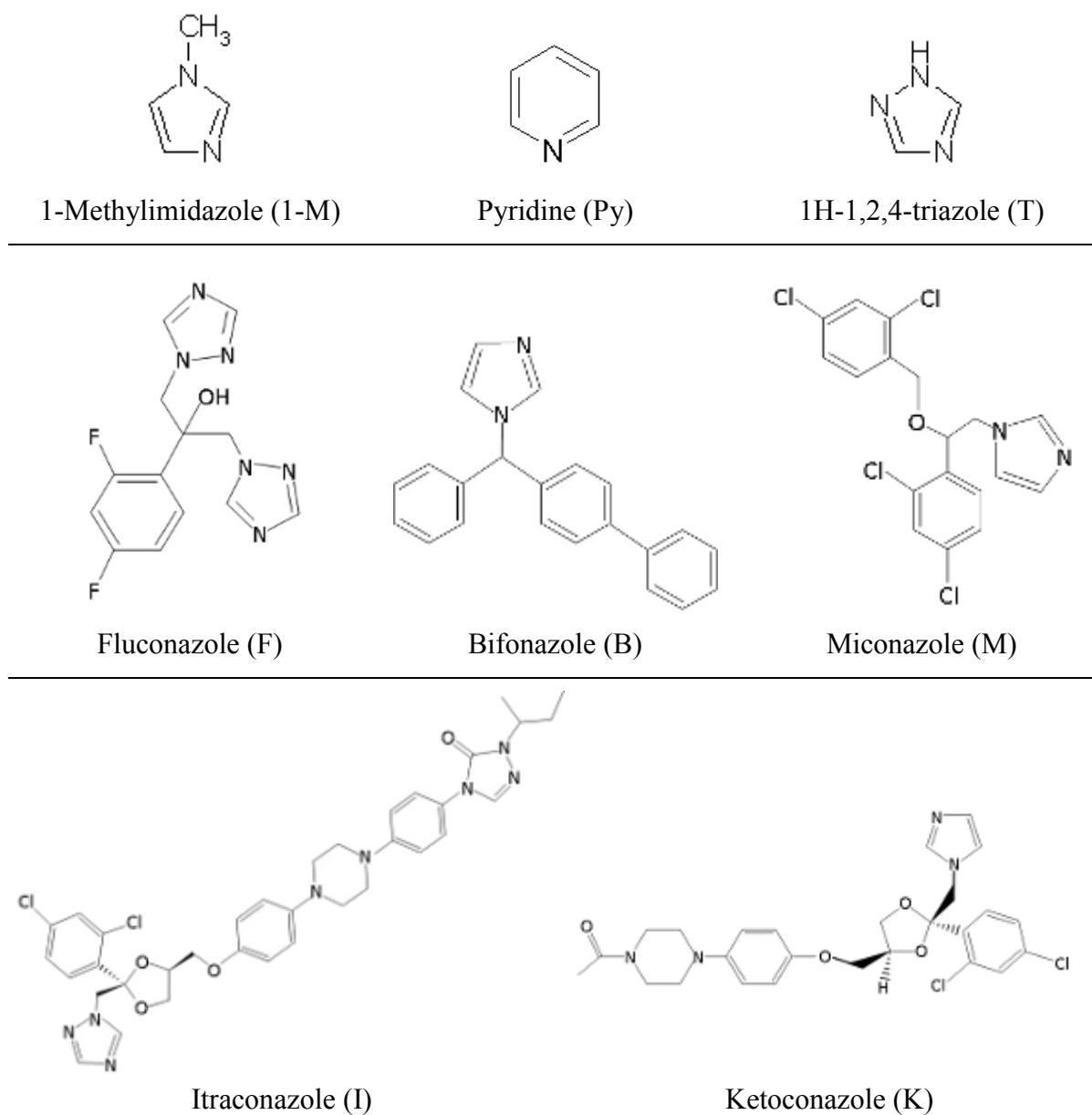


**Figure 1.** Azole Ligands of Fe(III)-protoporphyrin IX, as studied in this work.

In this context, a better understanding at the molecular level of the interactions between iron in the heme complex and azole ligands is expected to be helpful in establishing a new strategy to design/develop new antifungal analogues. In the present study, we have undertaken a gas-phase investigation aiming at evaluating experimental bond dissociation energies of eight different heme-azole complexes. Working in the gas-

phase offers the advantage that dissociation reactions yield direct informations on the intrinsic reactivity of cations.

The assay, performed with a commercial hybrid triple-quadrupole linear ion trap mass spectrometer (Q1q2Q<sub>LIT</sub>), is based on three sequential steps: i) incubation of the methanol solution containing theazole ligand (L) mixed with hemin chloride; ii) selection of the electrosprayed  $[\text{Fe}^{\text{III}}(\text{PPIX})\text{L}]^+$  complex using Q1; iii) collision with N<sub>2</sub> in the quadrupole collision cell q2 at variable collision energies for CID. In order to gain insight into the interaction mode, and into how strongly azoles bind bare  $\text{Fe}^{\text{III}}(\text{PPIX})^+$ , CID experiments were theoretically supported using a Car-Parrinello Molecular Dynamics (CPMD). The relation between the internal energy content and the isomeric and conformational landscape of the sampled ion population is an additional reason for the growing interest in energy dependence studies of ionized biomolecules. Interestingly, it has previously been shown that gas-phase activation and dissociation studies on isolated/trapped macromolecular ions allow us to relate bond energies evaluated in the gas-phase with structural/conformational patterns in solution<sup>30</sup>.

## 4.2. Experimental Section

### 4.2.1. Materials.

Hemin Chloride, 1-Methylimidazole, 1H-1,2,4-Triazole, Methanol and Ammonia used in this work were supplied from commercial source (Sigma-Aldrich, Milan, Italy) and used without further purification. Fluconazole, Miconazole, Itraconazole, Bifonazole and Ketoconazole were extracted and purified from commercial drugs (respectively Diflucan®, Daktarin®, Sporanox®, Canesten® and Nizoral®) according to acid-base extraction procedures described in the literature<sup>31</sup>. Stock solutions of hemin chloride and of eachazole were prepared at millimolar concentration in methanol and then mixed in a 1: 1 molar ratio in methanol so reaching a final concentration of 5  $\mu\text{M}$ .

#### 4.2.2. CID Experiments.

The sampled ions were generated in the gas-phase by directly infusing a  $1 \times 10^{-5}$  M methanol solution of  $[\text{Fe}^{\text{III}}(\text{PPIX})]\text{Cl}$  and Azole through a fused –silica capillary to the ESI source by a syringe pump at a typical flow rate of  $10 \mu\text{L min}^{-1}$ . Typical values of declustering potential and entrance potential were set to 40 and 5 V, respectively. Collision-induced dissociation (CID) experiments at variable energy were carried out using an Applied Biosystems 2000 Q-Trap instrument, a commercial hybrid triple-quadrupole linear ion trap mass spectrometer (Q1q2Q<sub>LIT</sub>). The ion of interest was mass-selected using Q1. CID experiments were performed in the quadrupole collision cell q2 at variable collision energies ( $E_{\text{lab}} = 5\text{-}50$  eV) with  $\text{N}_2$  as collision gas at a nominal pressure of  $5.4 \times 10^{-5}$  torr. The dissociation product pattern was monitored by scanning Q<sub>LIT</sub> by using the enhanced mode of operation where the ions, formed in q2, are trapped in Q<sub>LIT</sub> for 35 accumulation spectra in order to increase both resolution and intensity. At  $E_{\text{lab}} = 0$  eV, no significant fragmentation of mass-selected  $[\text{Fe}^{\text{III}}(\text{PPIX})\text{L}]^+$  ions was observed. Notably, for weakly bound complex ions, a non-negligible amount of ion decay has been previously observed even at  $E_{\text{lab}} = 0$  eV, which is in part attributed to the presence of collision gas not only in the quadrupole, but also in the focusing regions between the mass analyzers<sup>32-34</sup>. This explanation is supported by the pressure dependence of the relative fraction of ions<sup>35,36</sup>.

The instrumental response was initially tuned for the  $[\text{Fe}^{\text{III}}(\text{PPIX}) (1\text{-Methylimidazole})]^+$  complex and the selected conditions were used for all subsequent analyses. For energy-resolved CID, the phenomenological appearance energies ( $E_{\text{PT}}$ ) were measured while scanning the quadrupole offset. Ion peak intensities were found considerably higher when the detector quadrupole was operated in “*enhanced product ion*” (EPI) mode as compared to the more conventional “*product ion*” (PI) mode. The former mode was therefore used for the whole set of measurements performed in this report. In EPI mode, after fragmentation in q2 region, the fragment ion is captured and then scanned with an enhanced scan speed, this means that the elimination of the precursor ion can be easily observed<sup>37</sup>.

The collision-energy dependent CID mass spectra have been measured in at least three independent experiments performed on different days in order to eliminate any



possible systematic error. In a single experiment, each experimental point is obtained as an average of 35 spectra, in order to obtain a better signal to noise ratio. In order to avoid a possible effect of the kinetic energy resolution on the relative binding energies of  $[\text{Fe}^{\text{III}}(\text{PPIX})\text{L}]^+$ , the experimental conditions were kept as much reproducible as possible. The same holds true for possible effects of the internal energy content of the parent ions generated in the ESI source. Variation of the collision energy, converted to the center of mass frame  $\text{ECM} = E_{\text{lab}} \times [m / (m + M)]$ , (where  $m$  and  $M$  are the masses of the collision gas and of the ion, respectively) led to the breakdown curves that allowed the extrapolation of phenomenological appearance energies ( $E_{\text{PT}}$ ) of the various fragmentation channels. The conversion satisfies the equation where  $E_{\text{lab}} = (\text{CE} + \text{EP} - \text{Nominal Zero})$ , where CE represent the instrumental collision energy, EP is the voltage between the skimmer (ground) and the entrance to Q0. Regarding the Nominal Zero correction, full details will be given in the paragraph 4.3.1.

#### 4.2.3. Computational Details.

The calculations were performed using the Car-Parrinello molecular dynamics method<sup>38</sup>, which is based on Density Functional Theory (DFT). Previous work has demonstrated the reliability of this method in the description of structural, energetic and dynamical properties of systems of biological interest<sup>39</sup>. In the present application, Kohn–Sham orbitals are expanded in a plane wave basis set with the kinetic energy cutoff of 70 Ry. We employed ab initio pseudopotentials, generated within the Troullier–Martins scheme<sup>40</sup>, including the non-linear core-correction for the iron atom<sup>41</sup> to enhance the transferability with respect to magnetic excitation. Our calculations were made using the generalized gradient-corrected approximation of the spin-dependent Density Functional Theory (DFT-LSD), following the prescription of Becke and Perdew<sup>42</sup>. Structural optimizations were performed by means of molecular dynamics with annealing of the atomic velocities, using a time step of 3.0 fs and the fictitious mass of the electrons was set at 900 a.u. The systems are enclosed in an isolated supercell of sizes depending on the ligand under examination (18 · 14 · 18Å for small models, 18 · 18 · 18Å for medium models and 26 · 22 · 22Å for large models).

The energy required for the dissociation process (bond dissociation energy, BDE) has been calculated considering the quartet spin state for the iron(III)-heme, that is generally the lowest-lying state<sup>43-45</sup>. The  $[\text{Fe}^{\text{III}}(\text{PPIX})]^+$  starting structures (Figure 2) were taken from previously optimized structures, with the substituents on the PPIX macrocycle attached in the same orientation as found in the crystal structure of CYP51<sup>20</sup>. Vinyl substituents are in *trans* position with respect to the C2-C3 porphyrin bond, pointing opposite to the nearest  $\text{CH}_3$  substituent. However, the two torsional isomeric forms of each vinyl are in thermal equilibrium at room temperature and the energy difference between the two isomers is less than 2 kcal mol<sup>-1</sup><sup>46</sup>. Propionic groups were also considered in a *trans* orientation with respect to the porphyrin plan, according to the P450 sterol 14 $\alpha$ -demethylase X-ray structure and the intramolecular hydrogen bonding network related to the two propionic acid side-chain<sup>47</sup>. Optimized  $[\text{Fe}^{\text{III}}(\text{PPIX})\text{L}]^+$  structures revealed an “out-of-plane” displacement of the metal atom inside of the iron-porphyrin core while the axial ligand was considered oriented towards the propionic groups.

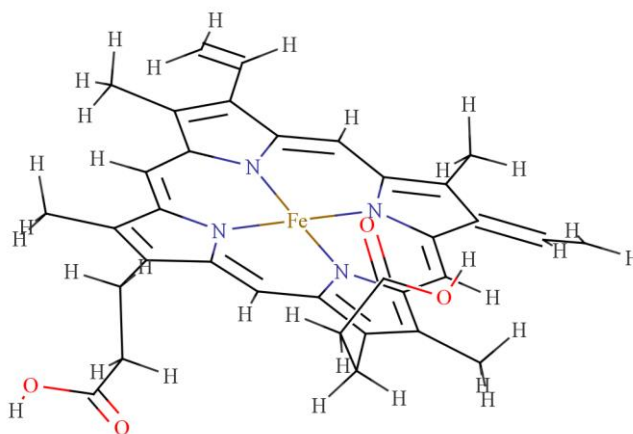


**Figure 2.** Optimized geometric structure for the computed  $[\text{Fe}^{\text{III}}\text{PPIX}]^+$  ion.

### 4.3. Results and Discussion

In the present study,  $[\text{Fe}^{\text{III}}(\text{PPIX})\text{L}]^+$  complexes, formed in solution, transferred in the gas-phase by electrospray ionization and selected by a quadrupolar filter, were assayed by CID at variable energy in a hybrid triple quadrupole linear ion trap mass spectrometer. Seven typicalazole drugs and model compounds, including 1-M, T, Py, F, M, I, B and K (Figure 1) were tested, each inhibitor endowed with a chemical motif (namely an aza group) that may interact with the  $\text{Fe}^{\text{III}}(\text{PPIX})$ . While Miconazole, Bifonazole and Ketoconazole interact with heme-iron by an imidazole ring, Fluconazole and Itraconazole have a triazole ring. Finally, the three simple molecules, 1-Methylimidazole, 1,2,4-Triazole and Pyridine, were taken into consideration as model structures for comparison purposes. When the complexes of interest were analyzed under ESI-MS, a remarkable signal intensity were observed for each adduct, indicative of a high affinity of heme ions towards the selectedazole molecules.

#### 4.3.1. Kinetic Energy of the Precursor Ions

In our tandem mass spectrometer, sampled ions suffer many collisions in q0. This process results in the thermalization of the ions. Instrumental parameters will then affect the potential the ions will experience (nominal zero). This value is needed to calculate the potential difference that accelerates the ions into q0 prior to extraction and collision within q2. Hence, the zero point of the kinetic energy scale as well as the width of the kinetic energy distribution were measured using retarding potential analysis and controlled by fine adjustments of the focusing lens system. Resolution parameters were set as 0.7 da of spectral resolution and 1 V as voltage difference between q0 and Q1 (see the Supporting Information, IE1 and high-pass-mass-filter). For instance, working in EPI mode, the ion  $[\text{Fe}^{\text{III}}(\text{PPIX})1\text{-M}]^+$  displays a gaussian distribution of kinetic energy with a full-width half maximum (*fwhm*) of 4.0 eV in the laboratory frame as shown in Figure 3.

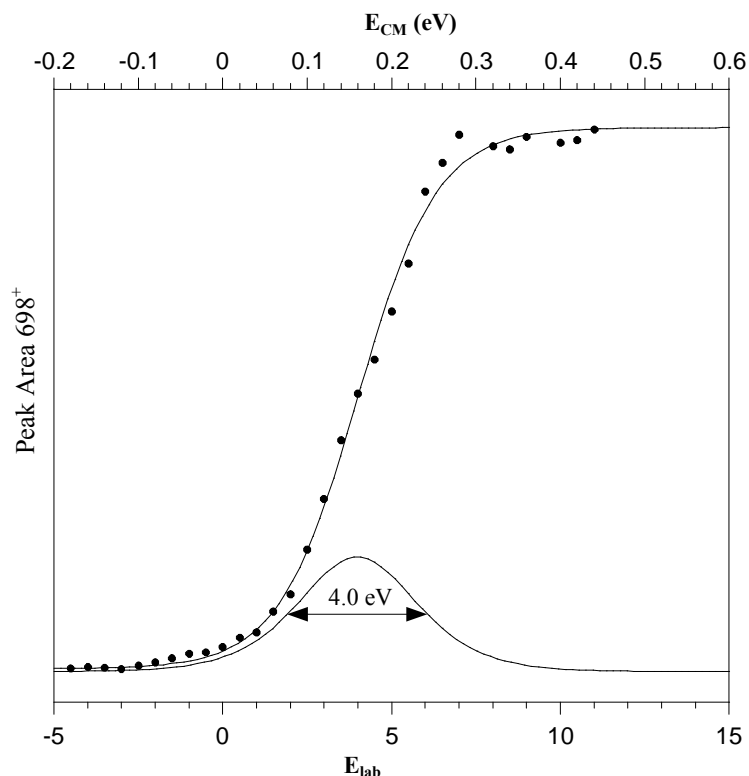


**Figure 3.** The retarding potential analysis of the parent-ion ( $m/z$  616). A Gaussian fit of the first derivative of the retarding potential data reveals a large kinetic energy distribution (4.0 eV).

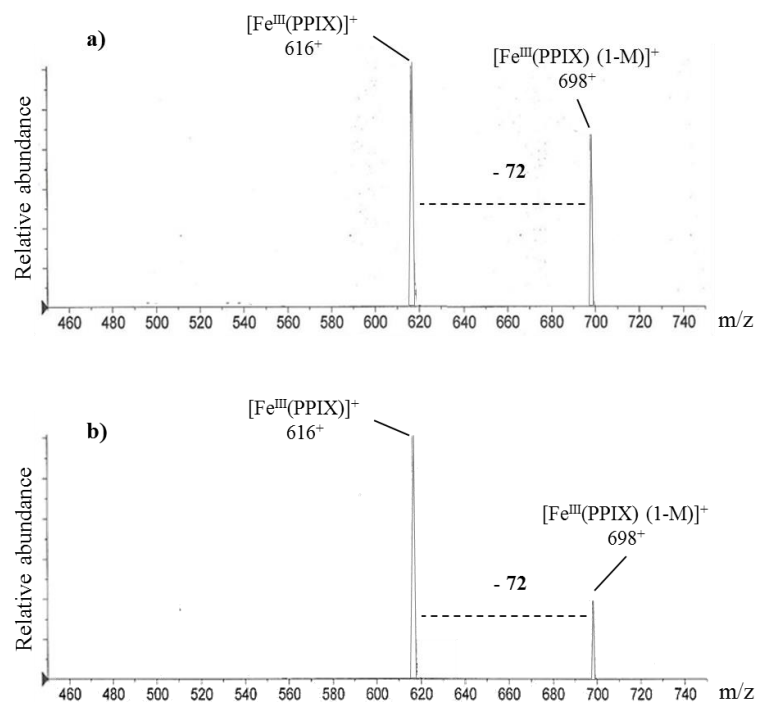
The *fwhm* of the Gaussian fit of the first derivative of the retarding potential data corresponds to the energy spread of the  $[\text{Fe}^{\text{III}}(\text{PPIX})\text{1-M}]^+$  ion energy, while the maximum of the Gaussian profile represents the zero point of the energy scale. A range of values between 2.9 and 5.8 eV are found to part the nominal instrumental zero from the true zero of the energy scale. Kinetic energy distributions between 3.4 and 6.0 eV ( $E_{\text{lab}}$ , *fwhm*) have been measured for the various complexes. The *fwhm* is wider for larger complexes such as  $[\text{Fe}^{\text{III}}(\text{PPIX})\text{I}]^+$  and  $[\text{Fe}^{\text{III}}(\text{PPIX})\text{K}]^+$ , probably due to a perturbations as a result of rf heating during passage of the ions through Q1. However, the width of the kinetic energy distribution only reflects the axial component of the kinetic energy of the precursor ion (translational energy). Operation at low ion energies. In considering the  $E_{\text{CM}}$ , nominal zero corrections of each complex must be taken into account, since the ions may differ by as much as several electron volts from the nominal laboratory energy.

### 4.3.2. Phenomenological Threshold Energy Determination

In the discussion of the appearance energies for dissociation, a reference paper to be considered is the report on ligand transfer and ligand association reactions by Angelelli et al. for a variety of  $[\text{Fe}^{\text{III}}(\text{PPIX})\text{L}]^+$  ions<sup>48</sup>. In this work, selected ligands L include natural and model substrates of the prosthetic group, such as amines, nitriles, ketones, and nitric oxide. Among the ligands considered in this survey, pyridine may be considered also as model for the nitrogen-containing inhibitor class which this doctoral thesis is focused on. Pyridine displayed a remarkably high heme cation affinity. It showed up as one of the most strongly bound ligands towards  $[\text{Fe}^{\text{III}}(\text{PPIX})]^+$ . The high affinity displayed by pyridine for the metal respect was found in line with high its gas-phase basicity<sup>49,50</sup>. This finding was later confirmed by Hayes et al. who studied the relative binding energies for  $[\text{Fe}^{\text{III}}(\text{PPIX})]^+$  with eight model nitrogen bases from variable energy CID experiments<sup>51</sup>. In the interesting work by Balding et al.<sup>23</sup> on the mechanism of inhibition of P450 enzymes by azole drugs, the mode of interaction between the three most representative nitrogen ring molecules (pyridine, 4-Methylimidazole and 1-Methyltriazole) and an unsubstituted heme moiety was elucidated. A displacement mechanism of water by azole drugs was theoretically demonstrated with the help of DFT. A complete and exhaustive description of the iron coordination structure laid the basis for further elucidation of the mechanisms of drug activity. Furthermore, the nature of the azole-heme linkage has been clearly elucidated<sup>23</sup>. Even molecular nitrogen has been conceived as potential ligand. However, interaction with iron is too weak to allow the system to be considered as a potential and informative subject for CID experiments.

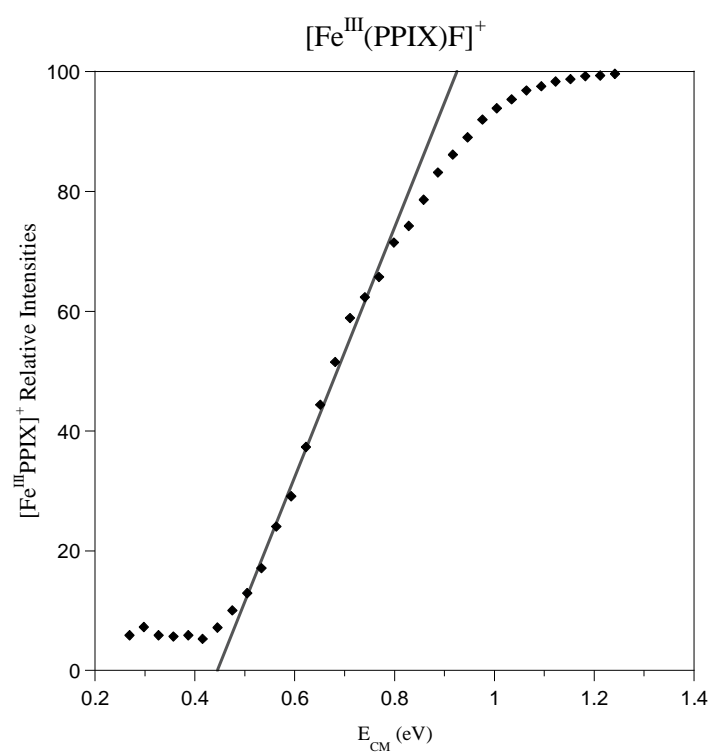
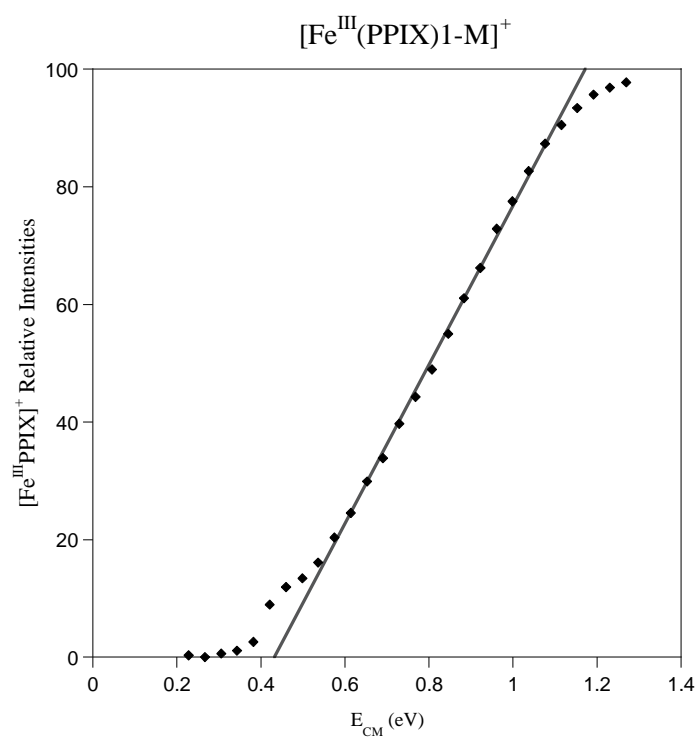
Therefore, the present work focuses on the binding with ligands of the azole family (Figure 1) and on how they chemically act as inhibitors through the interaction with their aza-type nitrogen atoms. Elucidating the binding between reference azole structures (1-Me, T, P) and the  $\text{Fe}^{\text{III}}(\text{PPIX})^+$  complex yields a scale of relative binding energies of azole drugs (M, B, I, K, F). When the variable-energy CID process was monitored for the eight selected precursor  $[\text{Fe}^{\text{III}}(\text{PPIX})\text{L}]^+$  adduct ions in a hybrid triple quadrupole linear ion trap mass spectrometer, the loss of the neutral azole ligand (L), resulting in free  $[\text{Fe}^{\text{III}}(\text{PPIX})]^+$ , is the only dissociation channel observed over the whole examined energy range. As an

example, Figure 4 shows the mass spectra obtained after selection of  $[\text{Fe}^{\text{III}}(\text{PPIX})1\text{-M}]^+$  ( $m/z$  698) and CID at a collision energy of 10 (a) and 22 (b) eV.



**Figure 4.** CID spectra of mass-selected  $[\text{Fe}^{\text{III}}(\text{PPIX})1\text{-M}]^+$  at a collision energy of a) 10 and b) 22 eV. The CID process results in the loss of  $m/z$  72 ( $L=$  1-Methylimidazole).

Figure 5 shows the dependence of the relative abundances of parent and fragment ions on the collision energy in the center-of-mass frame. Linear extrapolation of the rise of the sigmoid curve yields a phenomenological threshold energy ( $E_{\text{PT}}$ ) for the sampled complex. Exemplary CID breakdown graphs of mass selected  $[\text{Fe}^{\text{III}}(\text{PPIX})\text{L}]^+$  adduct ions are depicted for  $L=$  1-Methylimidazole, Ketoconazole and Fluconazole in Figure 5.



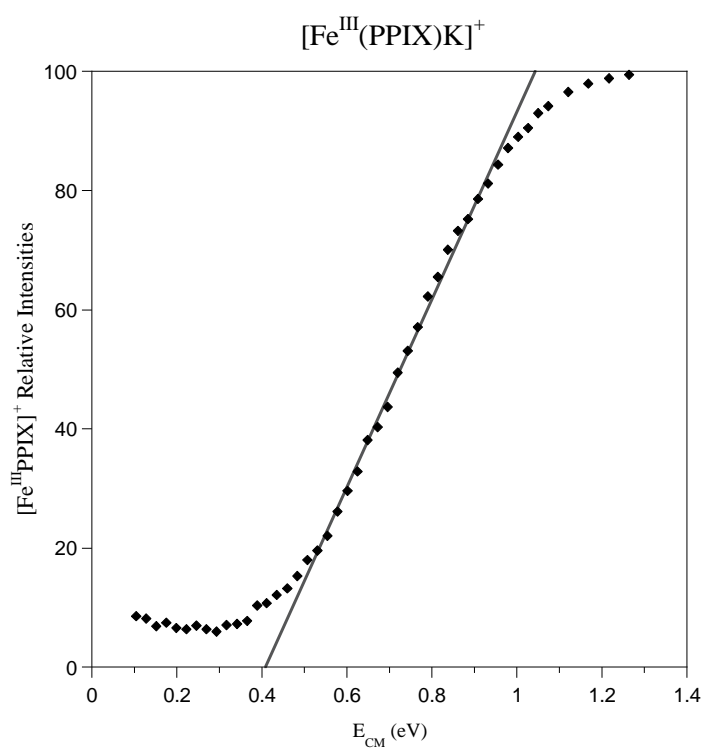


**Figure 5.** Energy variable CID curves of mass selected  $[\text{Fe}^{\text{III}}(\text{PPIX})1\text{-Me}]^+$  ( $m/z$  698),  $[\text{Fe}^{\text{III}}(\text{PPIX})\text{F}]^+$  ( $m/z$  922) and  $[\text{Fe}^{\text{III}}(\text{PPIX})\text{K}]^+$  ( $m/z$  1146) complexes as a function of  $E_{\text{CM}}$ .

Linear extrapolation of the rise of the sigmoid curve yields a phenomenological threshold energy for the appearance of  $[\text{Fe}^{\text{III}}(\text{PPIX})]^+$  ( $E_{\text{PT}}$ ). The  $E_{\text{PT}}$  values for all complexes (in eV) are listed in the following table (Table 2).



adduct	$E_{PT}^1$	$BDE_{theor}^1$
$[Fe^{III}(PPIX)T]^+$	$0.25 \pm 0.2$	$0.79 \pm 0.5$
$[Fe^{III}(PPIX)I]^+$	$0.35 \pm 0.2$	$1.00 \pm 0.2$
$[Fe^{III}(PPIX)F]^+$	$0.44 \pm 0.2$	$1.18 \pm 0.2$
$[Fe^{III}(PPIX)1-M]^+$	$0.42 \pm 0.2$	$1.03 \pm 0.5$
$[Fe^{III}(PPIX)K]^+$	$0.42 \pm 0.2$	$1.22 \pm 0.2$
$[Fe^{III}(PPIX)Py]^+$	$0.44 \pm 0.2$	$0.88 \pm 0.5$
$[Fe^{III}(PPIX)M]^+$	$0.48 \pm 0.2$	$1.16 \pm 0.2$
$[Fe^{III}(PPIX)B]^+$	$0.48 \pm 0.2$	$1.17 \pm 0.2$

<sup>1</sup> Values are given in eV.

**Table 2.** Values of phenomenological appearance energies ( $E_{PT}$ ), obtained by linear extrapolation of the rise of sigmoid curves, and  $BDE_{theor}$ , obtained performing the Car-Parrinello molecular dynamics calculations.

These values allow us to obtain a ladder of energies required to activate the loss of azole L from the  $[Fe^{III}(PPIX)L]^+$  adduct ion, and to point out how the differently activated nitrogens of each ligand react to an external collisional jolt. The breaking of the  $Fe^{III}$ -L bond of triazole-based drugs requires a lower energy compared to the imidazole-based drugs. Interestingly, the dissociation experiments show a higher dissociation energy for the ligand 1-M ( $0.42 \text{ eV} \pm 0.2$ ) and Py ( $0.44 \text{ eV} \pm 0.2$ ) if compared to T ( $0.25 \text{ eV} \pm 0.2$ ). So, it may be not surprising that each imidazole-based drug (B, M, K) shows a higher  $E_{PT}$  value if compared to triazole-based drugs highlighted in dark gray on Table 2.

One should keep in mind that in the isolated complex we are not taking into account the large number and wide variety of non-covalent interactions playing a role when the heme-ligand complex is embedded within the enzyme cavity. Owing to the large number of factors that come into play in the physiological process, a direct comparison of the gas-phase and the biological values listed in Table 1 is not amenable. However, probing the variability of the naked interactions with the metal provides helpful information on the capability of the coordinating scaffold. Upon scrutiny of Table 2, it emerges that B and M present the highest  $E_{PT}$  values of  $0.48 \text{ eV} \pm 0.2$  ( $46.31 \text{ kJ mol}^{-1}$ ). This finding may be related to the higher gas-phase basicity of the imidazole ring with respect to the triazole moiety, although additional electronic effects of the functional

groups directly connected to the azole core cannot be excluded. This point will be further discussed in the theoretical section.

### 4.3.3. Bond Dissociation Energy Calculations

Bond dissociation energies of all eight complexes sampled in the present study were computed with the help of DFT and Car-Parrinello molecular dynamics (CPMD). DFT represents an appropriate method to reproduce relative  $E_{PT}$ . A recent study on the binding properties of azole drugs is reported by Balding et al. in an already cited reference. Their ability to highlight the presence of a hydrogen bond network offers an accurate treatment of the model  $[\text{Fe}^{\text{III}}(\text{PPIX})\text{L}]^+$ , where the effects of proximal hydrogen-bonding donors and electron withdrawing groups have been properly taken into account. In our work, the full presence of substituents on the porphine ring, namely propionic, vinyl and methyl substituents of  $\text{Fe}^{\text{III}}(\text{PPIX})$ , has been considered, so reproducing the complete prosthetic group.

Computations have been performed in a stepwise sequence. First, we performed a complete structure relaxation of the  $[\text{Fe}^{\text{III}}(\text{PPIX})1\text{-M}]^+$  complex in two different spin state: doublet and quartet. Balding et al. theoretically demonstrated that the quartet spin state is the lowest one for the pentacoordinate geometry of iron(III). We ignored any spin crossing in the association process of the ligand. We computed an energy difference of about  $47 \text{ kJ mol}^{-1}$  between the doublet and the quartet spin state in  $[\text{Fe}^{\text{III}}(\text{PPIX})\text{T}]^+$  complex, where the high spin state is largely preferred (as experimentally demonstrated for the ground state of the 5-coordinate heme in catalases). The starting structure of  $[\text{Fe}^{\text{III}}(\text{PPIX})]^+$  was taken from a previously optimized structure<sup>52</sup>, with the propionic substituents attached in *trans*-position with respect to the porphyrin plane and the vinyl groups in an opposite orientation towards each other (as shown in Figure 6).

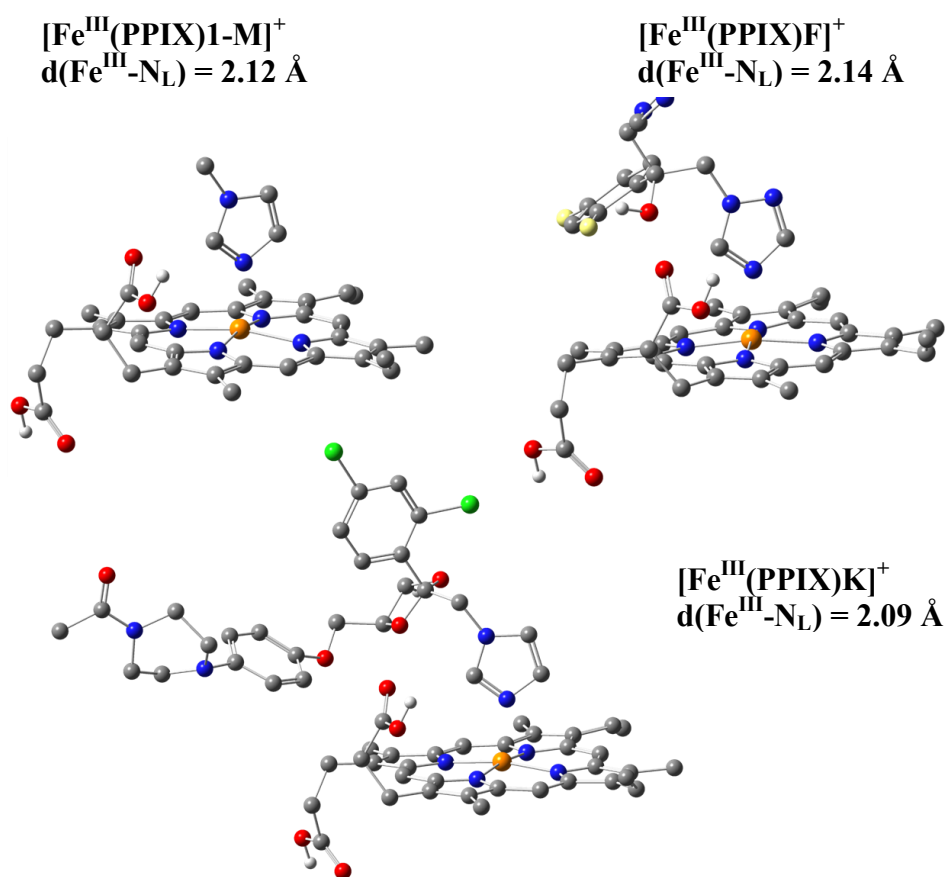


**Figure 6.** Optimized geometries for  $[\text{Fe}^{\text{III}}(\text{PPIX})1\text{-M}]^+$ ,  $[\text{Fe}^{\text{III}}(\text{PPIX})\text{F}]^+$  and  $[\text{Fe}^{\text{III}}(\text{PPIX})\text{K}]^+$  complexes. Hydrogen atoms, directly bonded to carbon, are omitted for the sake of clarity.

Overall, the values of the bond distances follow the same trend as the  $E_{PT}$  values (Table 3). The length of the  $Fe^{III}-N_L$  bond in  $[Fe^{III}(PPIX)B]^+$  and  $[Fe^{III}(PPIX)M]^+$  complexes is 2.11 Å, in correspondence with the highest  $E_{PT}$  value (0.48 eV). It is equally interesting how well the method relates the longest bond distance to the Itraconazole ligand (2.21 Å) to the lowest  $E_{PT}$ . The  $Fe^{III}-N_L$  bond length appears not to be affected either by steric hindrance or by the hydrophobicity of the ligand. However steric hindrance may play an important role in the coordination mechanism of the drugs upon study, and, in addition, the charge distribution on the chelating nitrogen may control the noncovalent interaction with the prosthetic groups. In Figure 6 the geometries of L = 1-M; F; K show a comparable orientation of the N-substituent towards the propionic groups and an “out of plane” effect of the iron. A complete scan of the torsional angle between the ligand and the prosthetic group was performed suggesting the correct orientation of the ligand with respect to all degrees of freedom of the system. The minimum-energy structure parameters of the  $[Fe^{III}(PPIX)L]^+$  complexes are reported in Table 3, defining the distance and the orientation of the ligand in the axial position.

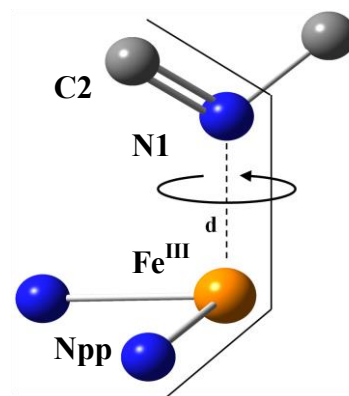


**Figure 7.** Torsional motion of the azole drug.

	$\text{Fe}^{\text{III}}\text{-N}_L$ distance	Npp-Fe-N1-C2 dihedral angle
$[\text{Fe}^{\text{III}}(\text{PPIX})\text{K}]^+$	2.09	-61.94
$[\text{Fe}^{\text{III}}(\text{PPIX})\text{B}]^+$	2.11	-37.20
$[\text{Fe}^{\text{III}}(\text{PPIX})\text{M}]^+$	2.11	-39.25
$[\text{Fe}^{\text{III}}(\text{PPIX})(1\text{-M})]^+$	2.12	-44.57
$[\text{Fe}^{\text{III}}(\text{PPIX})\text{T}]^+$	2.12	-42.72
$[\text{Fe}^{\text{III}}(\text{PPIX})\text{F}]^+$	2.14	-64.14
$[\text{Fe}^{\text{III}}(\text{PPIX})\text{Py}]^+$	2.16	-43.17
$[\text{Fe}^{\text{III}}(\text{PPIX})\text{I}]^+$	2.15	-72.06

**Table 3.** Structural parameters computed for the eight complexes by CPMD calculations. Distances are given in angstrom and angles in degrees.

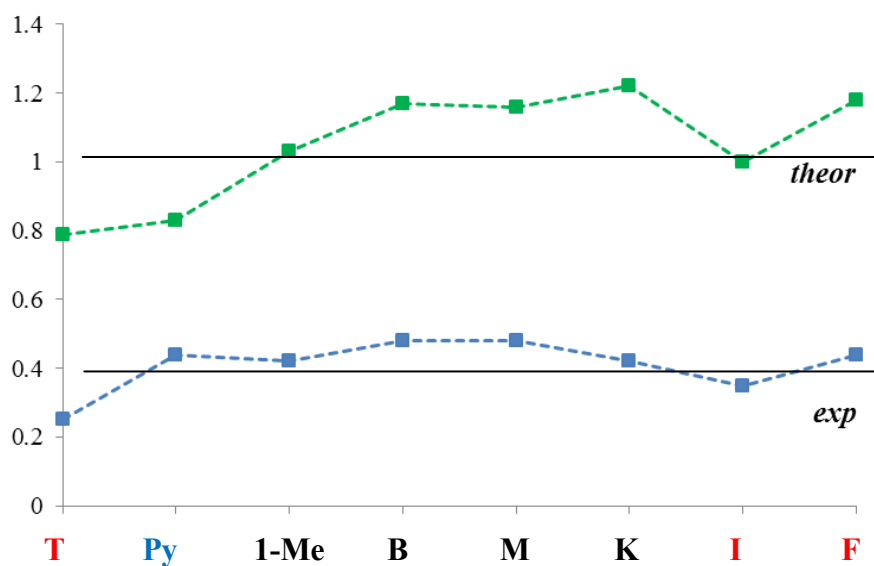


**Figure 8.** Comparison of the trend between the experimental results of  $E_{PT}$  and  $BDE_{theor}$  (green line).

From the comparison of Figure 8, a rather similar trend among the computed and the experimental values (blue line) emerges, although all  $BDE_{\text{theor}}$  (green line) are consistently larger. When comparing either triazole- (I and T) or imidazole- (K, B, M) based drugs, the latter ones display a higher dissociation energy threshold as well as a higher predicted BDE, while the differences between the various complexes are somewhat flat. The simple structure and hydrophobic character of B might explain its high coordination ability, where extensive conjugation over three phenyl rings may play a role in a non-covalent interaction with the porphyrin ring. On the other side, a dioxolane functional group ( $-\text{CH}(\text{OR})_2$ ), shared by K and I, should help the azole ring in the coordination to  $\text{Fe}^{\text{III}}$  compared to the unsubstituted hydroxyl group in F ( $-\text{C}(\text{OH})(\text{R})_2$ ) compound, where the two triazole rings bound to the same carbon atom do not seem to positively affect the respective coordination ability.

#### 4.4. Conclusions

A combined approach based on gas-phase collision-induced dissociation experiments along with a theoretical determination of bond dissociation energies has been applied to unveil binding features of eight heme-azole complexes. Naked adduct ions were studied, allowing intrinsic binding properties to be determined, without any solvent, counter ion or matrix effect. Pyridine, imidazole-like and triazole-like drugs were compared in their ability to chelate iron in the Fe(III)-protoporphyrin IX prosthetic group. Actually, a better interpretation of this kind of noncovalent interaction represents a challenge in the design of new antifungal analogues. Thus the work described here get help fundamental understanding in the antifungal research and the data in this article appear consistent with available data for antifungal activity against human  $14\alpha$ -demethylase. A different protein environment of *candida albicans*  $14\alpha$ -demethylase may have an impact on the inhibition of fungal enzymes. In this perspective, a better understanding of the driving forces between azole compounds and the binding pocket of CaCYP51 might facilitate and indeed speed up the research. This new approach yields a determination of phenomenological relative threshold energies of all complexes, whose theoretical investigation confirmed the general trend. Imidazole like drugs are excellent chelating agents in the interaction with heme iron. Nearly behavior can be obtained from pyridine

scaffold. The good sensitivity and selectivity of use of the collision-induced dissociation experiments linked to a theoretical prediction make them more compatible for extrapolating bond dissociation energies strengths than other techniques which we are aware.

#### **4.5. Training Experience in CPMD Calculations at Parc Cientific de Barcelona**

I would like to express my sincere gratitude to Research Professor Carme Rovira for the opportunity to obtain up to three months of research experience on my on-going project. The theoretical support to the study on the binding of antifungal azole ligands to heme has been carried during these research experience at the “Parc Cientific de Barcelona”, where I completed the investigation on the binding of azole drugs. The activity of the research group of Prof. Rovira is focused on the simulation of biological processes , in particular on the mechanism of action of ligand-protein interactions. Professor Rovira is widely experienced in the study of the heme systems. Thus I become familiar with a method of molecular dynamics (Car-Parrinello Molecular Dynamics (CPMD)) , an implementation of Density Functional Theory ideally suited to the study of macro-complexes of biological interest. The theoretical binding energies correctly interpret the data obtained from experiments in collision-induced dissociation, opening up prospects for a method of investigation aimed at identifying molecules with specific antifungal activity.

## 4.6. References

- (1) Giusiano, G. E.; Mangiaterra, M.; Rojas, F.; Gomez, V. Yeasts Species Distribution in Neonatal Intensive Care Units in northeast Argentina *Mycoses* **2004**, 47, 300-303.
- (2) Carrillo-Munoz, A. J.; Giusiano, G.; Ezkurra, P. A.; Quindos, G. Antifungal Agents: Mode of Action in Yeast Cells *Soc. Espan. de Quimiot.* **2006**, 19, 130-139.
- (3) Georgopapadaku, N. H.; Walsh, T. J. Human Mycoses: Drugs and Targets for Emerging pathogens *Science* **1994**, 264, 371-373.
- (4) Walsh, T. J.; Groll, A.; Hiemenz, J.; Fleming, R.; Roilides, E.; Anaissie, E. Infections due to Emerging and Uncommon Medically Important Fungal Pathogens *Clin. Mic. Inf.* **2004**, 10, 48-66.
- (5) Andriole, V. T. Current and Future Antifungal Therapy: New Targets for Antifungal Therapy *Int. J. of Antimicrob. Ag.* **2000**, 16, 317-321.
- (6) Poulos, T. L.; Raag, R. Cytochrome P450cam: Crystallography, Oxygen Activation, and Electron Transfer *FASEB* **1992**, 6, 674-679.
- (7) Bossche, H. In *Current Topics in Medical Mycology*; McGinnis, M., Ed.; Springer New York: 1985; Vol. 1, p 313-351.
- (8) Vandenbossche, H.; Marichal, P.; Gorrens, J.; Bellens, D.; Verhoeven, H.; Coene, M. C.; Lauwers, W.; Janssen, P. A. J. Interaction of Azole Derivatives with Cytochrome-P-450 Isozymes in Yeast, Fungi, Plants and Mammalian-Cells *Pestic. Sci.* **1987**, 21, 289-306.
- (9) Trosken, E. R.; Adamska, M.; Arand, M.; Zarn, J. A.; Patten, C.; Volkel, W.; Lutz, W. K. Comparison of Lanosterol-14 Alpha-Demethylase (CYP51) of Human and *Candida Albicans* for Inhibition by Different Antifungal Azoles *Toxicology* **2006**, 228, 24-32.
- (10) Schenkman, J. B.; Remmer, H.; Estabrook, R. W. Spectral Studies of Drug Interaction with Hepatic Microsomal Cytochrome *Mol. Pharmacol.* **1967**, 3, 113-123.
- (11) Schuster, I. The Interaction of Representative Members from Two Classes of Antimycotics (the Azoles and the Allylamines) with Cytochromes P450 in Steroidogenic Tissues and Liver *Xenobiotica* **1985**, 15, 529-546.
- (12) Varhe, A.; Olkkola, K. T.; Neuvonen, P. J. Oral Triazolam is Potentially Hazardous to Patients Receiving Systemic Antimycotics Ketoconazole or Itraconazole *Clin. Pharmacol. Ther.* **1994**, 56, 601-607.
- (13) Park, J. Y.; Shon, J. H.; Kim, K. A.; Jung, H. J.; Shim, J. C.; Yoon, Y. R.; Cha, I. J.; Shin, J. G. Combined Effects of Itraconazole and CYP2D6\*10 Genetic Polymorphism on the Pharmacokinetics and Pharmacodynamics of Haloperidol in Healthy Subjects *J. Clin. Psychoph.* **2006**, 26, 135-142.
- (14) Murayama, N.; Imai, N.; Nakane, T.; Shimizu, M.; Yamazaki, H. Roles of CYP3A4 and CYP2C19 in Methyl hydroxylated and N-oxidized Metabolite Formation from Voriconazole, a New Antifungal Agent, in Human Liver Microsomes *Bioch. Pharm.* **2007**, 73, 2020-2026.
- (15) Guardiola-Diaz, H. M.; Foster, L. A.; Mushrush, D.; Vaz, A. D. Azole-antifungal Binding to a Novel Cytochrome P450 from *Mycobacterium Tuberculosis*: Implications for Treatment of Tuberculosis *Bioch. Pharm.* **2001**, 61, 1463-1470.
- (16) McLean, K. J.; Cheesman, M. R.; Rivers, S. L.; Richmond, A.; Leys, D.; Chapman, S. K.; Reid, G. A.; Price, N. C.; Kelly, S. M.; Clarkson, J.; Smith, W. E.; Munro, A. W. Expression, Purification and Spectroscopic Characterization of The Cytochrome P450 CYP121 from *Mycobacterium Tuberculosis* *J. Inorg. Bioch.* **2002**, 91, 527-541.
- (17) Banfi, E.; Scialino, G.; Zampieri, D.; Mamolo, M. G.; Vio, L.; Ferrone, M.; Fermeglia, M.; Paneni, M. S.; Pricl, S. Antifungal and Antimycobacterial Activity of New Imidazole and Triazole Derivatives. A Combined Experimental and Computational Approach *J. Antimicrob. Chem.* **2006**, 58, 76-84.
- (18) Poulos, T. L.; Howard, A. J. Crystal Structures of Metyrapone- and Phenylimidazole-inhibited Complexes of Cytochrome P-450cam *Biochemistry* **1987**, 26, 8165-8174.
- (19) Podust, L. M.; Poulos, T. L.; Waterman, M. R. Crystal Structure of Cytochrome P450 14Alpha -Demethylase (CYP51) from *Mycobacterium Tuberculosis* in Complex with Azole Inhibitors *PNAS* **2001**, 98, 3068-3073.
- (20) Strushkevich, N.; Usanov, S. A.; Park, H. W. Structural Basis of Human CYP51 Inhibition by Antifungal Azoles *J. Mol. Biol.* **2010**, 397, 1067-1078.
- (21) Lepesheva, G. I.; Park, H. W.; Hargrove, T. Y.; Vanhollebeke, B.; Wawrzak, Z.; Harp, J. M.; Sundaramoorthy, M.; Nes, W. D.; Pays, E.; Chaudhuri, M.; Villalta, F.; Waterman, M. R. Crystal Structures of *Trypanosoma Brucei* Sterol 14Alpha-Demethylase and Implications for Selective Treatment of Human Infections *J. Biol. Chem.* **2010**, 285, 1773-1780.



- (22) Rupp, B.; Raub, S.; Marian, C.; Holtje, H. D. Molecular Design of Two Sterol 14 $\alpha$ -Demethylase Homology Models and their Interactions with the Azole antifungals Ketoconazole and Bifonazole *J. Comp. Mol. Design* **2005**, *19*, 149-163.
- (23) Balding, P. R.; Porro, C. S.; McLean, K. J.; Sutcliffe, M. J.; Marechal, J. D.; Munro, A. W.; de Visser, S. P. How do Azoles Inhibit Cytochrome P450 Enzymes? A Density Functional Study *J Phys. Chem. A* **2008**, *112*, 12911-12918.
- (24) Mishra, E.; Worlinsky, J. L.; Gilbert, T. M.; Bruckner, C.; Ryzhov, V. Axial Imidazole Binding Strengths in Porphyrinoid Cobalt(III) Complexes as Studied by Tandem Mass Spectrometry *J. Am. Soc. Mass. Spectrom.* **2012**, *23*, 1135-1146.
- (25) Covey, T. R.; Bonner, R. F.; Shushan, B. I.; Henion, J. The Determination of Protein, Oligonucleotide and Peptide Molecular Weights by Ion-spray Mass Spectrometry *Rap. Comm. Mass Spectr.* **1988**, *2*, 249-256.
- (26) Smith, R. D.; Loo, J. A.; Barinaga, C. J.; Edmonds, C. G.; Udseth, H. R. Capillary Zone Electrophoresis and Isotachopheresis-mass Spectrometry of Polypeptides and Proteins Based Upon an Electrospray Ionization Interface *J. Chromatogr.* **1989**, *480*, 211-232.
- (27) Edmondson, R. D.; Russell, D. H. Evaluation of Matrix-assisted Laser Desorption Ionization-time-of-flight Mass Measurement Accuracy by Using Delayed Extraction *J. Am. Soc. Mass. Spectrom.* **1996**, *7*, 995-1001.
- (28) Guo, X.; Duursma, M. C.; Kistemaker, P. G.; Nibbering, N. M.; Vekey, K.; Drahos, L.; Heeren, R. M. Manipulating Internal Energy of Protonated Biomolecules in Electrospray Ionization Fourier Transform Ion Cyclotron Resonance Mass Spectrometry *J. Mass. Spectrom.* **2003**, *38*, 597-606.
- (29) Light-Wahl, K. J.; Loo, J. A.; Edmonds, C. G.; Smith, R. D.; Witkowska, H. E.; Shackleton, C. H.; Wu, C. S. Collisionally Activated Dissociation and Tandem Mass Spectrometry of Intact Hemoglobin  $\beta$ -chain Variant Proteins with Electrospray Ionization *Biol. Mass. Spectrom.* **1993**, *22*, 112-120.
- (30) Senko, M. W.; Speir, J. P.; McLafferty, F. W. Collisional Activation of Large Multiply Charged Ions Using Fourier Transform Mass Spectrometry *Anal. Chem.* **1994**, *66*, 2801-2808.
- (31) Harwood, L. M.; Moody, C. J.; Percy, J. M. *Experimental Organic Chemistry: Standard and Microscale*; Wiley, 1999.
- (32) Schroder, D.; Semialjac, M.; Schwarz, H. Secondary Kinetic Isotope Effects in Cation-bound Dimers of Acetone (C<sub>3</sub>H<sub>6</sub>O)M(C<sub>3</sub>D<sub>6</sub>O)<sup>(+)</sup> with M = H, Li, Na, K, Rb, Ag, and Cs *Int. J. Mass. Spectrom.* **2004**, *233*, 103-109.
- (33) Schroder, D.; Schwarz, H.; Aliaga-Alcalde, N.; Neese, F. Fragmentation of the (cyclam-acetato)Iron Azide Cation in the Gas-Phase *Eur. J. Inorg. Chem.* **2007**, 816-821.
- (34) Chiavarino, B.; Crestoni, M. E.; Fornarini, S.; Scuderi, D.; Salpin, J. Y. Interaction of Cisplatin with Adenine and Guanine: A Combined IRMPD, MS/MS, and Theoretical Study *J. Am. Chem. Soc.* **2013**, *135*, 10877-10877.
- (35) Fedorov, A.; Couzijn, E. P. A.; Nagornova, N. S.; Boyarkin, O. V.; Rizzo, T. R.; Chen, P. Structure and Bonding of Isoleptic Coinage Metal (Cu, Ag, Au) Dimethylaminonitrenes in the Gas-phase *J. Am. Chem. Soc.* **2010**, *132*, 13789-13798.
- (36) Couzijn, E. P. A.; Zocher, E.; Bach, A.; Chen, P. Gas-Phase Energetics of Reductive Elimination from a Palladium(II) N-Heterocyclic Carbene Complex *Chem-Eur. J.* **2010**, *16*, 5408-5415.
- (37) McClellan, J. E.; Murphy, J. P.; Mulholland, J. J.; Yost, R. A. Effects of Fragile Ions on Mass Resolution and on Isolation for Tandem Mass Spectrometry in the Quadrupole Ion Trap Mass Spectrometer *Anal. Chem.* **2002**, *74*, 402-412.
- (38) Car, R.; Parrinello, M. Unified Approach for Molecular Dynamics and Density-Functional Theory *Phys. Rev. Lett.* **1985**, *55*, 2471-2474.
- (39) Carloni, P.; Rothlisberger, U.; Parrinello, M. The Role and Perspective of Ab Initio Molecular Dynamics in the Study of biological systems *Acc. Chem. Res.* **2002**, *35*, 455-464.
- (40) Troullier, N.; Martins, J. L. Efficient pseudopotentials for plane-wave calculations. II. Operators for fast iterative diagonalization *Phys. Rev. B* **1991**, *43*, 8861-8869.
- (41) Louie, S. G.; Froyen, S.; Cohen, M. L. Nonlinear Ionic Pseudopotentials in Spin-Density-Functional Calculations *Phys. Rev. B* **1982**, *26*, 1738-1742.
- (42) Becke, A. D. Density Functional Calculations of Molecular-Bond Energies *J. Chem. Phys.* **1986**, *84*, 4524-4529.
- (43) Groenhof, A. R.; Swart, M.; Ehlers, A. W.; Lammertsma, K. Electronic Ground States of Iron Porphyrin and of the First Species in the Catalytic Reaction Cycle of Cytochrome P450s *J. Phys. Chem. A* **2005**, *109*, 3411-3417.

- (44) Chiavarino, B.; Crestoni, M. E.; Fornarini, S.; Rovira, C. Unravelling the Intrinsic Features of NO Binding to Iron(II)- and Iron(III)-Hemes *Inorg. Chem.* **2008**, *47*, 7792-7801.
- (45) Charkin, O. P.; Klimenko, N. M.; Charkin, D. O.; Chang, H. C.; Lin, S. H. Theoretical DFT Study of Fragmentation and Association of Heme and Hemin *J. Phys. Chem. A* **2007**, *111*, 9207-9217.
- (46) Hunter, C. L.; Lloyd, E.; Eltis, L. D.; Rafferty, S. P.; Lee, H.; Smith, M.; Mauk, A. G. Role of the Heme Propionates in the Interaction of Heme with Apomyoglobin and Apocytochrome b5 *Biochemistry* **1997**, *36*, 1010-1017.
- (47) Siu, C. K.; Guo, Y.; Hopkinson, A. C.; Siu, K. W. How large is the [Fe(III)(protoporphyrin IX)]<sup>+</sup> ion (hemin<sup>+</sup>) in the Gas-Phase? *J Phys Chem B* **2006**, *110*, 24207-24211.
- (48) Angelelli, F.; Chiavarino, B.; Crestoni, M. E.; Fornarini, S. Binding of Gaseous Fe(III)-Heme Cation to Model Biological Molecules: Direct Association and Ligand Transfer Reactions *J. Am. Soc. Mass. Spectrom.* **2005**, *16*, 589-598.
- (49) *NIST Chemistry WebBook, NIST Standard Reference Database Number 69*; National Institute of Standards and Technology, 2005.
- (50) Crestoni, M. E.; Fornarini, S. Fourier Transform Ion Cyclotron Resonance Study of the Gas-Phase Basicity of N-nitrosodimethylamine *J. Mass. Spectrom.* **2004**, *39*, 1379-1381.
- (51) Hayes, L. A.; Chappell, A. M.; Jellen, E. E.; Ryzhov, V. Binding of Metalloporphyrins to Model Nitrogen Bases: Collision-Induced Dissociation and Ion-Molecule Reaction Studies *Int. J. Mass. Spectrom.* **2003**, *227*, 111-120.
- (52) Chiavarino, B.; Crestoni, M. E.; Fornarini, S.; Rovira, C. Protonated Heme *Chemistry* **2007**, *13*, 776-785.

---

## ACKNOWLEDGEMENTS

*I would like to thank to my PhD advisors,  
Professors Maria Elisa Crestoni  
and Rino Ragno, for supporting me during  
these past three years. I am also very  
grateful to  
Professor Simonetta Fornarini for her  
scientific advice, knowledge and many  
insightful discussions and  
suggestions. She is my best role model for a  
scientist, mentor  
and teacher. I also have to thank the other  
member of my research group,  
Barbara Chiavarino,  
she has been helpful in providing advice  
many times during my PhD school career.*

*Alberto De Petris, Rome, January 2014*

---